Applied Physics Reviews

REVIEW ARTICLE | SEPTEMBER 11 2024

The role of gallium nitride in the evolution of electric vehicles: Energy applications, technology, and challenges

Special Collection: Frontiers in energy materials research: novel measurement, modelling and processing approaches

Kazi Faridur Rahman ; Shaili Falina ; Mohamed Fauzi Packeer Mohamed ; Hiroshi Kawarada ; Mohd Syamsul

Check for updates

Appl. Phys. Rev. 11, 031322 (2024)
https://doi.org/10.1063/5.0215799

View Online
Export Citation

Articles You May Be Interested In

Programmable buck-boost converter for EV charging application

AIP Conf. Proc. (August 2024)

21 October 2024 08:24:33

AIP Publishing

Special Topics Open for Submissions

Learn More

AIP Publishing

Applied Physics Reviews REVIEW pubs.aip.org/aip/are

The role of gallium nitride in the evolution of electric vehicles: Energy applications, technology, and challenges

Cite as: Appl. Phys. Rev. **11**, 031322 (2024); doi: 10.1063/5.0215799
Submitted: 26 April 2024 · Accepted: 16 August 2024 ·
Published Online: 11 September 2024

View Online Export Citation CrossMark

Kazi Faridur Rahman,[1] Shaili Falina,[2,3,a)] Mohamed Fauzi Packeer Mohamed,[3] Hiroshi Kawarada,[4,5] and Mohd Syamsul[1,4,a)]

AFFILIATIONS

[1]Institute of Nano Optoelectronics Research and Technology (INOR), Universiti Sains Malaysia, Sains@USM, Bayan Lepas 11900, Pulau Pinang, Malaysia
[2]Collaborative Microelectronic Design Excellence Center (CEDEC), Universiti Sains Malaysia, Sains@USM, Bayan Lepas 11900, Pulau Pinang, Malaysia
[3]School of Electrical and Electronic Engineering, Universiti Sains Malaysia, Nibong Tebal 14300, Pulau Pinang, Malaysia
[4]Faculty of Science and Engineering, Waseda University, Tokyo 169-8555, Japan
[5]Power Diamond Systems Inc., Shinjuku, Tokyo 169-0051, Japan

Note: This paper is part of the APR Special Topic on Frontiers in energy materials research: novel measurement, modelling and processing approaches.
[a)]**Authors to whom correspondence should be addressed:** shailifalina@usm.my and nasyriq@usm.my

21 October 2024 08:24:33

ABSTRACT

It is only recently that the electric vehicle (EV) has evolved into a contemporary invention. There has been a rapid acceleration in the development of EVs in a number of nations in order to lessen their reliance on oil and their contribution to environmental pollution. In the tangible world, fully EVs do not release any carbon dioxide (CO_2) emissions from their tailpipes, unlike any other conventional vehicles. This results in a 50%–70% CO_2 reduction in air pollution per year. The achievement of electrification in transportation has led to a reduction in the weight and size of the vehicles as the need for internal combustion engines can be eliminated. Wide bandgap materials such as silicon carbide (SiC) and gallium nitride (GaN) offer advantages in the manufacturing of EVs. Beginning the late 2000s, the EV industry has begun to adopt GaN devices in their manufacturing processes. The semiconductor material GaN stands out as a material for power electronic systems in EVs owing to its high switching frequency, higher temperature limit, and high voltage breakdown. This review aims to provide a comprehensive overview of semiconductor GaN materials for EV applications, which could be useful to provide insights for researchers and scientists to accelerate their innovation for the improvement of EVs. This review begins with an introduction to EVs, followed by the anticipated demand for EVs. The application of GaN devices in EVs, compared to the traditional Si and SiC devices, which are the primary power devices in current EVs, is discussed. The recent advancement in GaN devices that are capable of being used in various components of a fully automated EV, such as the battery, energy storage system, auxiliary power unit, and motor drive, in addition to their use in different non-automotive vehicles such as electric aircraft, electric ships, electric railways, electric submarines, and heavy duty vehicles, is also discussed. Finally, the challenges posed by GaN devices and potential solutions to overcome these shortcomings have been addressed.

© 2024 Author(s). All article content, except where otherwise noted, is licensed under a Creative Commons Attribution (CC BY) license (https://creativecommons.org/licenses/by/4.0/). https://doi.org/10.1063/5.0215799

TABLE OF CONTENTS

I. INTRODUCTION 2
II. IS GAN THE FUTURE? 4
III. GAN-BASED POWER DEVICES IN EV SYSTEM 8
A. Energy storage system (ESS) 8
B. On-board charger module 9
C. Motor drives 15
D. Auxiliary power system (APS) 18
IV. GAN-BASED DEVICES FOR NON-AUTOMOTIVE VEHICLES 21

© Author(s) 2024

A. Electric aircraft 21
B. Heavy duty and off-road vehicles 24
C. Electric rail vehicle 27
D. Electric ships 30
E. Electric submarines 33
V. CHALLENGES FOR GAN IN EV 36
A. Cross-talk 36
B. Gate leakage current 36
C. Dynamic performance 37
D. Thermal management 38
VI. CONCLUSION AND FUTURE PROSPECTS 38

I. INTRODUCTION

Prior to the end of the 20th century, the automobile industry was exclusively dependent on oil as its main energy source. Nevertheless, the reliance on oil has resulted in several problems, including anthropogenic air pollution (particularly in densely populated regions), depletion of oil reserves, and the dependency of oil-consuming nations on oil-producing nations.[1–4] The combustion of these oils with air produces carbon dioxide (CO_2), a greenhouse gas (GHG), which contributes to global warming and climate change. The gradual increase in temperatures is altering weather patterns and causing significant disruptions to the delicate ecological equilibrium, which is a matter of great worry.[5–8] Transportation electrification offers a substantial reduction in the adverse impacts of GHG emissions on global warming, as well as a considerable decrease in reliance on oil and gas. The worldwide adoption rates of electric vehicles (EVs) have been increasing due to their many advantages, including their pollution-free nature, lower reliance on fossil fuels, cost-effectiveness, and quieter operation on the road.[9] EVs also do not release any carbon dioxide (CO_2) emissions while they are driven since they do not have a tailpipe. This results in a 50%–70% CO_2 reduction in air pollution per year.[10] The current study on EVs encompasses several areas, such as the exploration of strategies and efficacy for expanding transportation infrastructure, cost reduction, and the advancement of efficient charging systems. With the decreasing costs of technology used for EVs, it is expected that there will be a rise in public desire for these sorts of vehicles.[11] Generally, EVs can be dissected into three main categories: hybrid electric vehicles (HEVs), plug-in hybrid electric vehicles (PHEVs), and battery electric vehicles (BEVs). The categories are determined by the vehicle's power supplements and propulsion systems.[12] Table I displays a comprehensive review of several kinds of EVs. A HEV is defined as any vehicle that utilizes at least two energy sources for propulsion. The two potential sources of power are petrol or diesel fuel, in addition to a battery. In hybrid automobiles, either of the source systems has the capability to independently provide electricity to the vehicle.[13,14] Hybrids may also favor the internal combustion engine (ICE) unit, which is more efficient for highway driving. A PHEV integrates an ICE with an electric motor and battery unit, similar to a hybrid vehicle. However, PHEVs often include bigger battery units and more robust electric motors compared to conventional hybrids. This implies that PHEVs have the capability to operate only on electric power, therefore completely deactivating the ICE. A BEV is sometimes referred to as an "all-electric" or "full-electric" automobile. These vehicles are propelled by rechargeable battery units, without any other source of energy. These vehicles connect to an electrical power source in order to replenish their energy. In addition to these three categories, there are additional kinds of electric cars, including mild-hybrid electric vehicles (MHEV) and fuel cell electric vehicles (FCEV). Figure 1[15] shows the projected annual growth of EVs (BEVs, PHEVs, and HEVs) from 2010 to 2050, including baseline (BS), moderate (MS), and stringent (SS) outcomes.

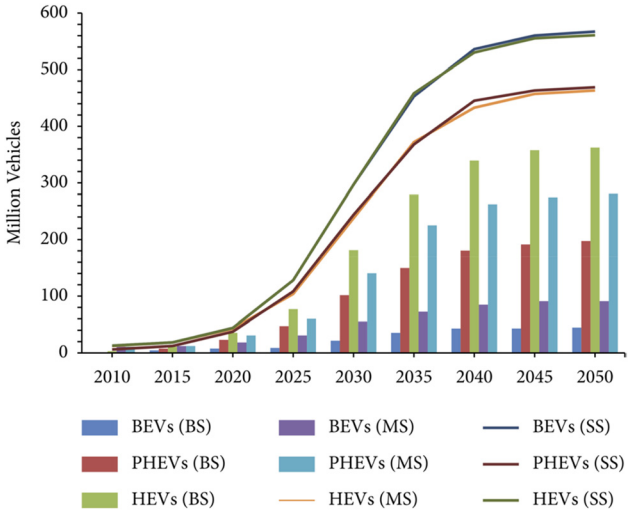

FIG. 1. Stocks of three types of EVs expected to expand at varying rates from 2010 to 2050.[15] Reproduced with permission from Falcão *et al.*, Appl. Energy **193**, 297–307 (2017). Copyright 2017 Elsevier.

One of the advantages of EVs is their affordable price. Over the past decade, various types of EVs have been produced by a diverse range of manufacturers, underscoring a burgeoning demand for these vehicles in the market. Figure 2 depicts the popular EVs that have been produced since 2014–2023, as updated by Hossain *et al.*[1] The statistic offers an estimation of the duration required to charge the car from 0% to 80% capacity, based on the various charging procedures. Many studies have concluded that the optimal range of EV battery state of charge is between 20% and 80%.[16] Other authors suggested that the state of charge of EV batteries should be between 10% and 90%.[17] Fundamentally, there are three levels of charging voltage for EV cars:

TABLE I. Comprehensive review of several kinds of EV.

Types	BEV	HEV	PHEV
Drive section	Electric machine	Electrical machine, internal combustion engine (ICE)	Electrical machine
Energy sources	Battery, ultracapacitor	Battery, ultracapacitor, ICE unit	Fuel cell
Energy supplements	Electricity and power system	Electricity and power system, gasoline station	Hydrogenide

21 October 2024 08:24:33

© Author(s) 2024

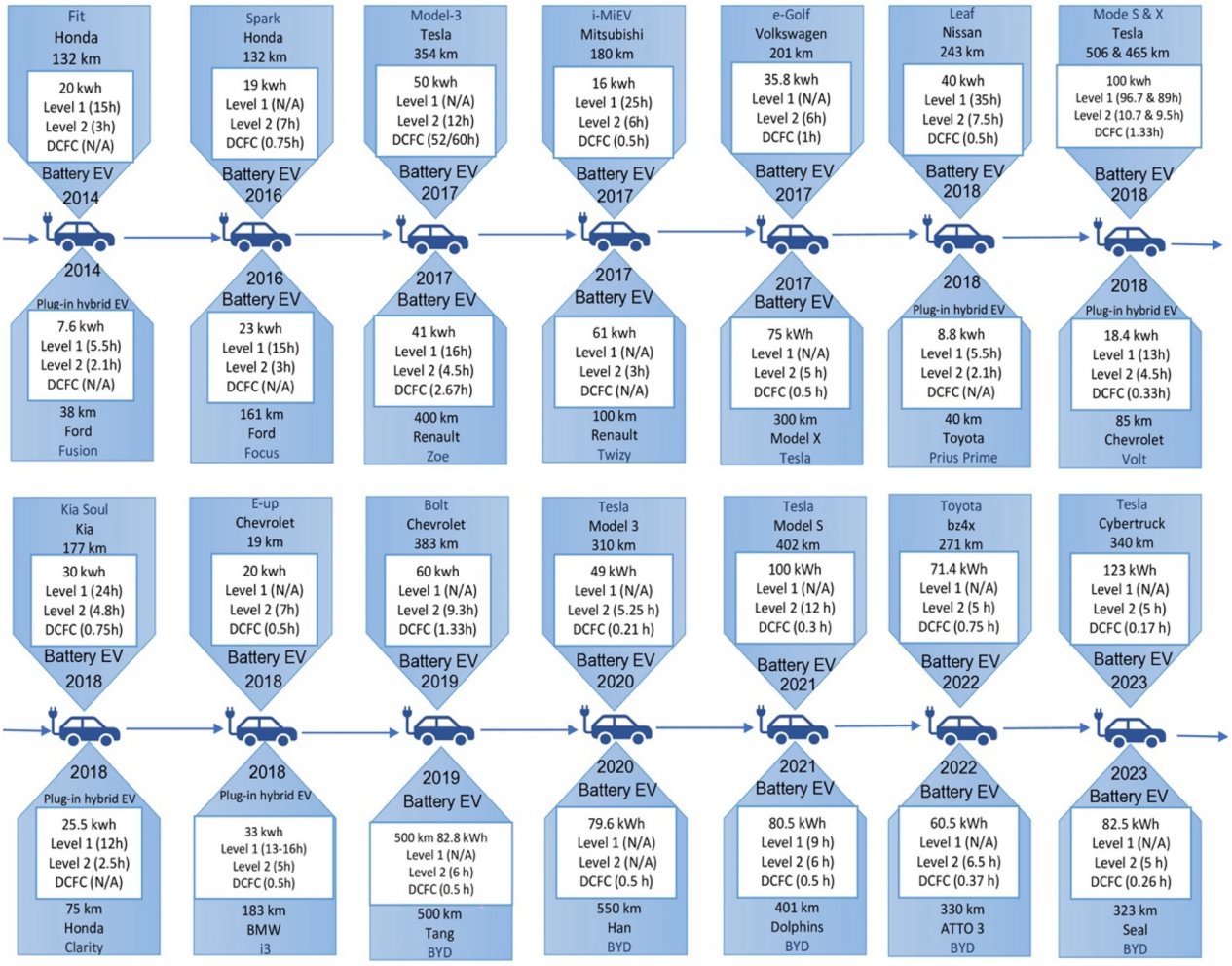

FIG. 2. Popular electric vehicle produced from 2014 to 2023.[20–33] Hossain *et al.*, Complexity **2022**, 3304796 (2022), licensed under a Creative Commons Attribution (CC BY) License.

the first level charging voltage ranges from 110 to 120 V, the second level ranges from 220 to 240 V, and the third level, also known as DC fast charging (DCFC), ranges from 200 to 800 V. Notably, the drive range of an EV is closely correlated with the charge level of its battery. Several automobile models can retain their battery charge for an additional 200–400 km of driving even after being driven for 100 km. Indeed, some contemporary electric car models have a driving range exceeding 400 km.[18,19]

To accomplish electrification in transportation, it is necessary to decrease the weight of the vehicles and improve their operation efficiency. This can be achieved by replacing silicon-based power devices in EVs with wide bandgap (WBG) technologies, such as silicon carbide (SiC) and gallium nitride (GaN), which are well-known for their superior power switching operation compared to silicon (Si).[34,35] Despite the extensive utilization of Si and SiC in power device applications, they possess significant disadvantages. Si, in its pure state, exhibits neither good conductivity nor insulation properties, rendering it unsuitable for use as an electrical material without being combined with other substances. The electron mobility of Si is reduced, leading to decreased device performance. Si devices generally have a higher power consumption. SiC incurs significant manufacturing and processing expenses due to the challenges associated with producing big wafers, limited supply, increased complexity in gate drive, and reduced switching speed. Compared to Si and SiC, GaN possesses remarkable characteristics, such as a high saturation drift velocity and a high critical breakdown field. Furthermore, it possesses a significant critical drift field. A high critical field is essential for capturing higher blocking voltages and achieving shorter drift widths. Meanwhile, the drift velocity influences the frequency at which the devices are triggered to carry out their operations.[36]

There are many reviews[37–41] on the development of EVs that mention their importance and future perspectives; however, reviews that discuss in depth the contributions of WBG materials to EV technologies are scarcely available in the literature. This review has been

21 October 2024 08:24:33

© Author(s) 2024

prepared in a way that comprehensively covers the information about all the aspects of GaN devices for EVs, which could be useful to provide insights for researchers and scientists to accelerate their innovation for the improvement of EVs. This review begins with an introduction to EVs, followed by the anticipated demand for EVs. The following part covers a detailed structural discussion of GaN power devices and their essential characteristics, as well as the possibility of employing GaN in EVs with a comparison between conventional Si and SiC as power devices, which are the main power devices of an EV at the moment. Section II discusses the recent discoveries of power devices that are potentially being used in various components of a fully automated EV, such as the battery, energy storage system (ESS), auxiliary power unit, and motor drive, in addition to their use in different non-automotive vehicles such as electric aircraft, electric ships, electric railways, electric submarines, and heavy-duty vehicles. Finally, the challenges posed by GaN devices and potential solutions to overcome these shortcomings, along with conclusions and future prospects, have been addressed.

II. IS GaN THE FUTURE?

GaN semiconductors have emerged as a very promising technology in the field of electronics, presenting a multitude of benefits compared to conventional silicon-based semiconductors. Owing to its wideband gap properties, GaN material is well-suited for use in heavy-duty fields, including automobiles and aerospace telecommunications.[42] Essentially, GaN comprises a crystalline lattice structure including gallium (Ga) and nitrogen (N) atoms, as depicted in Fig. 3(a).[43] The energy gap of GaN has been experimentally proven to be three times larger compared to Si.[44] This characteristic enables the efficient movement of electrons and provides several advantages, including exceptional electron mobility and saturation velocity compared to Si and SiC, allowing them to function at elevated velocities, resulting in accelerated switching rates and facilitating the development of high-frequency devices.[44–46] This feature allows for effective power management, making them ideal for high-power tasks. Another exceptional characteristic of GaN semiconductors is their efficient heat conductivity.[44] The material effectively disperses heat, allowing for efficient thermal control in high-power applications. This feature aids in the prevention of excessive heat generation. Moreover, GaN's ability to withstand greater operating temperatures in comparison to silicon-based semiconductors enhances performance and reliability by minimizing the need for intricate cooling systems.[47] On this account, GaN devices can function at higher voltages while maintaining optimal performance, resulting in improved reliability and durability of the power devices. The comparison of material characteristics of GaN, SiC, and Si is presented in Table II and Fig. 3(b).[48]

GaN has the potential to enable the development of more compact and lighter electronics. GaN components possess a remarkable power density and the ability to be made smaller in size, allowing them to provide significant power outputs while taking up less physical space.[49] This benefit is especially significant in applications that need a small size and less weight, such as portable electronic devices and automotive systems. Figures 3(c) and 3(d) demonstrate the structure of a GaN-based power device in three-dimensions (3D) and two-dimensions (2D), respectively. The size of the GaN power device usually varies from 20 nm to 2 mm. Currently, there are two types of architectures under consideration for GaN-based power devices: lateral structures and vertical structures. The AlGaN/GaN high electron

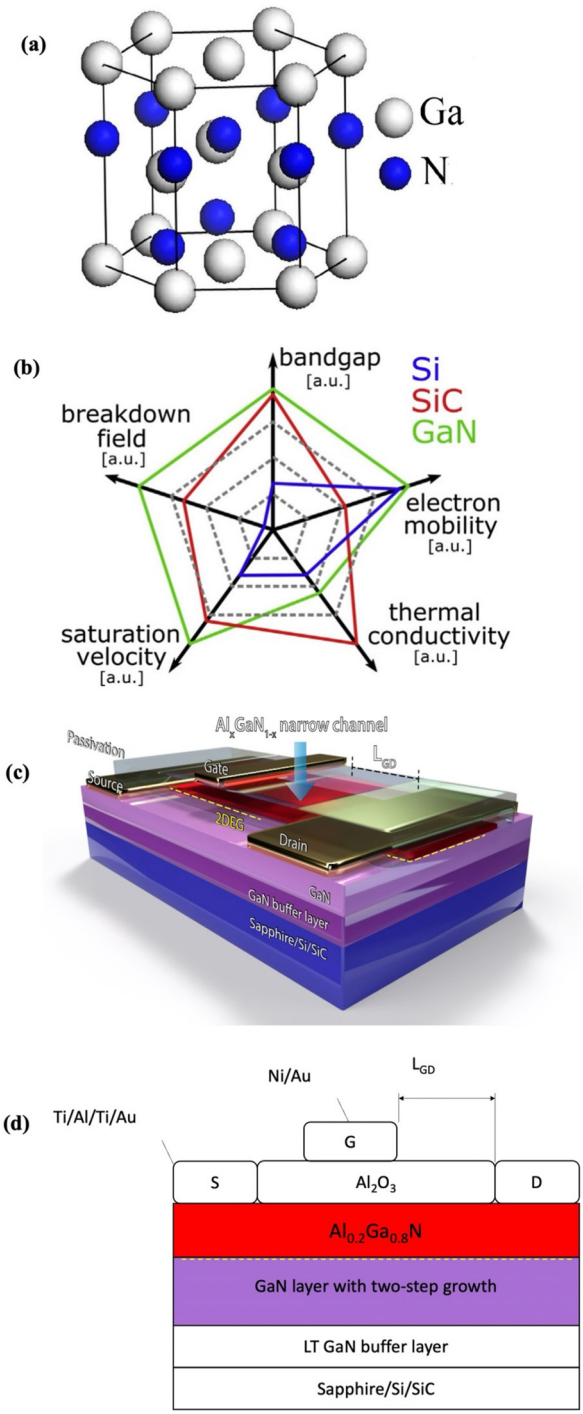

FIG. 3. (a) Structure of wurtzite GaN crystals.[43] Reproduced with permission from Qin *et al.* Crystals **8**, 428 (2018). Copyright 2018 MDPI. (b) Comparison of Si, SiC, and GaN power electronics material characteristics.[48] Reproduced with permission from Fatahilah *et al.*, Micro and Nano Eng. **3**, 59–81 (2019). Copyright 2019 Elsevier. (c) 3D model of a typical GaN device with 2DEG horizontal channel underneath the source and drain. (d) 2D model of a typical GaN device.[63] Reproduced with permission from Yusuf *et al.*, Crystals **13**, 90 (2023). Copyright 2023 MDPI.

21 October 2024 08:24:33

© Author(s) 2024

TABLE II. Comparison of Si with wideband gap materials SiC and GaN.

Parameter	GaN	SiC	Si
Electron mobility (cm^2/V g)	1800	900	1400
Energy gap (eV)	3.5	3.26	1.12
Breakdown electric field (MV/cm)	3.3	3	0.3
Thermal conductivity (W/cm K)	1.3	4.9	1.5
Saturation drift velocity (Mcm/s)	27	27	10

mobility transistor (HEMT) is the most favorable lateral structure, as shown in Fig. 4(a).[50] It operates by using a two-dimensional electron gas (2DEG) that is formed at the interface of an AlGaN/GaN heterostructure. The AlGaN/GaN structure exhibits a significant electron mobility of around 2000 cm^2/V·s and a high electron velocity, with a peak velocity of around 2.5×107 cm/s and a saturation velocity of approximately 1.3×107 cm/s. Furthermore, the AlGaN/GaN structure exhibits a sheet carrier density above $1 \times 1013\,cm^{-2}$, thanks to its robust piezoelectric and spontaneous polarization properties in III-nitride materials. AlGaN/GaN HEMTs have low on-resistance due to their high electron mobility and carrier density. Simultaneously, a vertical structure is also highly efficient in achieving low on-resistance and high breakdown voltage properties, similar to conventional Si-based power devices such as power metal oxide semiconductor field-effect transistors (MOSFETs) or insulated-gate bipolar transistors (IGBTs).[51,52] It has garnered growing interest in recent times. Rohm, a Japanese corporation, announced the development of GaN vertical MOSFETs. The schematic structure of the vertical GaN device is shown in Fig. 4(b). The University of California, Santa Barbara, revealed a distinctive configuration utilizing 2DEG carriers in the access area.[53] Toyota described the use of regrown p-GaN to limit the vertical current in their vertical constructions.[54] When comparing GaN-based lateral HEMTs to GaN-based vertical power devices, it has been observed that there are more and greater structural variances in the latter.

Enhancement-mode (normally off) power transistors are necessary for fail-safe design and circuit simplicity in power switching applications. Due to the presence of the native 2DEG channel, the GaN HEMT is naturally a depletion-mode (normally on) device. For voltage-source converters, this is unfavorable due to the possibility of shoot-through occurring at startup or when control power is lost. It was demonstrated by Lanford *et al.*[55] that gate recess etching can be used to achieve normally off AlGaN/GaN HEMTs. Subsequently, it was combined with an integrated dual-gate structure by Lu *et al.*[56] in order to achieve a higher breakdown voltage and lower contact resistance. Additionally, it was combined with a tri-gate structure by Lu *et al.*[57] in order to achieve enhanced gate control and lower off-state leakage. Various alternative techniques have been shown to produce enhancement-mode AlGaN/GaN HEMTs. These methods involve bandgap engineering for piezo neutralization,[58] as well as the incorporation of p-AlGaN[59] and InGaN[60] layers beneath the gate metal.

In contrast, the normally off technology for GaN vertical power transistors is contingent upon the particular device structure that is being utilized. GaN vertical MOSFETs are able to readily generate a threshold voltage that is higher than 3 V.[52] They are normally off by means of their intrinsic characteristics, which have become one of their main advantages over lateral HEMTs. However, the normally off design continues to be problematic for vertical GaN transistors that make use of the 2DEG at the AlGaN/GaN interface. This is due to the fact that the threshold voltage is still intrinsically negative. Although it is possible to employ the principles that were outlined before for lateral devices, further development and refinement are still required. Okada *et al.*[61] showed that it is possible to obtain a normally off operation by reducing the thickness of the regrown AlGaN in vertical structures. Such advancements are crucial for efficient power conversion, which is vital for maximizing performance and increasing the driving range of electric and hybrid cars. The GaN power device plays a crucial role in various components of an EV, including the energy storage system (ESS), charger, motor drive, and auxiliary power unit. Figure 5[62] shows the applications of GaN devices in different components of EVs.

Any power electronic GaN should have as its primary objective to maximize the amount of the off-state breakdown voltage (BV) while simultaneously minimizing the dynamic on-resistance R_{on}, $R_{on,dyn}$, and parasitic capacitances associated with the device. Scaling up the

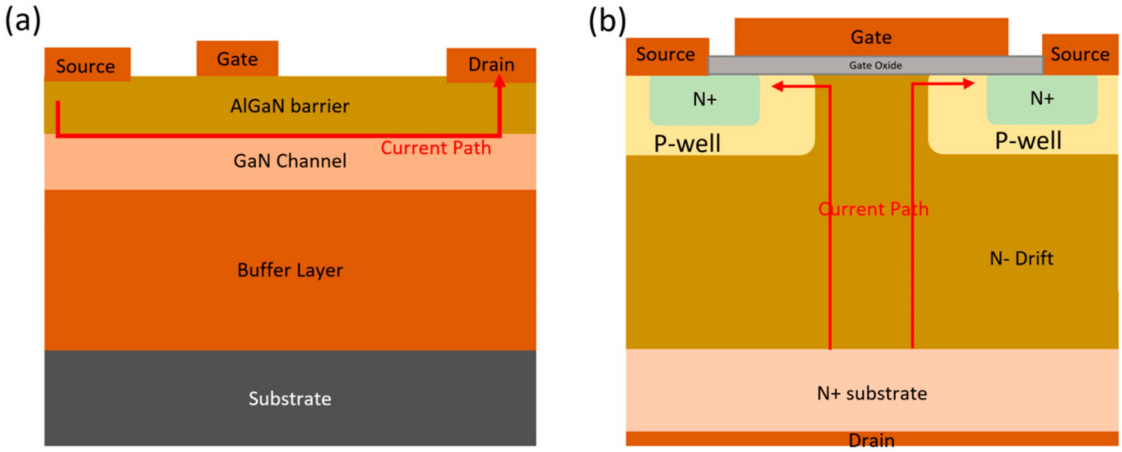

FIG. 4. Schematic structures of (a) lateral GaN device and (b) vertical GaN device.[50] Reproduced with permission from Langpoklakpam *et al.* Micromachines **14**, 1937 (2023). Copyright 2023 MDPI.

21 October 2024 08:24:33

© Author(s) 2024

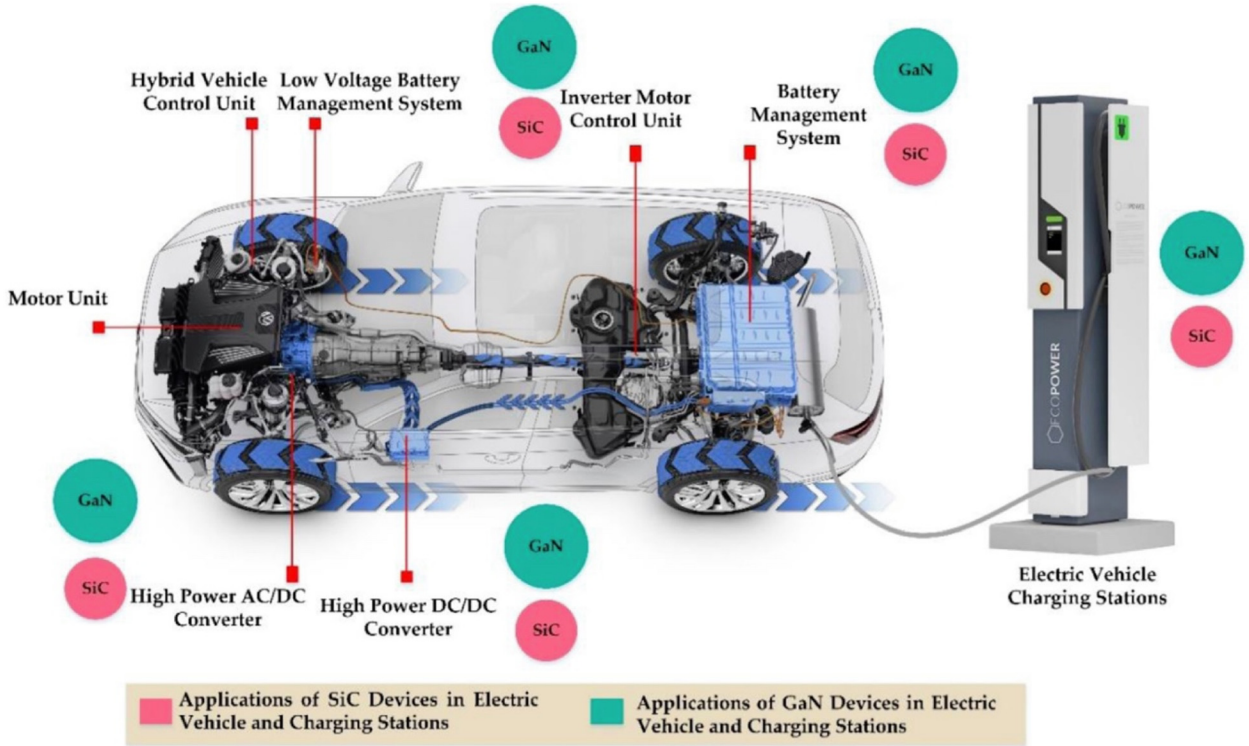

FIG. 5. Applications of GaN and SiC in different EV components.[62] Reproduced with permission from Rajendran *et al.*, J. Energy Storage **42**, 103099 (2021). Copyright 2021 Elsevier.

component by increasing the gate-drain distance (L_{gd}) is one method that may be utilized to achieve the goal of raising the BV. This results in an increase in the area of the access region, which in turn leads to a greater R_{on} and, consequently, on-state losses. The equation for calculating the specific (R_{on}) is[64]

$$R_{on} = (R_{gs} + R_{ch} + R_{gd} + 2R_{con}) \times (L_{gs} + L_{ch} + L_{gd} + 2L_{con}), \quad (1)$$

where R_{gs} is the resistance between the gate and the source, R_{ch} is the resistance of the channel, R_{gd} is the resistance between the gate and the drain, R_{con} is the resistance of the connection, L_{gs} is the length between the gate and the source, L_{ch} is the length of the channel, L_{gd} is the length between the gate and the drain, and L_{con} is the length of the connection. The relation that determines the lowest specific on-state resistance ($R_{on,sp}$) in HEMTs for any one particular BV is[65]

$$R_{on,sp} = \frac{BV^2}{q m_n n_s E_{crit}^2}, \quad (2)$$

where q, μ_n, n_s, and E_{crit} are the elementary charge, electron mobility, sheet carrier concentration, and critical electric field of GaN, respectively.[66] Nevertheless, in a practical device, there are a large number of material growth and device processing characteristics that can cause the $R_{on,sp}$-BV relation to depart from the ideal correlation. These characteristics, including defects in the crystal structure, dopants, surface impurities, and the quality of the dielectrics (and their interfaces) deposited on the surface of the III-nitride, can have a detrimental impact on the BV of the device as well as the critical electric field of GaN.[67] This might appear as an increased off-state leakage current, dielectric breakdown, or a rapid current spike caused by an accidentally additional leakage channel in the III-nitride heterostructure.[68] A high BV vertical GaN-on-GaN p-i-n diode with a modified mesa structure was proposed by Ho *et al.*[69] They produced vertical GaN p-i-n diodes that were grown on substrates that were free-standing GaN (FS-GaN). Thick GaN epi-layers were produced on the FS-GaN substrate as a result of this uniform epitaxy while maintaining a high crystalline quality. With a high BV of 2.98 kV and a low specific on-resistance of 0.85 mΩ cm^2, the vertical GaN p-i-n diode was demonstrated.[68] Likewise, low on-resistance high BV GaN diodes on low dislocation density GaN substrates were introduced by Sumiyoshi *et al.*[70] In this instance, they created FS-GaN substrates with low dislocation density to create vertical GaN Schottky barrier diodes (SBD). The SBDs had a specific on-resistance of 0.71 mΩ cm^2 and a BV of nearly 1100 V.

Occasionally, in GaN HEMT devices, a negative bias is required to turn off the devices, which is one of the major issues in the power electronics field. To create a normally off device, threshold voltage (V_{th}) is an important parameter because having a lower threshold voltage can improve the switching frequency of the GaN device. A lower threshold voltage can also lower power consumption, which means there is no need to offer additional voltage, making it less expensive in terms of power, as shown using[71]

$$V_{th}(x) = \varphi_B(x) - \Delta E_c(x) - \frac{s(x)}{\varepsilon_0\, \varepsilon_{AlGaN}(x)} t - \frac{q N_D}{\varepsilon_0\, \varepsilon_{AlGaN}(x)} (t)^2. \quad (3)$$

21 October 2024 08:24:33

© Author(s) 2024

In this equation, φ_B (x) represents the Schottky barrier height, $\sigma(x)$ represents the polarization charge at the AlGaN/GaN interface, ΔE_C (x) represents the conduction band discontinuity at the AlGaN/GaN interface, ε_{AlGaN} (x) represents the AlGaN layer permittivity, ε_o represents the permittivity vacuum, t represents the AlGaN thickness, and N_D represents the doping.

Another factor in the electro-thermal model for GaN vertical MOSFETs is the charge at the interface between the channel and gate dielectric. The inclusion of interface charge arises from the significant disparity between the V_{th} values obtained through theoretical calculations and those observed in experimental devices. In theory, the threshold voltage of a GaN MOSFET can be expressed as[72]

$$V_{th} = \frac{Q_s}{C_{ox}} + 2\,\varphi_B, \tag{4}$$

where Q_s is the total space charge per unit area in the semiconductor, φ_B represents Schottky barrier height, and C_{ox} is the insulator capacitance per unit area.

Minimizing power loss is important for EVs, as it directly correlates with increased efficiency. Increasing the efficiency of a 200-kW inverter from 95% to 99% results in a decrease in power loss from 10 to 2 kW. This improvement is advantageous for both the traction power and cooling system needs. The input and output power can be evaluated as[73]

$$P_{in} = V\,I, \tag{5}$$

$$P_{out} = I^2 R_L, \tag{6}$$

where V is the breakdown voltage, I is the current, and R_L is the load resistance.

Switching frequency is a critical characteristic in the design and operation of GaN power devices. The switching frequency of an inverter or converter refers to the frequency at which the switching mechanism is activated and deactivated. The frequencies commonly seen are in the range of a few kilohertz to several megahertz (20 kHz–2 MHz). Higher switching frequencies lead to a decrease in the size of related supporting components, including inductors, transformers, resistors, and capacitors. It also minimizes the space needed on the circuit board and casing. The power dissipation of switching components, such as diodes, transistors, and thyristors, as well as the inductive and capacitive parasitic elements and electromagnetic interference (EMI), is directly influenced by the switching frequency. Due to higher power densities, switching frequencies increased, which raised switching losses. Consequently, these losses impose a constraint on the highest achievable switching frequency in practice. A high-frequency PWM Buck converter using GaN-on-SiC HEMT was proposed by Rodriguez *et al.*[74] Targeting switching frequencies in the tens of megahertz range, they have investigated the usage of GaN-on-SiC HEMTs in traditional pulse-width modulated switched-mode power converters. The efficiency and device sizing limits of this technology are examined, and design principles and guidelines are provided to fully utilize the devices' capabilities. The results for both integrated and discrete-device implementations of synchronous Buck converters are shown. These implementations can supply more than 10 W of output power from a voltage of up to 40 V with efficiencies of more than 90% at switching frequencies up to 40 MHz and more than 95% while operating at 10 MHz. Ueda *et al.*[75] proposed GaN transistors on Si for switching and high-frequency applications, employing novel epitaxial structures such as superlattice interlayers grown by metal organic chemical vapor deposition (MOCVD) to relieve strain and eliminate cracks in GaN over large-diameter Si substrates up to 8 in. The manufactured GaN transistors provide outputs of 203 W at 2.5 GHz and 10.7 W at 26.5 GHz. The switching frequency is denoted by[76]

$$f_{sw} = \frac{1}{T_{on} + T_{off}}, \tag{7}$$

where f_{sw} is the switching frequency, T_{on} is the on time of the power device, and T_{off} is the off time of the power device. On the other hand, if a device is in power saving mode (PSM), the switching frequency will depend on the load (L), current (I), and input and output voltages (V_{IN} and V_{OUT}). The switching frequency for those kinds of power-saving mode devices can be calculated as[77]

$$f_{psm} = \frac{2\,I_{out}}{t_{ON}^2\,\dfrac{V_{IN}}{V_{OUT}}\,\dfrac{V_{IN} - V_{OUT}}{L}}. \tag{8}$$

Power density is a measure of how much power can be processed in a given space, which implies that the power generated is proportional to the area occupied by the system. Having a high power density reduces space requirements, provides maximum output power, and reduces costs. Power density can be assessed using[78]

$$P_{density} = \frac{V\,I}{L\,W}, \tag{9}$$

where V is the voltage, I represents the input current, L is the length of the circuit board, and W is the height of the highest component present on the board.

Precise thermal management is significant for achieving the best possible performance and durability of power electronics systems based on GaN technology. Elevating the temperature will accelerate the deterioration of GaN transistors and diminish their resilience. In order to ascertain the temperature levels reached by GaN devices during the rated operation of a power converter, it is necessary to construct a thermal model. The Laplace equation, as depicted in Eq. (10),[79] is utilized to model the thermal characteristics of power electronic components by representing temperature as T. The assumptions of continuous, laminar, and incompressible heat flow are made, in line with the principles of heat transfer,[79]

$$\nabla^2 T = \frac{\delta^2 T}{\delta x^2} + \frac{\delta^2 T}{\delta y^2} + \frac{\delta^2 T}{\delta z^2}. \tag{10}$$

Thermal conductivity is a parameter that quantifies a substance's capacity to conduct heat. It is determined by calculating the amount of heat that can be transferred through a certain thickness of the material, per unit area, and per unit temperature difference. By applying the notion of thermal conductivity, one may calculate the thermal resistances (R_θ) of each location in power electronic switches as[79]

$$R_\theta = \frac{L}{k\,A}, \tag{11}$$

where L is the thickness of the material, k is the thermal conductivity, and A is the surface area.

In order to accomplish energy consumption reduction, enhance heat dissipation, and lower the size and weight of the device, efficiency

21 October 2024 08:24:33

© Author(s) 2024

is an important factor for GaN devices. Increased efficiency results in reduced energy losses, leading to long-term cost savings for the system. In scenarios where power consumption is a notable consideration, such as in data centers or EVs, enhancing efficiency can result in large financial savings. In power electronics systems, any energy that is not effectively transformed is frequently released as heat. Enhancing efficiency results in a decrease in heat production, hence diminishing the requirement for intricate and costly cooling systems. Reducing the size and weight of power electronics components is crucial in various applications, particularly portable gadgets and EVs. Increased efficiency enables the creation of smaller systems since less space is required for heat dissipation and cooling technologies. The efficiency of a power device is[80]

$$\eta = \frac{P_{out}}{P_{in}} x\, 100\%. \tag{12}$$

GaN technology is crucial in developing not only in the EV industry but also in the aerospace and telecommunications industries. GaN devices facilitate high-frequency operation, resulting in amplified bandwidth and improved data transmission capabilities. This has the utmost significance for upcoming wireless networks, satellite communications, and radar systems.[81] In addition, GaN semiconductors are also pivotal in the progress of energy efficiency and renewable energy. GaN power devices enhance power conversion in solar inverters and wind turbines, resulting in improved system efficiency and facilitating the integration of renewable energy sources into the power grid.[82]

III. GaN-BASED POWER DEVICES IN EV SYSTEM

A. Energy storage system (ESS)

An energy storage system is essential to an EV operation. The current trend of EVs uses renewable energy stored in the vehicle batteries, which is converted into rotational mechanical energy by the electric motor propulsion system to power the vehicle. Hence, the performance of the EVs is determined by the efficiency of electric motor, converter, and battery system integration. To accomplish high efficiency and improve power density of the electric motor, novel motor materials, rotor structure, and stator winding have been used in the battery packing system. Cutting-edge materials such as GaN have been researched and applied to the converter to improve the efficiency of the EV energy storage system.

Lithium-ion (Li-ion) and nickel-metal hydride (NiMH) batteries are two unique battery technologies that are often used in EVs. Li battery is an irreplaceable source of energy that is used in a variety of EVs, including the Nissan LeFeng and the Mitsubishi iMiev. On the other hand, it is important to point out that nickel-metal hydride batteries are utilized as the primary source of energy in half of all today's EVs, including the Toyota Prius.[83] It is vital that the energy source from the battery continuously flows to the EV without interruption. Thanks to advancements in the electronic field, the supplemental charge of the EV battery can be monitored, allowing for better management of energy usage and efficiency. The optimum level for vehicle operation is generally agreed upon to be around 20%, according to the opinions of specialists. As a consequence of this, it is strongly suggested that the emission zone should not go higher than 80% in order to keep the level at an acceptable and sustainable standard. Therefore, it is important to highlight the fact that the state of a charge that is gradually being regenerated may be determined. Essentially, the energy storage system

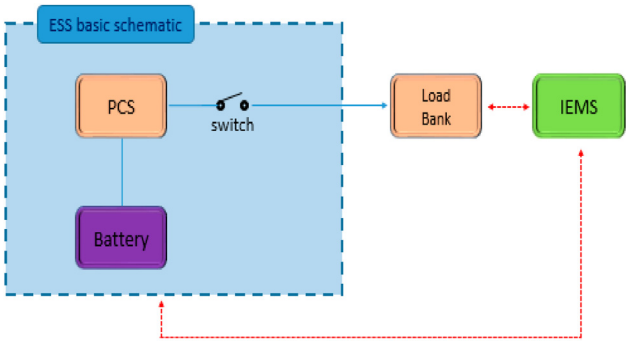

FIG. 6. Block diagram of energy storage system in electric vehicle.[84] Reproduced with permission from Roh *et al.*, J. Mar. Sci. Eng. **7**, 230 (2019). Copyright 2019 MDPI.

(ESS) consists of a secondary battery (lead-acid battery) and a power conditioning system (PCS). It is built using a bidirectional connection system with an intelligent energy management system (IEMS), which is a control system to monitor voltage, current, and the system's state in real time. In this system, the PCS plays triple functions: (1) to monitor the state of charging (SoC) of batteries in real time; (2) to control temperature, current, and voltage to ensure the stability of the system; and (3) as a surge protection that prevents overcharging/overloading of the batteries. Figure 6 illustrates the complete system of an energy storage system.

Numerous and continuous efforts have been made to improve the battery-based ESS. The safety, reliability, and lifespan of an EV battery are determined by the battery's SoC and its state of health.[85] Customers are likely to be more receptive to the transition toward the electrification of transportation if there is a large improvement in the range of electric cars that can be driven on a single charge as a result of advances in battery technology. EVs often make use of batteries that have a capacity that is far greater than what is necessary because of the desire to achieve a greater electric supply, accordingly contributing to greater driving range. However, this results in a significant increase in the overall size of the battery. Therefore, it is essential to employ battery components that have a high energy density,[86,87] as this will allow the dimensions and weight of these batteries to be reduced. The use of wide bandgap materials such as GaN devices in power converters of hybrid energy storage system (HESS) has enabled the reduction of the overall dimension and weight of the HESS. Their low conduction resistance and high-frequency operation make possible high-efficiency energy storage while reducing the size of power converters. Several studies have reported the utilization of GaN HEMT in their power converter designs to achieve improved power efficiency, energy density, and specific energy at the system level. For example, Ander *et al.*[88] introduce a HESS that utilizes lithium-ion (Li-ion) and lithium–sulfur (Li–S) battery modules together with a GaN-based DC–DC converter. Their work relies on analyzing the experimental data from a HESS prototype that demonstrates exceptional energy and power capabilities across several driving scenarios. The HESS consists of a lithium titanate oxide (LTO) anode battery, which ensures high power demands, and a module utilizing innovative Li–S technology, designed to enhance specific energy capacity. A GaN semiconductor-based bidirectional power converter was created to establish a connection between

21 October 2024 08:24:33

© Author(s) 2024

two batteries. The GaN-based power converter they designed achieves a high efficiency of 96.5% while running at a frequency of 300 kHz, and it has a decreased size of 0.4 l. In addition, the performance of the constructed HESS prototype is assessed by experimental testing using typical automobile profiles, across various driving conditions. The HESS prototype demonstrates a 5.56% improvement in energy density and a 28.21% increase in specific energy compared to a battery system consisting only of Li-ion cells. Abdullah *et al.*[89] introduced a soft switching phase-shifted full bridge (PSFB) converter utilizing GaN HEMT devices. This study empirically evaluates the benefits of employing GaN HEMT devices in the high-frequency, high-power DC–DC converter. Initially, the GaN HEMT's dynamic performance is assessed under various operating situations. Abdullah *et al.*'s work also introduced a unique approach to achieve soft switching in a zero-voltage zero-current switching (ZVZCS) PSFB converter. The suggested method utilizes the output parasitic capacitance (*Coss*) of the GaN devices and the transformer leakage inductance (LLK). A prototype of a 5-kW GaN-based PSFB with a frequency range of 100–250 kHz, voltage range of 400/600 V, was constructed and evaluated. To evaluate their power and also frequency, they have used Eq. (13) for maximum output power and Eq. (14) for frequency as follows:

$$P_{MAX} = \frac{T_j + T_c}{R_{th}}, \tag{13}$$

where T_j is the junction temperature, R_{th} is the total thermal resistance, and T_c is the case temperature.

$$f_{sw} = \frac{(100\% - \beta)P_{MAX} - P_{cond}}{P_{sw}}, \tag{14}$$

where P_{cond} is the conduction loss and P_{sw} is the switching loss.

The prototype demonstrated excellent dynamic performance across a wide range of load powers and achieved an impressive converter efficiency of up to 98.18%. Figure 7(a) compares the measured efficiencies of the proposed converter at frequencies of 100, 200, and 250 kHz. The efficiency exhibited a progressive increase across all switching frequencies at 4100 W. The accomplishment of ZVZCS results in enhanced efficiency across a broad spectrum of power levels. The loss distribution of the proposed converter is illustrated in Fig. 7(b) for various output powers and two distinct switching frequencies. Additionally, Fig. 7(c) depicts the loss distribution of the proposed converter at a power output of 5 kW and varying switching frequencies. Notably, GaN HEMT devices are able to function at 40% of their maximal power dissipation even when running at a high switching frequency of 250 kHz. Similarly, Yoo *et al.*[90] demonstrated a GaN HEMT-based PSFB converter. This research incorporates a secondary synchronous rectifier into the converter by utilizing GaN HEMT technology. The proposed converter demonstrates that the switches are vertically arranged rather than planarly arranged. This arrangement was chosen to ensure that each switch leg faces vertically. Additionally, the inductance was reduced by placing the switches on the same floor as the gate driver, thereby minimizing the path of the gate driver. Furthermore, efforts were made to position the gate driver's GND and the switch's source pin in close proximity to each other. The 500-W converter operated at a voltage of 300 V/14 V, a frequency of 100 kHz, and achieved an efficiency of over 93%. The efficiency of the PSFB converter utilizing GaN HEMTs was enhanced by over 2% by comparing it to the efficiencies of conventional PSFB converters. Both of the mentioned PSFB converters exhibited a substantial level of efficiency. Table III shows the data for different converters for ESS based on recent studies.

Isolated bidirectional converter can serve as an alternative to improve EV's ESS. The commonly used architecture for isolated bidirectional DC–DC conversion is the dual active bridge (DAB).[98–104] It possesses the benefits of a minimal quantity of passive components, a symmetric construction, diverse modulation methods, and the possibility of gentle switching. Xue *et al.*[92] investigated DC–DC converter using 650 V GaN HEMTs for energy storage system (ESS) applications. The power stage being suggested is a bidirectional half-bridge center-tap with an active clamp circuit, controlled by phase shift. The revised dual-active-bridge configuration employed cutting-edge power device technology of GaN HEMT. In the proposed circuit design, the inductor is eliminated due to the permissibility of hard switching operation for the GaN device. An efficiency study was performed, and the system achieves a power density of 30 W/in.^{3} and a peak efficiency of 98.3% across a wide range of input and output voltages. Both soft-switching and hard-switching modes were successful in attaining minimal power loss while also achieving high power density.

B. On-board charger module

Essentially, to maximize driving range of an EV, it is crucial to maximize the usage of available energy from the battery pack. Therefore, the battery packs are manufactured at a wide range of voltage, which makes the high-efficiency, high-power-density on-board charger (OBC) module design significantly challenging. Resonant converters with variable switching-frequency control are substantially used in the state-of-art of power supplies, which can provide high efficiencies and high-power density. However, the traditional resonant converters have a major drawback; as the input or output voltage increases, the control frequency range also increases, resulting in an increase in the driving and magnetic components, which reduces conversion efficiency. Wide bandgap GaN semiconductors play a significant role in enhancing the efficiency of the OBC module, which can provide power density without sacrificing its performance.

Aiming for higher power, smaller size, and higher efficiency, a high frequency inductor–inductor–capacitor (LLC) resonant converter is a promising solution for multi-kilowatt on-board charger (OBC) for EV. Figure 8[105] shows the charging configuration of on board charger of EV. Among the various converters available for EV charging applications, the LLC resonant converter offers significant advantages. The inherent resonance of LLC converters allows for soft switching on both the primary and secondary sides, resulting in improved efficiency through the reduction of switching losses. Furthermore, employing an LLC topology results in the conservation of board space. Liu *et al.*[106] developed a high-frequency converter utilizing GaN devices and integrated magnetics. In this work, a second-stage LLC resonant converter was developed, and the LLC resonant circuit was employed as a direct-current transformer (DCX) to run the driver circuit at high efficiency. Furthermore, this study also developed and enhanced the primary- and secondary-side configurations and magnetic components in the LLC resonant converter. It also identified the most appropriate primary-side topology and secondary-side rectification architecture for an LLC resonant converter. Achieving a maximum efficiency of 97.03%, a 1-kW LLC resonant converter was developed with a 400 V input voltage, a 300 V output voltage, and a switching frequency of

21 October 2024 08:24:33

© Author(s) 2024

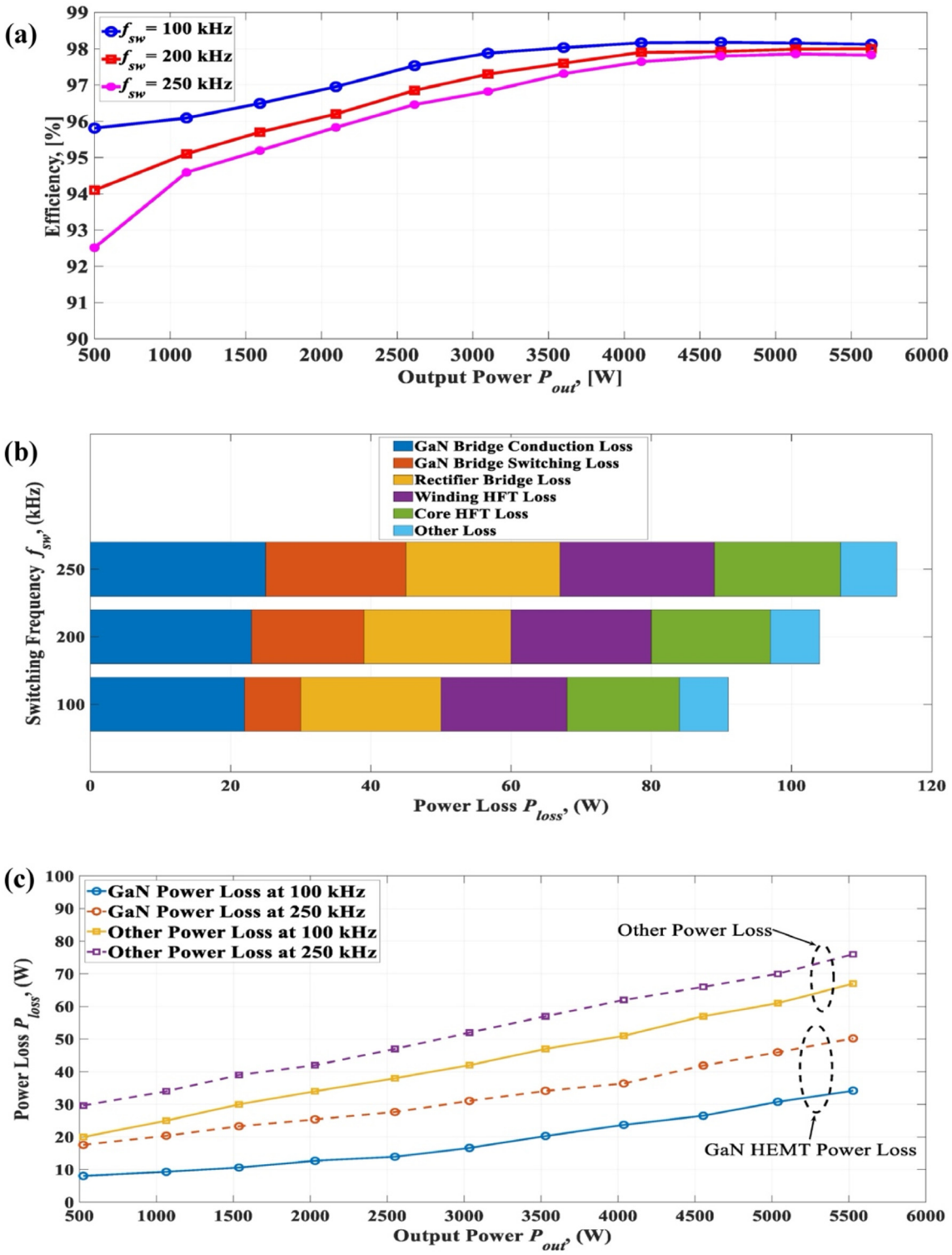

FIG. 7. (a) Efficiency vs output power under different switching frequency. (b) Detailed loss distribution of the proposed converter at 5 kW. (c) Loss distribution of the proposed converter at different output powers and two different switching frequencies.[69] Reproduced with permission from Awwad *et al.*, World Electr. Veh. J. **13**, 206 (2022). Copyright 2022 MDPI.

21 October 2024 08:24:33

© Author(s) 2024

TABLE III. Data of different converters for ESS from recent literature.

Device type	Voltage (V)	Power (kW)	Frequency (kHz)	Density (kW/l)	Efficiency (%)	Ref.
GaN PSFB	400/600	5.6	100–250		98.18	89
GaN HEMT PSFB	300/14	0.5	100		93	90
GaN CD PSFB	28/250	0.2	300		92.3	91
GaN bidirectional DAB	400/12	1	75	1.8	98.3	92
IGBT PSFB	360	10	75		97.8	93
PSFB	400	1.4	⋯	3.7	98.68	94
Bidirectional PSFB	400	0.3	100		93	95
DAB PSFB	400	3.3	⋯	2.5	98.12	96
MOSFET PSFB	36/14	⋯	7		96.6	97

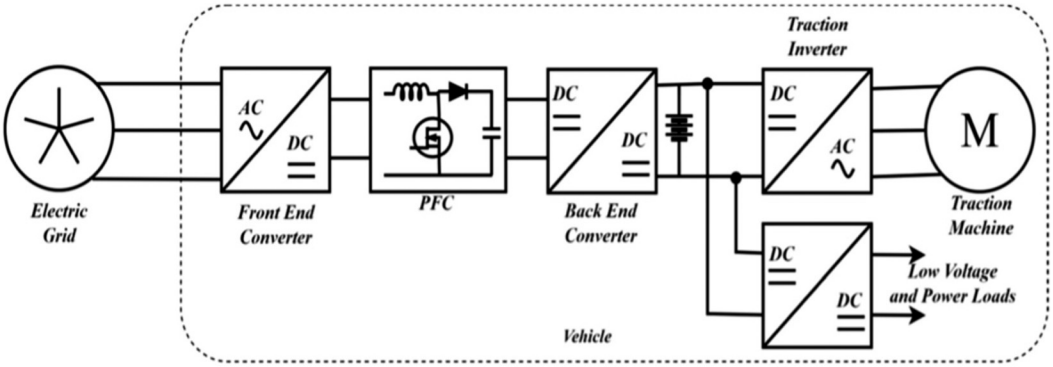

FIG. 8. On board charging configuration.[105] Reproduced with permission from Mustafa *et al.*, Energies **16**, 129 (2023). Copyright 2023 MDPI.

500 kHz. Figures 9(a) and 9(b) show the actual core size and circuit diagram, respectively. Figure 9(c) shows the measured power efficiency of the converter. Based on the observed data from the figure, the efficiency was determined to be 88% at a load of 10%. Once the load hit 20%, the efficiency peaked at 92%. Subsequently, the efficiency progressively rose to 96% when the load reached 40%. The efficiency thereafter achieved its maximum value of 97.03% at an 80% load and remained constant until reaching 100%. The transformer winding of the converter, operating at full load, recorded the greatest temperature of 78.6 °C. Figures 10(a)–10(c) display the temperature distribution of the power components on the primary side when operating at full load. The maximum temperatures recorded for these components are 38.1, 40.4, and 78.6 °C, respectively. Because the parameters of this paper are high-voltage to high-voltage, the loss may be mostly ascribed to the transformer, notably the transformer windings. Therefore, the temperature distribution of the overall converter will be centered on the windings of the transformer. This is due to the fact that the main or secondary switching components have zero-voltage-switch turn-on.

Similarly, Faizan *et al.*[107] developed a half-bridge LLC resonant GaN converter that is highly efficient and compact, specifically tailored for low-power applications. This study presents a GaN LLC resonant converter that is very efficient and compact. Figure 11(a) displays the proposed design of the LLC resonant converter. The LLC resonant tank has a magnetizing inductor (L_m), a resonant inductor (L_r), resonant capacitors (C_r), and a transformer. The transformer built for the planned LLC resonant converter consists of a single primary winding and two distinct secondary windings that are identical. C11 and C12, as well as D11 and D12, serve as output capacitors and rectifier diodes for the first secondary winding, respectively. C21 and C22, as well as D21 and D22, serve as output capacitors and rectifier diodes for the second secondary winding, respectively. When the LLC resonant converter is running at the resonance point or in the below resonance zone, the primary side half-bridge switches S1 and S2 can be turned on without any switching loss. ZVS is used to turn on both switches, and ZCS is used to turn on and off secondary side diodes. This reduces switching losses and increases system efficiency. The 240-W converter operates at 240 V and has a frequency of 75 kHz. The converter is specifically designed for low-power applications. The results indicate that the GaN HEMT-based resonant converter is superior in terms of efficiency and cost-effectiveness compared to the Si MOSFET-based resonant converter. Figure 11(b) depicts the efficiency comparison between the developed LLC resonant converter utilizing GaN HEMT and Si MOSFET. The GaN HEMT-based LLC resonant converter demonstrates a much higher efficiency of 98.5% and a power factor correction (PFC) of 0.99, as compared to the Si MOSFETs, which have an efficiency of 87.4% and a PFC of 0.92. Figure 11(c) illustrates a comparison of the losses between two solutions for LLC resonant converter. The results demonstrate that GaN HEMT offers notable benefits in terms of switching performance and conduction for the design of LLC resonant converters. The input power of the devices was

21 October 2024 08:24:33

© Author(s) 2024

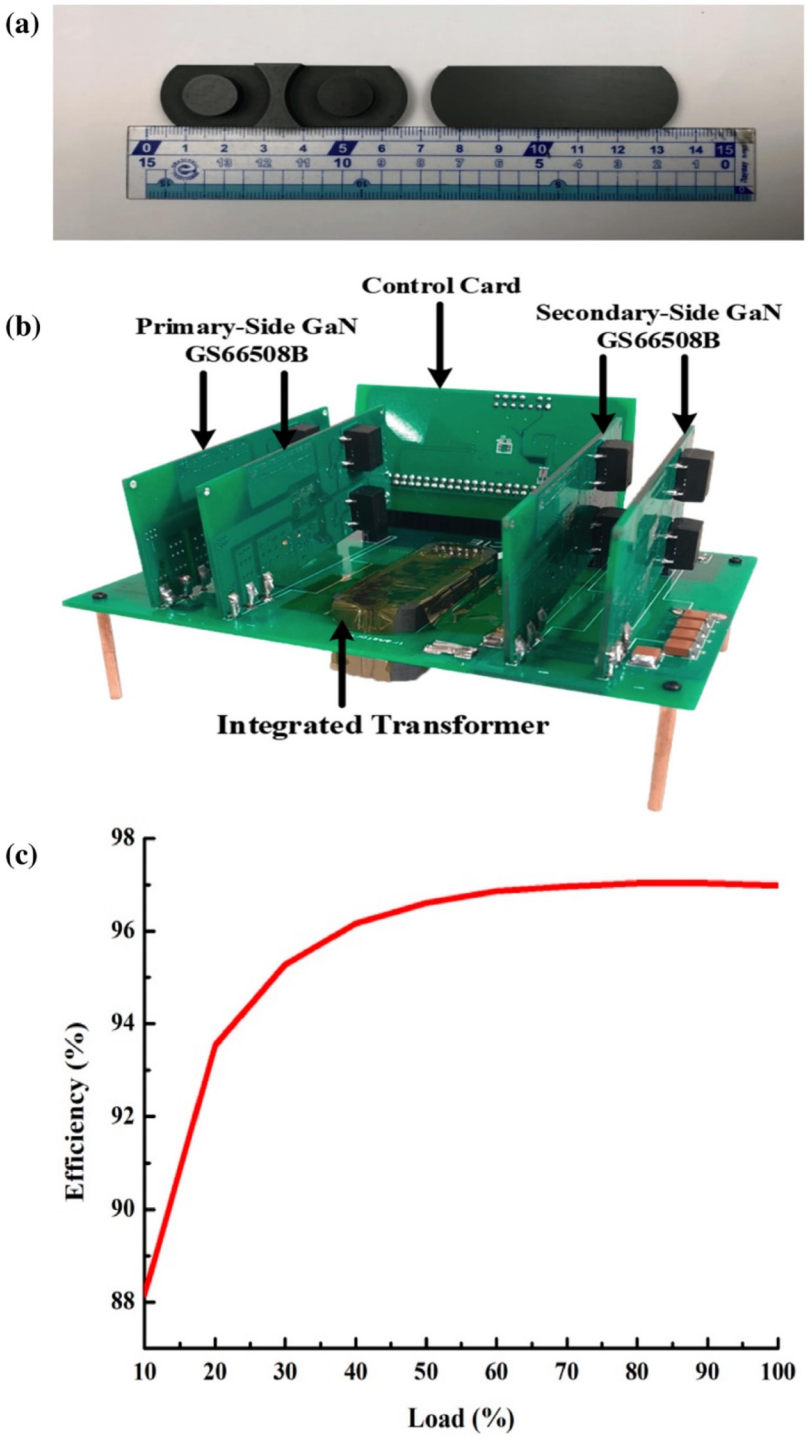

FIG. 9. (a) Experimental prototype of the (a) core structure and (b) circuit and (c) the measured power efficiency.[106] Reproduced with permission from Liu *et al.*, Energies **12**, 1781 (2019). Copyright 2019 MDPI.

calculated by Eq. (15), and the energy losses were calculated by Eq. (16). The GaN LLC resonant converter exhibits approximately 37% lower overall energy losses when compared to Si MOSFET solutions.

$$P_{input} = \frac{V^2}{16\,X\,L\,X\,f_r}\left[\frac{1}{2} - \frac{2\,X\,V}{3X\pi XV}\right], \tag{15}$$

where V is the bus voltage, and f_r is the resonance frequency.

21 October 2024 08:24:33

© Author(s) 2024

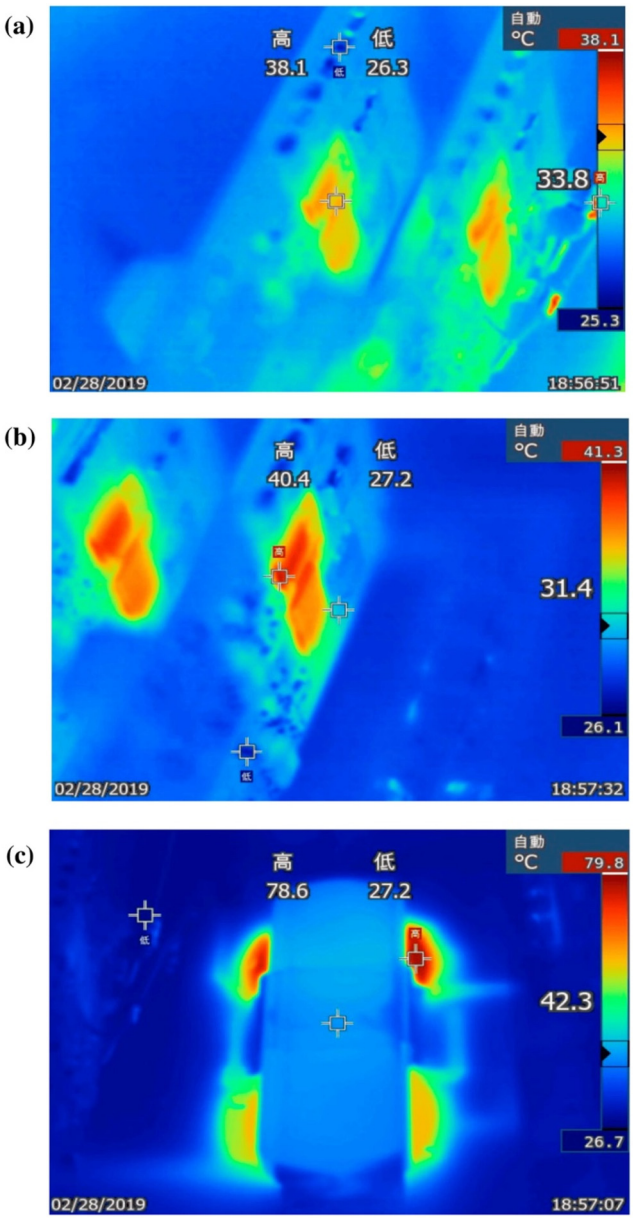

FIG. 10. Temperature of the LLC converter at full load: (a) primary-side GaN devices, (b) secondary-side GaN devices, and (c) core and winding of transformer.[106] Reproduced with permission from Liu *et al.*, Energies **12**, 1781 (2019). Copyright 2019 MDPI.

$$E_{loss} = \int_t^0 V_{ds}(t) i_{ds}(t)\, dt, \tag{16}$$

where V_{ds} is the drain source voltage, t is the time, and i_{ds} is the drain source current.

Sun *et al.*[108] also developed a compact GaN-based LLC resonant converter with outstanding efficiency. This study outlines a comprehensive design process for a 10-kW GaN-based LLC resonant converter, with the primary goals of achieving high efficiency and high-power density. The text provides a detailed illustration of the modular switching cell design, which incorporates paralleled 650 V, 60 A e-mode GaN HEMTs. It covers many aspects, such as layout considerations and thermal management. An uncomplicated methodology for designing a conventional heat sink is exemplified, along with a straightforward experimental approach to validate the calculated thermal resistance. This approach can also be applied to different devices or designs of converters. In addition, through the meticulous design of the converter assembly, the all-GaN-based LLC resonant converter achieves a peak efficiency of 97.9% and a power density of 131 W/in.^{3} (8 kW/l). The switching frequency used was 400 kHz, which accounts for less than 5% of the total loss due to its low turn off loss and ZVS characteristics. The two previously mentioned studies may have demonstrated good efficiency and improved power density; however, their proposal of a compact converter has resulted in complex circuit designs for each circuit. This complexity makes the overall converter design complicated and expensive, particularly for EV charger applications. Despite the remarkable results of the studies, further investigation is necessary to acquire a simple design of the converter with optimal efficiency. Table IV reports multiple findings on the different LLC converters for the OBC system.

Although the LLC resonant converter has numerous advantages, some challenges remain in its application to the OBC system. The conventional LLC converter lacks the ability to allow reverse power flow, which is essential for bidirectional applications due to its unbalanced resonant tank. Another limitation is the difficulty of achieving zero voltage switching (ZVS) under all circumstances. Furthermore, it is challenging to attain high power density magnetics while ensuring excellent manufacturability. In order to achieve a simple design and overcome the challenges of the LLC converter, many researchers have proposed bidirectional CLLC converters because they offer several advantages for battery charger in an EV. The interface circuit for battery charger is efficient due to its bidirectional power transmission ability and easy modulation strategy. The system's streamlined design enables efficient energy charging processes. Ammar *et al.*[110] proposed a GaN-based converter for plug-in EV OBC. This study introduces a bidirectional CLLC resonant converter designed for the DC–DC step in modular level-2 on-board chargers. The functioning of the system is analogous to that of the typical LLC converter, but with the inclusion of an LC tank on the secondary side of the transformer.[116,117] The converter may achieve resonance throughout the bidirectional mode by using a variable DC–bus voltage. In the grid-to-vehicle (G2V) mode, a low battery voltage range is handled by employing switching frequency modulation, which leads to a narrower range of DC–bus voltage. Consequently, this enables the use of 650 V GaN devices for the switches on both the main and secondary sides. A high-frequency prototype with a power output of 1 kW is conceived and developed. In order to connect the primary and secondary sides, half-bridge switch networks are utilized in their proposed converter design. The switch voltages are limited by the DC–bus and battery voltages. While the rectifying half bridge works in reverse conduction for the whole of the switching period, the inverting half bridge is switched at the switching frequency with a duty cycle of 50% and a defined dead time, regardless of the direction in which the power flow is flowing. ZVS is achieved when the inverting devices switch on, regardless of the load conditions. When the transformer leakage inductance is integrated into the

21 October 2024 08:24:33

© Author(s) 2024

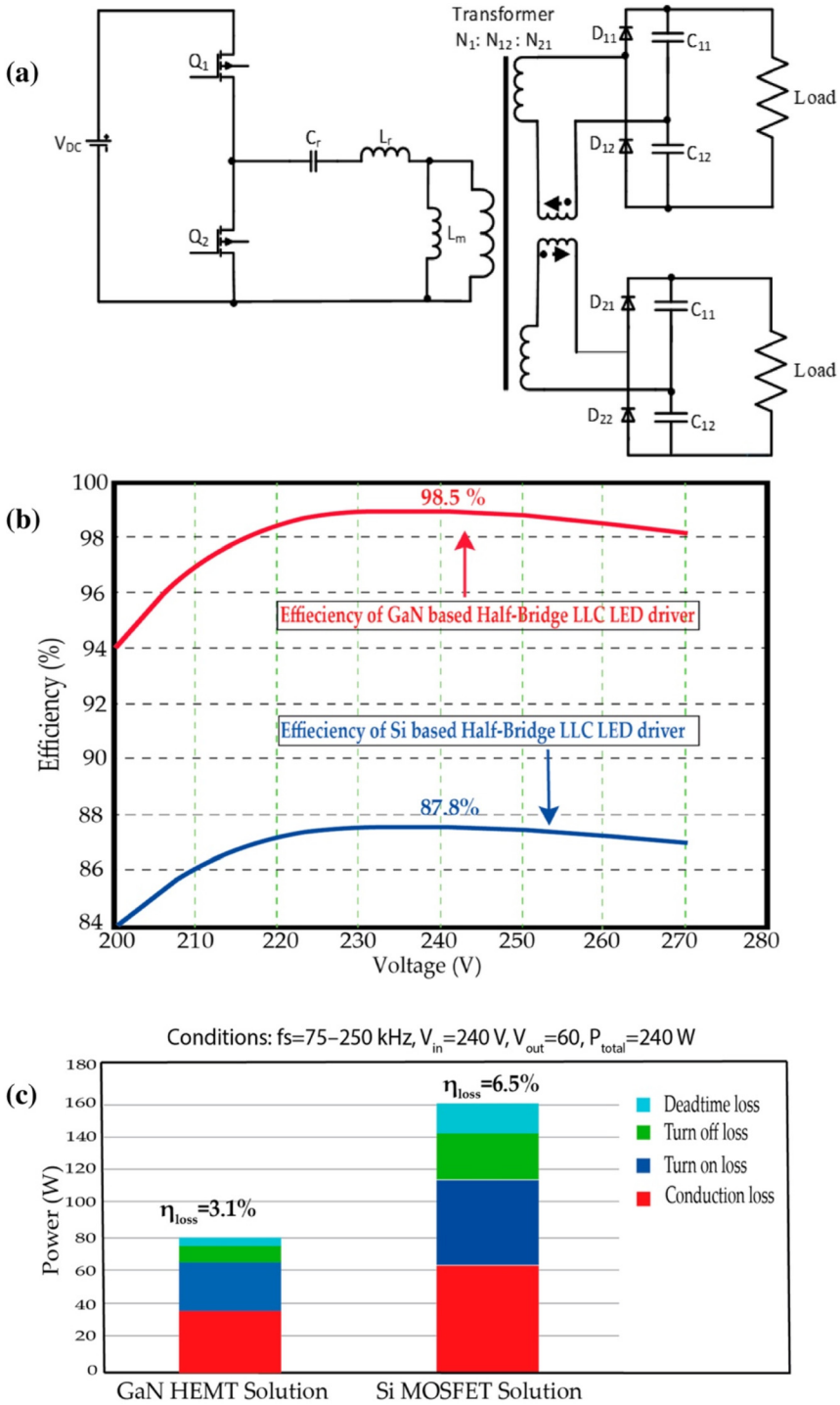

FIG. 11. (a) Proposed half bridge GaN LLC converter. (b) Efficiency comparison of designed LLC resonant converter with GaN HEMT and Si MOSFET. (c) Loss comparison of two solutions for LLC resonant converter.[107] Reproduced with permission from Faizan *et al.*, Electronics **12**, 2850 (2023). Copyright 2023 MDPI.

resonant tank, it becomes possible to integrate the resonant inductors within the transformer. This symmetric operation is provided across both power directions. The 1-kW prototype functions in ZVS over the whole load range, with an efficiency of up to 95.7%. The resonant tank series inductances are included into the transformer. The voltage input was measured at 650 V, while the switching frequency was determined to be 391 kHz. The prototype functions by operating the rectifying devices in reverse conduction, and the resulting loss is measured and

21 October 2024 08:24:33

© Author(s) 2024

TABLE IV. Different kinds of LLC converter for OBC modules based on recent studies.

Device type	Voltage (V)	Power (kW)	Frequency (kHz)	Efficiency (%)	Density (kW/l)	Ref.
LLC converter	400	1	500	97.03	···	106
Half bridge GaN LLC	240	0.24	75	98.5	···	107
GaN LLC	650	10	400	92.3	8	108
GaN LLC	380	0.5	···	97.85	18.9	109
GaN CLCC	650	1	391	95.7	···	110
GaN HEMT LLC	650	3.7	···	96.32	2.03	111
Micro inverter LLC converter	40/80	0.1	200	94.3	···	112
GaN SET LLC	200	0.6	250	97	···	113
LLC	400	3.7	500	98	···	114
GaN HEMT LLC	650	2.5	130	98.3	···	115

quantified. The high-frequency transformer incorporates the series inductances of the resonant tank, resulting in a reduced number of components and enabling high power density, therefore resolving the issue of reverse power flow. One-third of the overall power loss is also expended in the process of rectification, creating a compromise between efficiency and the factors of simplicity, cost, and production.

Wireless charging is one of the promising solutions to improve convenience for EV users. Wireless charging, also referred to as in-motion charging, allows for charging EV battery while driving in the transportation network. EV wireless charging A wire coil that is embedded into the surface of the parking lot serves as the conduit for the passage of an electric current. The movement of electric current causes the generation of a magnetic field, which in turn makes it easier for power to be transmitted between the primary and secondary coils. It is possible for the EV to be charged by elevating it above the charging equipment that has been installed on the ground in the area that has been allocated for parking.[118] As a result of these prevalent trends, wireless power systems are undergoing a transition from their current state as simplistic charging stations to their future state as viable power sources. This goal may be reached by increasing the power capacity of those systems while concurrently extending their operating coverage. Compared to amplifiers that are based on Si MOSFETs, amplifiers that are based on GaN have a wider range of imaginary impedance. Recent developments in coil technology and the use of higher power amplifiers, such as GaN MOSFETs as an alternative to Si devices, have made it more likely that large-scale wireless power distribution systems will be able to be designed.[119] The high frequency characteristic of GaN converters, in particular GaN HEMT, is another benefit when using wireless charging technology. Yang *et al.*[120] designed a GaN HEMT-based bipolar DC–DC converter that operates at a high frequency and has a high-power density. Here they made use of a Cuk converter in addition to a single-ended primary converter (SEPIC). The SEPIC converter offers the advantage of being able to operate as both a buck and boost converter. Additionally, it possesses a limited number of active components, a simple controller, and clamped switching waveforms that ensure operation with little noise. For Cuk converter, it possesses the capability to manage a diverse range of input voltages, uninterrupted input and output currents, as well as diminished electromagnetic interference (EMI). They have integrated the two converters into a microgrid that is of the bipolar type and operates at low voltage. Their experimental findings indicate that the power density is 35.23 W/in.^{3}, and the highest efficiency can reach 92.7% with a frequency of up to 1 MHz. Rezk and his team[121] have simulated an alternative design of GaN HEMT converters for wireless power transfer. A novel differential power oscillator has been proposed, utilizing a differential class-E power amplifier operating at the 433 MHz ISM band. Theoretically, doing a differential operation would increase the output power of a single-ended case by a factor of two, while also improving the supply rejection ratio. The simulation analysis yielded a 60 W output power at a frequency of 433 MHz, accompanied by a high DC-to-RF conversion efficiency of 67%. This level of efficiency makes it well-suited for wireless power transfer applications. The use of this technology has the potential to speed up the construction of wireless power networks on a scale large enough to make it possible to charge electric automobiles using these systems.

C. Motor drives

The efficiency of the power electronic motor drive system of an EV is one of the most important factors determining the EV's overall performance. When doing an analysis of the system that drives the motor, it is essential to take into consideration both the inverter and the motor. In the context of electric transportation, the improvement in power density results in a number of beneficial outcomes. When compared to vehicles powered by ICE, EVs that have motor drives that are more efficient have a better chance of being less expensive to produce and having lower thermal requirements; as a result, the market for EVs is expected to grow. Figure 12[122] shows a block diagram of a motor drive system in an EV.

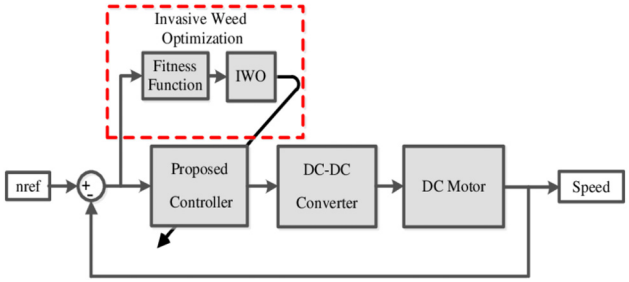

FIG. 12. Block diagram of motor drive system.[122] Obaid *et al.*, Indo. J. Electr. Eng. Comput. Sci. **15**, 95–103 (2019), licensed under a Creative Commons Attribution (CC BY) License.

21 October 2024 08:24:33

© Author(s) 2024

In the motor drive application of EVs, an inverter controls the frequency of power supplied to an AC motor. They are responsible for controlling speed and torque for electric motors. For DC–AC converters, single-phase inverters have been widely utilized as power converters in motor drive applications with lower voltage (below 1000 V) and smaller capacity (below 5 kW) due to their straightforward and robust control approach.[123,124] Xia *et al.*[125] introduced a single-phase inverter using a GaN foundation. This study investigates the improvement of the common ground dynamic DC-link (CGDL) inverter for single-phase applications. This is achieved through the use of GaN devices, split phase architecture, linked inductors, and a zero-voltage transition (ZVT) scheme. Figure 13(a) shows the proposed circuit diagram. The figure depicts the split phase CGDL inverter configuration, which includes an auxiliary ZVT branch in the front boost stage and a coupled inductor in the HB split phase inverter stage. Both stages operate simultaneously to achieve power decoupling and convert DC power to AC power. Thanks to the doubly grounded construction, which directly connects the negative terminal of the PV to the split phase grid neutral, the high-frequency common mode leakage current is effectively eliminated. The prototype of the CGDL inverter, with a power output of 1 kW and voltage of 200 V, showcases exceptional performance. The observed efficiency at UPF for various power levels is depicted in Fig. 13(b). This efficiency is based on the California Energy Commission (CEC) standard for photovoltaic inverters. Considering the controller and auxiliary power consumption, which includes the power for gate drivers, DSP controllers, and other integrated circuits, which is approximately 2.4 W, the weighted CEC efficiency is obtained to be 98.3% and a peak of 98.5% at a switching frequency of 75 kHz. This is without taking into consideration the additional power consumption. With a switching frequency of 75 kHz for the boost stage and 50 kHz for the split phase HB inverter stage, the equivalent efficiency figures are 98.5% CEC and 98.7% peak. The loss allocation figures obtained from both methods demonstrate a comparable distribution of losses for each component, as seen in Fig. 13(c). The last bar represents the projected power loss of 0.4 W attributed to the PCB traces, connectors, and capacitors. When compared to the experimental efficiency measurement of 13 W at the rated condition, the total loss obtained is 12.88 W, which is quite close. Valente *et al.*[126] examined the performance analysis of a single-phase GaN-based inverter. A novel GaN-based single-phase three-level Active NPC (3L-ANPC) inverter design has been developed, and its performance has been assessed in terms of thermal stress, efficiency, and total volume. The proposed 3L-ANPC inverter is composed of six switches, enabling the generation of three distinct voltage levels: positive (P), neutral (O), and negative (N). The modulation approach determines the current routes for each state. This work utilizes modulation, which incorporates two neutral states with distinct current pathways. The investigation demonstrated that the inverter had excellent performance, particularly in terms of switching loss. The inverter is equipped with a voltage of 400 V. The power output was 1 kW, and the switching frequency was 50 kHz. The inverter demonstrated exceptional efficiency, reaching almost 99%. At a power level of 1 kW, the efficiency is around 99%, but it decreases to about 95% when the output power reaches the rated level. The primary cause of this decrease in efficiency is conduction losses. Indeed, they possess dominance, and the costs incurred by switching are insignificant. It was discovered that the converter underwent testing in a DC/AC configuration, with a restricted DC-link voltage and output power, which is one of its limitations. The same approach has been taken by Gurpinar *et al.*[127] who introduced a single-phase inverter based on GaN HEMT technology. This paper presents an investigation of the trade-off between the volume of the heat sink and the output filter in a GaN HEMT-based single-phase Active Neutral point Clamped (ANPC) inverter. The inverter undergoes testing at 120 various operating points to assess its performance at four different heat sink temperatures (50, 60, 70, and 80 °C), five switching frequencies (16, 32, 64, 128, and 160 kHz), and six output load circumstances (300 W, 450 W, 850 W, 1250 W, 1650 W, and 2 kW). GaN HEMTs exhibit exceptional switching capabilities, resulting in extremely high efficiencies (exceeding 99%) while operating at low switching frequencies. The power cell's efficiency steadily decreases as the switching frequency increases, mostly owing to an increase in switching loss. However, even with this decrease, the efficiency remains over 97% throughout a wide range of loads at a frequency of 128 kHz. Increasing the switching frequency of the inverter by a factor of 4 (from 16 to 64 kHz) results in a power loss increase in just 1.5 times. By increasing the switching frequency to 128 kHz, which is eight times higher, the losses also rise by a factor of 2. The efficiency exhibits a linear decline as the switching frequency increases, dropping from 98.5% to 96.5% at a case temperature of 50 °C. The performance of the power cell is not significantly affected by changes in heat sink temperature under the specified test circumstances. They have used Eq. (17) to calculate their heat sink thermal resistance. Furthermore, the findings suggest that increasing the switching frequency can help maintain a high level of efficiency. They have used Eq. (18) to calculate their switching frequency. By increasing the switching frequency and heat sink temperature, the designer may decrease the size of the output filter and heat sink.

$$r_{hr} = \frac{T_h - T_a}{P_t}, \tag{17}$$

where rh_r is the heat sink resistance, T_h is the heat sink temperature, T_a is the room temperature, and P_t is the total power device loss.

$$f_{sw} = \frac{P_{Loss}}{K}, \tag{18}$$

where f_{sw} is the switching frequency, and P_{Loss} is the power loss.

Liu *et al.*[128] also proposed the use of a GaN-based single-phase inverter. In order to get a better analytical loss model for GaN HEMTs that takes nonlinear junction capacitance into account as well as an accurate analytical inductor loss model, a hybrid TCM control in the GaN-based single-phase megahertz inverter has been developed in this work. In addition, the research also conducted a comparison between the hybrid TCM inverter and the standard TCM inverter. This new design allows for both full range ZVS and limiting frequency variation. The inverter was equipped with an input voltage of 400 V and an output voltage of 200 V. The power output is 1 kW, and the switching frequencies were 300 kHz and 3 MHz. By utilizing this hybrid control system, the inverter is able to attain a power density of 120 W/in.^{3}, with a peak efficiency of up to 98%. The TCM efficiency is computed to provide a basis for comparison, taking into account its exceptionally high switching frequency of up to 10 MHz. It is evident that the efficiency of hybrid TCM consistently surpasses. The hybrid TCM has an efficiency that is approximately 4% more than that of the TCM,

21 October 2024 08:24:33

© Author(s) 2024

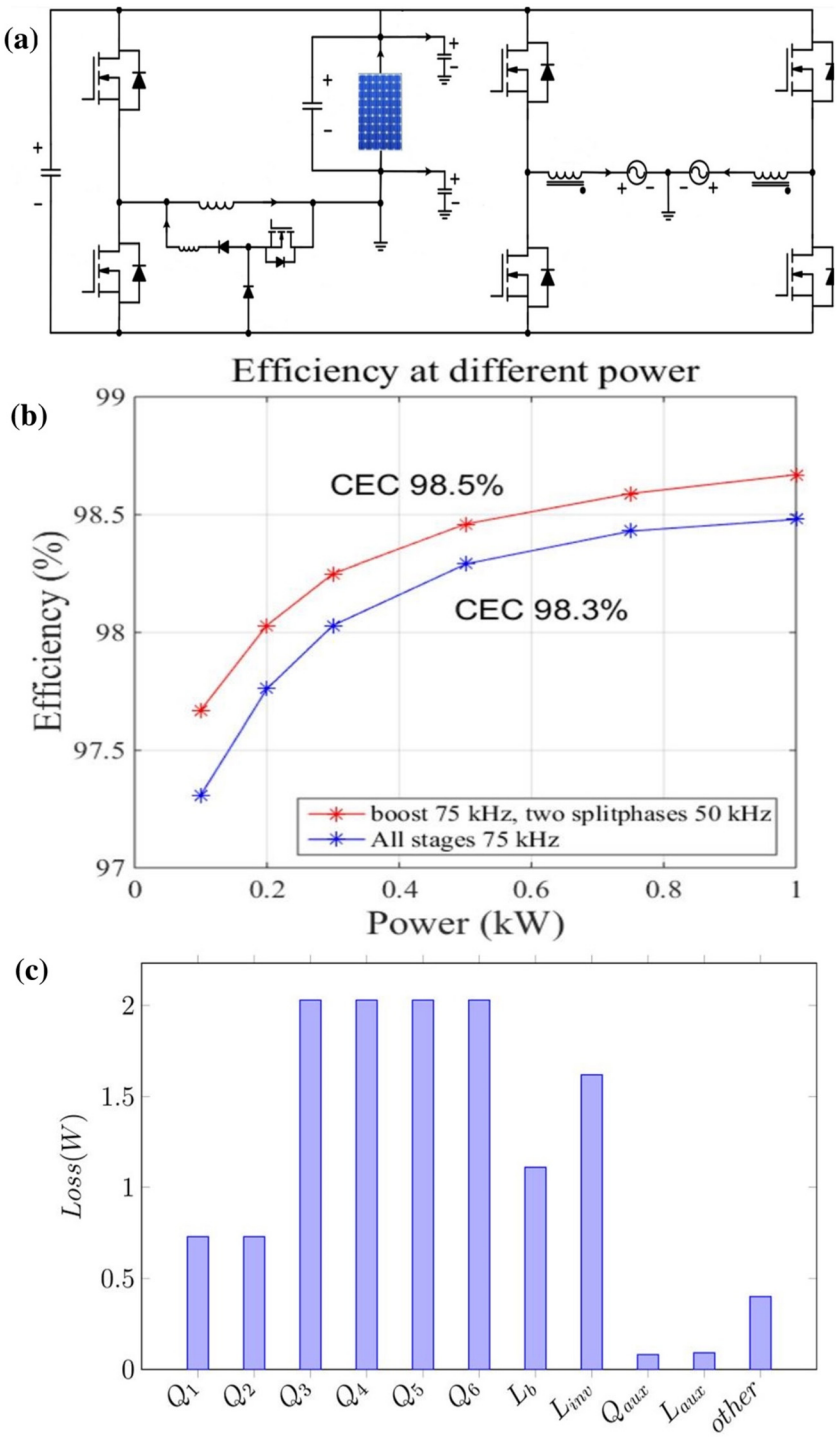

FIG. 13. (a) Proposed circuit configuration. (b) Efficiency of the inverter at different power. (c) Loss breakdown at a rated power of 1 kW for each component.[125] Reproduced with permission from Xia *et al.*, IET Power Electron. **13**, 525–534 (2020). Copyright 2020 Wiley-VCH.

21 October 2024 08:24:33

particularly when operating under light load situations. Table V presents the previous findings of different converters for motor drive.

While the mentioned single-phase inverters provide certain advantages, such as their straightforward design, they also have significant drawbacks. They exhibit reduced power production and less reliable voltage management. To address the limitations of single-phase inverters, particularly in motor drive applications for EVs, numerous researchers have suggested the use of three-phase multilevel

© Author(s) 2024

TABLE V. Data of different types of inverter's voltage, power, frequency, efficiency, and density based on recent studies.

Device type	Voltage (V)	Power (kW)	Frequency (kHz)	Efficiency (%)	Density (kW/l)	Ref.
GaN CGDL inverter	200	1	75/50	98.7	···	125
GaN 3L-ANPC	400	1	50	99	···	126
GaN single-phase inverter	···	2	16–160	98.5	···	127
GaN single-phase	400/200	1	300	98	8.3	128
GaN FCML inverter	200	2	···	99.43	···	129
GaN three-phase inverter	···	0.9	6	99.3	4.7	130
SiC inverter	550/400	···	20	99.3	···	131
PM Motor	···	5	···	90	···	132
PWM Inverter	400	2	100	80	···	133
PMSM Inverter	48	2	···	90	···	134

inverters due to their higher power output, improved efficiency, and enhanced durability. Elrais *et al.*[129] proposed GaN-based three port multilevel inverter. This study utilizes the appealing Flying Capacitor Multilevel (FCML) architecture to create a GaN-based three-port multilevel inverter, marking the first instance of its development. The three-port design utilizes a shared bus capacitor for the three ports and employs two four-level FCML DC–DC and DC–AC energy conversion routes. The DC–AC conversion method utilizes the widely established unfolding circuit mechanism to generate AC voltage. The suggested three-port multilevel converter employs two FCML converters utilizing GaN devices as power conversion routes. The proposed circuit has three ports and two pathways, with each path consisting of a four-level FCML converter. The DC–AC conversion method has a power rating of 1 kW and utilizes a full-bridge unfolding mechanism to generate an alternating current (AC) voltage. The DC–DC conversion channel is capable of processing a maximum power of 2 kW in both directions. There are two interfaces for each path. One interface of each path and port-1 are linked to the bus capacitor (*Cbus*), while the other interfaces of each path are connected to their respective ports. The voltage range for port-1 is 125 V_{DC} to 225 V_{DC}. The port-2 voltage range spans from 85 V_{RMS} to 120 V_{RMS} and is compatible with line frequencies of either 50 or 60 Hz. The port-3 voltage ranges from 0 to 200 V_{DC}. The voltage value of each port is selected according to the specific application requirements. Port-1 is the designated connection point for the photovoltaic (PV) system, and its voltage V_{DC} is equal to the voltage across the bus capacitor V_{bus}. The voltage of the AC grid at port-2 is 120 V_{RMS}. The battery has a voltage of 200 V_{DC} and may be attached to port 3. The proposed three-port inverter is designed to process a maximum power of 3 kW through a DC–AC line and a DC–DC path. The two pathways and the bus capacitor facilitate the transmission of electricity among the three ports. The three-port inverter is particularly dependable since its function remains unaffected even if one port source is not connected or fails, thanks to the decoupling of the three ports. The 3-kW prototype consists of a 1-kW DC–DC conversion path for AC production, which includes a full-bridge inverter. This inverter has reached a peak conversion efficiency of 98.2% at 500 W. Additionally, there is a 2-kW DC–DC conversion path that has achieved a peak efficiency of 99.43% at 990 W. The electricity is distributed across the three ports via the two conversion pathways. Ultimately, when the heatsink and microcontroller are taken out, the prototype achieves a power density of 285.6 W/in.^{3} (15.7 W/cm^3). In addition, multiple industries and companies have been engaged in the production of GaN-based motor drives, which have been utilized in various consumer products, including hoover cleaners, robotic cleaners, automation, and industrial machinery. EPC[135] and Navitas[136] are several of the prominent players in the semiconductor industry that manufacture a variety of motor drives based on GaN. Undoubtedly, numerous electric vehicle manufacturers have also utilized these motor drives in their EVs. GaN-based motor drives possess rapid switching speeds, allowing for accurate motor control. This enhances efficiency and responsiveness, resulting in a higher level of reliability compared to traditional motor drives. To summarize, the use of GaN-based multilevel inverters is strongly advised for motor drive applications. While single-phase inverters demonstrated superior efficiency, their power density was not substantial, which is crucial in terms of space. However, multilayer inverters have the capability to achieve high power density, resulting in a smaller inverter size. This makes them a feasible alternative for motor drive applications.

D. Auxiliary power system (APS)

The auxiliary power system (APS) of the EV transforms the high voltage from the battery pack into low voltage to provide electric power for internal components such as electric power steering, electric turbo, heated windscreen, and air conditioning. It can reduce air conditioning loss up to 30% and heating reduction up to 35%. DC–DC converters are utilized to supply power to these systems in EVs.[137,138] Many converters have a high current rating, which means they are not efficient.[92] This indicates that power is being wasted in different scenarios. Furthermore, numerous contemporary EVs utilize high voltage to operate certain supplementary equipment. Due to varying auxiliary power needs, it is not practical to use pre-made DC–DC converters for EVs, as these converters are typically built for high power applications.[139] This implies that car makers have two options: either they utilize preexisting high power converters at lower power levels, resulting in inefficiency, or they must develop their own converters. Using numerous GaN converters will improve efficiency and reduce power consumption while giving car manufacturers greater freedom to select the DC–DC converters' size and power.

Waradzyn *et al.*[140] developed a GaN-based DC–DC resonant boost converter. This work introduces an innovative approach to operating a resonant DC–DC switched-capacitor converter that achieves

21 October 2024 08:24:33

© Author(s) 2024

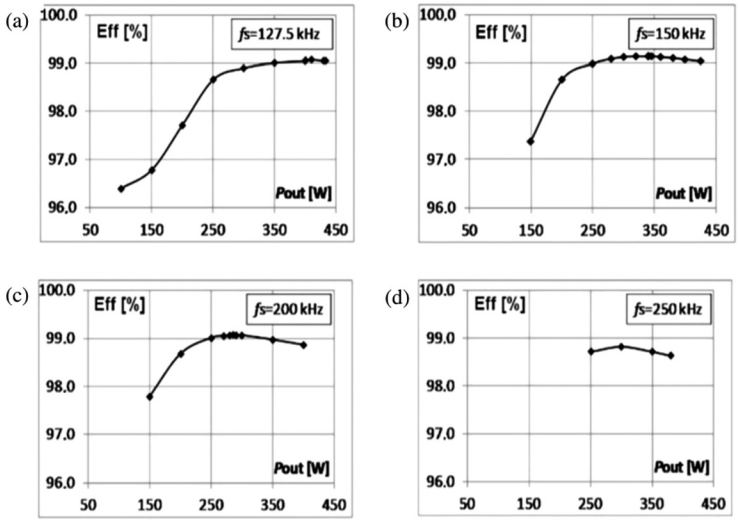

FIG. 14. Different efficiency for (a) 127.5 kHz, (b) 150 kHz, (c) 200 kHz, and (d) 250 kHz switching frequency.[140] Reproduced with permission from Waradzyn *et al.*, Energies **13**, 6403 (2020). Copyright 2020 MDPI.

very high efficiency and precise output voltage control. The suggested converter has attained a maximum efficiency of 99.228%. They have calculated their efficiency by using

$$\eta = 1 - \frac{\pi^2 P_{in} r T_s}{16 U_{in}^2 T_1} - \frac{\Delta U_D}{U_{in}} - \frac{\Delta W_{sn} f_s}{P_{in}}, \tag{19}$$

where U_{in} is the input voltage, P_{in} is the input power, r denotes the total resistance, and ΔU_D is the voltage drop across each diode, assumed to remain constant in the forward-conducting state. T_1 is the conduction time of the transistors, T_S is the switching period, f_S is the switching frequency, and ΔW_{SN} is the energy lost at turn-on in the resistances. Figures 14(a)–14(d) display the efficiency curve for various switching frequencies. Figure 14(a) displays the efficiency curve at a frequency of 127.5 kHz. The efficiency reached 96.3% when operating at a power of 100 W. Subsequently, it steadily rose to 96.8% when the power reached 150 W. The value steadily rises and reaches 98.8% when the power output is set at 250 W. Afterward, it attained a level of 99% with a power output of 350 W. It reached its maximum position at 99.2 with 415 W and remained constant until 435 W. Figure 14(b) displays the efficiency curve corresponding to a switching frequency of 150 kHz. The power output was 97.2% of the input power at 100 W. After that, it progressively rises to 99% when the power reaches 100 W. Later on, it attained its maximum value of 99.2% when the power reached 350 W. Subsequently, it gradually decreased to 99% when the power reached 425 W. The efficiency curve with a switching frequency of 200 kHz is depicted in Fig. 14(c). The power output of 100 W resulted in an efficiency of 97.8%. Following this, the efficiency progressively rises to 99% when the power output reaches 250 W. Subsequently, it reached its maximum point at 99.1% when the power output was 275 W. Afterward, the efficiency began to progressively diminish, reaching 99% when the power output reached 350 W. Finally, it decreases to 98% at 400 W. Figure 14(d) displays the efficiency curve with a switching frequency of 250 kHz. The power output was 98.8% efficient at a level of 250 W. At 300 W, it peaked at 98.9% and then continued to rise. At that point, it began to steadily decline to 98.8% when the power output reached 350 W. Finally, it decreases to 98.6% when the power is set at 380 W. Narasipuram *et al.*[141] proposed a GaN HEMT-based interleaved inductor–inductor–capacitor (iL^2C) resonant full-bridge DC–DC power converter. The two-stage interleaved L^2C enhanced load capacity, reduce current ripples, and circulating current. Consequently, they introduced a hybrid control strategy across all operating modes to improve regulation, minimize switching losses, and enable soft switching of the converter. Figure 15(a) illustrates a typical L^2C resonant FB DC–DC converter using the L^2C configuration. In order to provide adequate galvanic isolation, it is composed of a series resonant tank that is equipped with an inductor Lr and a capacitor Cr that are connected in series with a high-frequency transformer. Additionally, the resonant tank is equipped with a parallel inductance, which is referred to as the magnetizing inductance Lm. This inductance comes together to form the resonant network. The structure of the proposed iL^2C converter is illustrated in Fig. 15(b). The system comprises two resonant tanks, two switching circuits, and a solitary diode rectifier circuit. The two L^2C resonant-switching circuits (converters 1 and 2) are coupled in parallel on the primary part. The secondary part is equipped with a single rectifier network with double windings. The frequency of the converter is identified using

$$f_r = \frac{1}{2\pi\sqrt{L_r X C_r}}, \tag{20}$$

where L_r is the resonant inductor and C_r is the capacitor inductor. This approach enables operation at a phase shift angle of 180° between the gate signals of converters 1 and 2. The 3.3 kW GaN HEMT-based iL^2C resonant full-bridge DC–DC power converter with an input voltage of 300–500 V and an output voltage of 48 V was demonstrated. At full load conditions, the converter achieved an efficiency of 98.2%. Figure 15(c) shows the efficiency vs power curve. When the input and output voltages were 400 and 48 V, respectively, the efficiency was tested under eight different load circumstances, ranging from full load to light load. These load conditions were 3.3, 3.0, 2.5, 2.0, 1.65, 1.0, 0.5, and 0.33 kW, respectively. With a full load of 3.3 kW, half load of 1.65 kW, and light load of 0.33 kW, respectively, the measured efficiency was 98.2%, 98.7%, and 99.1%. An important advantage of employing the

21 October 2024 08:24:33

© Author(s) 2024

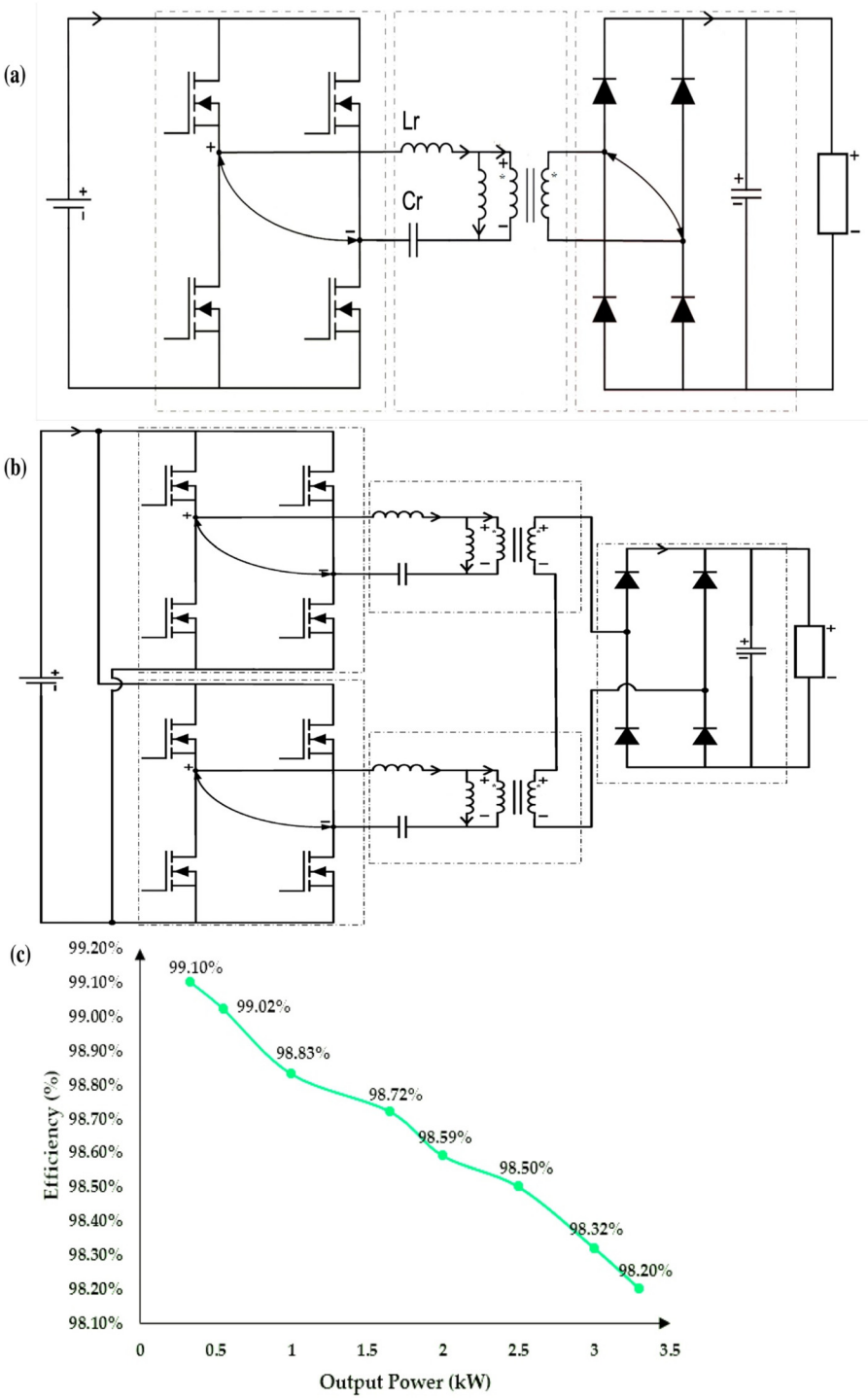

FIG. 15. (a) Typical structure of an L^2C resonant, (b) proposed iL^2C converter, and (c) efficiency vs power.[141] Reproduced with permission from Narasipuram *et al.*, Energies **16**, 5811 (2023). Copyright 2023 MDPI.

iL^2C converter instead of the L^2C converter is that the resonant tank design of the L^2C converter limits its ability to handle heavy loads, which leads to increased circulating current and reduced efficiency. By using iL^2C, the downside may be overcome by including two parallel L^2C, hence doubling the load capacity. Although both the studies aforementioned have good efficiency, the switching frequency was not disclosed. To address this, Kondrath *et al.*[142] offer a novel bidirectional full-bridge DC–DC converter for high power applications that

21 October 2024 08:24:33

© Author(s) 2024

combines SiC–GaN technology. The objective of this work is to utilize the high voltage capacity of SiC devices and the extraordinary switching performance of GaN devices in high-power converters. A 5-kW bidirectional full-bridge DC–DC converter has been built and simulated. The converter operates in continuous conduction mode (CCM). The converter's input voltage measured 540 V and operated at a switching frequency of 200 kHz, achieving an efficiency of up to 99.49%. The outcome is noteworthy due to the superior efficiency, switching behavior, and switch utilization achieved by the hybrid SiC–GaN-based converter. Nevertheless, as a result of the disparity in the switching characteristics of SiC and GaN devices and the inclusion of the transformer, the switch currents experienced significant surges during the switching transitions. This phenomenon may prevail at elevated switching frequencies and lead to reduced converter efficiency, particularly in high-power applications. In order to minimize the losses that occur during high switching frequencies, it is necessary to utilize soft switching approaches. Table VI displays a comparative analysis of the highest levels of efficiencies achieved by different converters, as given in recent research.

To achieve a more efficient converter, dual active bridge (DAB) converter is one of the popular choices because of its higher galvanic isolation, higher energy density, higher power ratings, and higher energy efficiency operation, which makes it a beneficial and most suitable converter in EV applications such as batteries and auxiliary power units. Jafari *et al.*[143] introduced a converter that utilizes GaN technology and features a DAB configuration. This converter is equipped with a high step-up capability and a high-frequency quasi-planar matrix transformer, which is capable of stepping up or stepping down voltage. It achieves zero-voltage switching (ZVS) by leveraging the resonance between its leakage inductance and the capacitance of the field-effect transistors (FETs). This enables the converter to operate efficiently at a high frequency of 300 kHz. High power density is made possible by the construction of the quasi-planar high-frequency transformer, which is sandwiched between the primary and secondary full-bridges. In their proposed converter, the transformer is positioned in the middle of the two full-bridge units. In a four-layer PCB design, the gate-drive and power-loops were implemented with the least parasitic inductance possible. The authors also provide electrical measurements and magnetic finite-element analysis (FEA) results, which are necessary for the design and evaluation of such a high-frequency transformer. The observed input voltage was 33 V, while the recorded output voltage was 400 V, with the converter operating at a switching frequency of 300 kHz. The converter had a commendable efficiency of 97.5% and a power density of 10 kW/l. Due to its superior power transfer capability, direct modulation, and high power density, which reduce the size of the converter, it is suitable for low voltage applications. GaN-based DAB converters are highly recommended for auxiliary power units in EVs because of their high power density, high efficiency, small size, and easy to realize ZVS. Although the full bridge converter has achieved significant efficiency, due to its expensive component cost and larger size, GaN-based DAB is a reasonable and viable solution.

IV. GaN-BASED DEVICES FOR NON-AUTOMOTIVE VEHICLES

In order to effectively transition toward a more electrified transportation system and mitigate the adverse consequences associated with the present transportation paradigm, it is imperative to extend the electrification efforts beyond automotive vehicles to encompass non-automotive modes of transportation as well. In this section, we delves into the applications of non-automotive devices in different transportation mediums.

A. Electric aircraft

In the field of aviation, it is vital that electric motors are meticulously engineered to ensure seamless operation under sustained conditions of rated power, particularly during cruise phases. In certain applications, such as hybrid cars, the electric motor is specifically engineered to function solely for brief power augmentation. Therefore, any comparisons involving these electric motors should be approached cautiously. The full potential of hybrid vehicles can be realized with the use of effective energy management strategies.[150,151] Figure 16(a)[152] illustrates the electric aircraft power system. In order to enhance the power density of electric motors, it is crucial to develop novel materials and technologies.[153,154] There exists a significant demand for aviation-specific electric motors that possess characteristics such as reduced weight, enhanced power output, and the ability to fulfill more stringent safety standards. The utilization of electric power in aircraft introduces novel challenges, such as the heat ejection dilemma, hence emphasizing the importance of improved electric motors.[155] Several studies imply that the advent of completely

TABLE VI. Comparison of voltage, power, frequency, density, and maximum efficiencies of different converters in recent studies.

Device type	Voltage (V)	Power (kW)	Frequency (kHz)	Efficiency (%)	Density (kW/l)	Ref.
GaN SCVD	200	0.4	127.5–250	99.228	···	140
GaN iL^2C	300–500	3.3	270	98.2	···	141
SiC-GaN	540	5	200	99.49	···	142
E-DAB GaN	400	0.2	300	97.5	10	143
Doubler GaN RSCC	300–500	1.5	160	99.82	65	144
GaN IBC	48/12	0.24	1200	96.7	···	145
RTBSCC MOSFET	150	0.14	160	98.3	···	146
MRCC SiC MOSFET	500/2000	5	285	98.5	···	147
SCRC MOSFET	300	3	350	99.5	···	148
RSCC MOSFET	120	100	100–200	94.6	···	149

21 October 2024 08:24:33

© Author(s) 2024

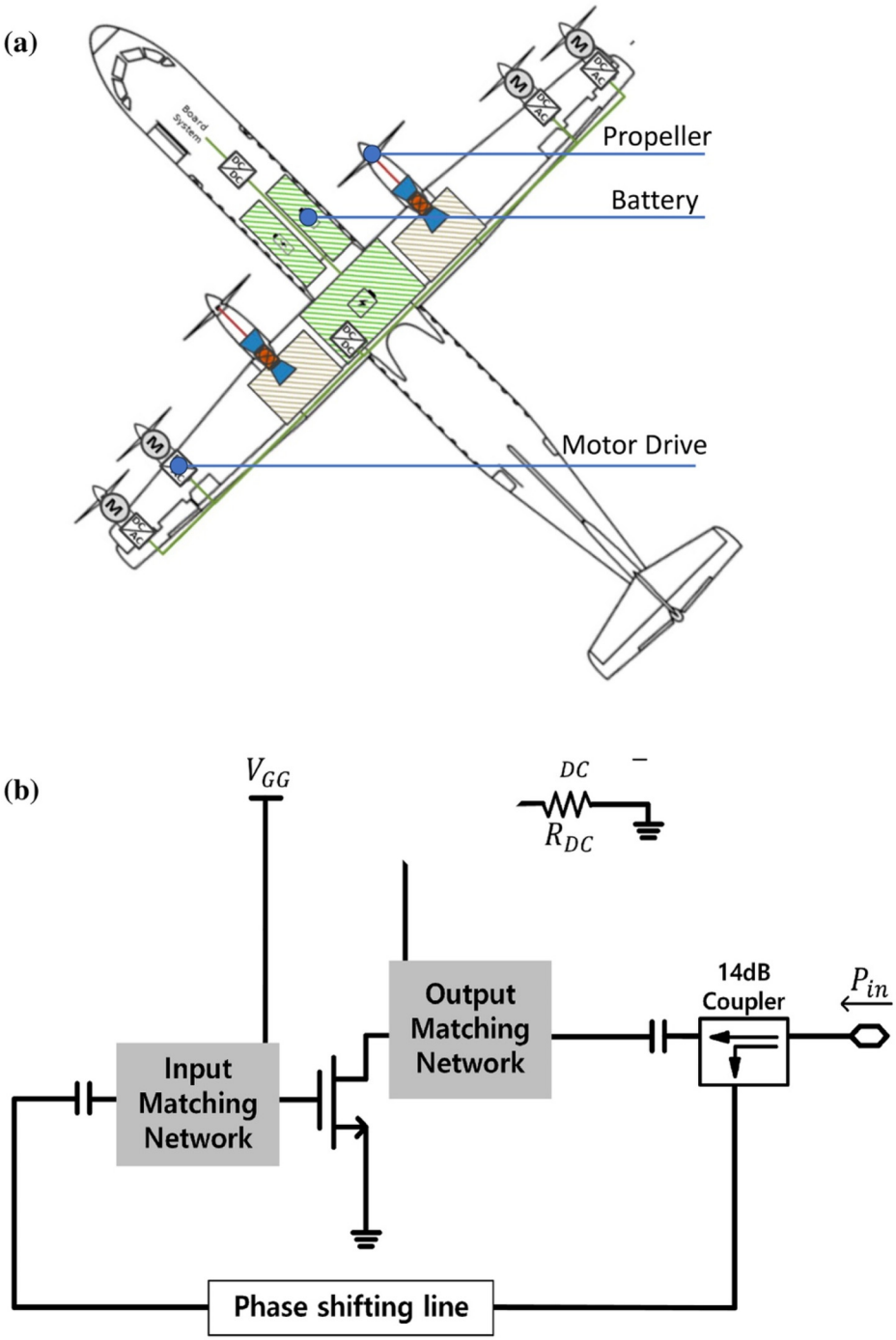

FIG. 16. (a) Electric power system of an electric aircraft.[152] Reproduced with permission from Hoelzen *et al.*, Energies **11**, 217 (2018). Copyright 2018 MDPI. (b) Schematic diagram of proposed class-F rectifier.[160] Reproduced with permission from Na *et al.*, Sensors **21**, 1608 (2021). Copyright 2021 MDPI.

electric aircraft in commercial aviation will necessitate the development of revolutionary aircraft designs.[156] An example of the NASA X-57 experimental aircraft[157] demonstrates the utilization of the distributed electric propulsion idea, which is deemed more appropriate for completely electric aircraft compared to traditional propulsion system configurations.

In the aircraft sector, the primacy of reliability tends to surpass that of cost. The utilization of GaN HEMTs results in a decrease in the dissipation of heat by power electronics, hence facilitating the development of cooling systems that are more compact and lightweight. The implementation of this approach enhances the dependability of the aircraft control system while concurrently mitigating its reliance on

21 October 2024 08:24:33

© Author(s) 2024

environmental control factors.[158] Moreover, the enhanced radiation tolerance of GaN and its capability to function well across a broad spectrum of temperatures render this WBG device highly suitable for deployment in the aforementioned applications.[159] The rectifier in aircraft health monitoring systems must provide high power capability despite its compact size. This feature enables the collection of appropriate sensing data and its transmission to the health monitoring system at a suitable pace. Rectifiers utilizing GaN device technology can be employed in wireless power transmission systems for monitoring the health of aircraft. Utilizing GaN devices instead of the usual Schottky diode in these systems enables high power operation. Na *et al.*[160] introduced GaN HEMT rectifier that has an independent second harmonic tuning circuit. This study presents a class-F synchronous rectifier design that utilizes a GaN HEMT with an integrated coupler and phase shifter on a module. The rectifier incorporates an independent second harmonic tuning circuit. A dedicated second harmonic tuning circuit was specifically constructed to enable class-F operation inside the 2.4 GHz frequency range. By independently adjusting the fundamental and second harmonic impedances of the circuits, it is possible to achieve high efficiency and output power for the power amplifier and rectifier. However, fine-tuning is necessary after implementation due to errors in the transistor's large-signal model and inaccuracies in the RF simulation of the passive circuits. Figure 16(b) depicts a diagram of the proposed synchronous rectifier. The drain DC supply for the power amplifier is transformed into a direct current load (RDC) for the rectifier. In theory, the RDC should equal the value of VDD divided by IDC for the power amplifier under big signal conditions. Nevertheless, in order to attain optimal performance, it is necessary to adjust the value of RDC owing to circuit losses and inaccuracies in the device model. A coupler and a phase shifter are positioned on the module in order to supply the RF signal to the gate. The coupling factor of the coupler is 14 dB, which should be about equivalent to the gain of the power amplifier. It is necessary to modify the phase of the RF signal in the gate in order to achieve optimal RF–DC conversion efficiency. This may be accomplished by utilizing a phase shifter, which is a transmission line on the module that alters the phase. The class-F power amplifier achieved a peak drain efficiency of 72.8%, while the synchronous rectifier achieved a peak RF–DC conversion efficiency of 69.6%. The transistor used in this setup had a very low power capacity yet it still managed to provide a high DC output power of approximately 7.8 W. The findings of the class-F power amplifier, including simulations and measurements, are shown in Fig. 17(a). Following the deployment of the power amplifier, more optimization was performed by adjusting the fundamental and second harmonic impedances in a manner apart from one another. At a maximal output power of 40 dBm, the manufactured power amplifier has a drain efficiency of 72.8% and a gain of 11 dB, according to the measurements taken. There is a high degree of concordance between the simulated and measured results. In Fig. 17(b), it is shown that the optimal load resistance is around 100 Ω. At this resistance, an RF–DC conversion efficiency of 69.6% and an output DC power of 7.81 W were effectively achieved. When the loss of the coupler and the phase

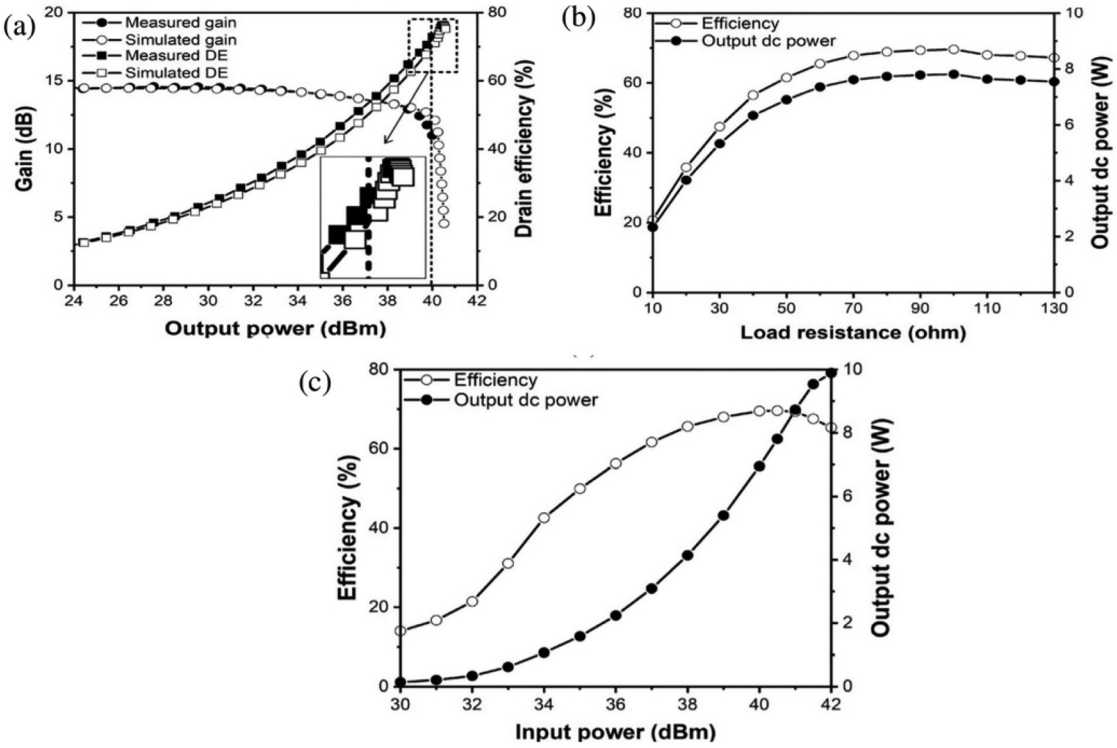

FIG. 17. (a) Simulated and measured gain and drain efficiency of the class-F power amplifier. (b) Measured RF-dc conversion efficiency and output DC power of the synchronous rectifier. (c) Measured power efficiency and output DC power according to the input power.[160] Reproduced with permission from Na *et al.*, Sensors **21**, 1608 (2021). Copyright 2021 MDPI.

21 October 2024 08:24:33

© Author(s) 2024

shifting lines that are connected to the rectifier are taken into consideration, it is recommended that a greater amount of the RF input power of the rectifier be given than the RF output power coming from the class-F power amplifier. It was possible to attain an RF-dc conversion efficiency of 69.6% with an input power of 11.22 W (40.5 dBm). A maximum of 9.89 W of direct current was achieved with an efficiency of 65.3%, and the RF–DC conversion efficiency was maintained at a level that was more than 50% at input power levels of at least 35 dBm. Similarly, Hoque *et al.*[161] proposed a GaN-based F-class rectifier. This study introduces a novel dual-band harmonic-tuned synchronous rectifier. It utilizes a GaN HEMT device with an inbuilt coupler and phase-shifter to handle RF input power at the watt level. The suggested design introduces a compact load network that achieves both inverse class-F and class-F load characteristics at 1.17 and 2.4 GHz, respectively. The 10-W rectifier circuit exhibits 78% and 76% efficiencies at 1.17 and 2.4 GHz frequency bands, respectively. Even with an input power of 32 dBm (∼1.5 W), the efficiency stays consistently over 50%, indicating strong efficiency in the lower input power range. The highest efficiency for the low band is 78% when the input power is 38.2 dBm. The DC power at this magnitude is 5.1 W. This study also showed that the input power range is greater in the 1.17 GHz operation compared to the 2.4 GHz operation. This is because the rectifier operates in class-F mode at 2.4 GHz, whereas it operates in inverted class-F mode at 1.17 GHz. By operating in this mode, the circuit's input power range is expanded, guaranteeing a minimum efficiency of 50% for an input power of 25 dBm. This characteristic makes the circuit highly appealing for future high power dual-band RF–DC applications. Table VII shows the previous development of different rectifiers.

Both of the aforementioned rectifiers have better designs, but the efficiencies of both devices are not significant due to high noise and high switching loss. To address this efficiency issue, a high-efficiency GaN-based bridgeless rectifier was fabricated and designed by Liu *et al.*[162] This work demonstrates the successful implementation of full-range ZVS for the bridgeless GaN-based MHz dual-SEPIC power PFC circuit. An investigation is conducted on the operational concept of the topology and the ZVS control. The integrated inductors are meant to consolidate all the magnetic components into a single E-I-E magnetic core. An analysis has been conducted on the inductance design for the bridgeless SEPIC PFC and the magnetic modeling for the E-I-E core with the linked inductor. The 300-W rectifier, which includes integrated inductors, achieved a peak efficiency of 97%. The rectifier had an input voltage of 220 V and an output voltage of 100 V. The rectifier also attained a notable switching frequency ranging from 400 to 1000 kHz. Therefore, employing a bridgeless SEPIC PFC circuit enables achieving a higher switching frequency, resulting in a reduced size of the rectifier. In the simplest terms, the rectifier is an extremely vital component for monitoring the health of the aircraft. In aviation, class F rectifiers are utilized rather often. It is still used despite the fact that its efficiency is not substantial due to the fact that the input impedance of the rectifier circuit is impacted by the load value. As a result, as the load value grows, the output voltage increases, but the efficiency declines. Despite this, it is still used because of its inexpensive cost and compact design.

B. Heavy duty and off-road vehicles

For the electrification of heavy-duty and off-road vehicles, such as trucks, improvements in power electronic systems are required. Electrification in transportation began with cars and has since extended to other modes, such as buses and trains. It is possible that power systems will leverage the enhanced capabilities of wide bandgap (WBG) devices in combination with silicon (Si) transistors to meet future vehicle requirements. GaN devices, in particular, have the potential to contribute to the development of more reliable and efficient heavy-duty vehicles.[36] One of the main components is the DC converter. These converters are used in electric vehicles (EVs), especially heavy-duty EVs, to prevent ripple currents from returning to the power source and to smooth out fluctuations in DC bus voltage. By utilizing converters, the impact of inductance in EV applications can be reduced. Converters are employed in inverters, motor controllers, and battery systems. Additionally, they function as filters to protect EV subsystems from voltage spikes, surges, and electromagnetic interference (EMI). GaN HEMT gate driver-based converters offer potential benefits due to their higher electric field, enhanced thermal management, and improved power conversion efficiency. An integrated dual half-bridge topology soft-switched high step-up DC/DC converter was suggested by Moradisizkoohi *et al.*[168] The converter achieves significant voltage amplification through the sequential coupling of secondary windings of transformers. Furthermore, an output stage utilizes a voltage multiplier stage (VMS) to enhance the voltage gain and equally distribute the voltage stress across the semiconductors. Moreover, the VMS directly feeds the output capacitors with the transformer leakage

TABLE VII. Comparison of different kinds of GaN-based amplifier's parameters from recent literature.

Device type	Circuit type	Power (W)	Frequency (GHz)	Efficiency (%)	Phase shifter	Ref.
GaN HEMT	Class F	7.8	2.4	69.6	External	160
GaN HEMT	Class F	10	2.4	78	···	161
GaN	SEPIC PFC	3000	0.0004	97	···	162
GaN HEMT	Class F	8.7	0.985	78	External	163
GaN HEMT	Class-F^{-1}	8	1.15	80.1	External	164
GaN HEMT	Class-F^{-1}	6.9	1.8	77	External	165
GaN HEMT	Class-F^{-1}	5.1	1.17	78	Integrated on module	161
GaN HEMT	Class F	7.18	2.4	75.5	Integrated on module	161
GaN	Class E	10	0.01	90	···	166
GaN	Class E	10	0.02	81.5	···	167

21 October 2024 08:24:33

© Author(s) 2024

energy. The active-clamp circuit in the proposed converter serves two purposes: it limits the voltage stress on switches and enables soft-switching, resulting in improved efficiency. The suggested converter is shown in Fig. 18(a). It comprises of a balanced VMS to raise the voltage conversion ratio and a traditional boost converter with an active-clamp circuit to give an input current with low ripple and soft-switching performance. The proposed converter's equivalent circuit is shown in Fig. 18(b). In this circuit, V_{in} represents the photovoltaic (PV) source, V_o represents the output voltage, L_B represents the boost inductor, C_r represents the DC-blocking capacitor, $C_{o1} - C_{04}$ represent the output capacitors, C_{m1} and C_{m2} represent the switched capacitor, S_M and S_C represent the main and clamp switch, respectively, $D_{o1} - D_{o4}$ represent the output diodes, and R_o represents the load resistance. The transformers are modeled using a magnetizing inductor (L_m), a leaking inductor (L_k), and an ideal transformer with a turn's ratio of $n = N_2/N_1$. Figure 18(b) also illustrates the presence of two transformers, T_1 and T_2. In this context, L_{k1} and L_{m1} represent the leakage inductor and magnetizing inductor of transformer T_1, respectively. Similarly, L_{k2} and L_{m2} designate the leakage inductor and magnetizing inductor of transformer T_2. The laboratory prototype of the suggested converter, which had a power output of 1 kW and operated at a voltage of 400 V, reached a maximum efficiency of 97.1% when it was operated at a switching frequency of 100 kHz. Figure 18(c) displays the plotted curve representing the observed and computed efficiency. According to the diagram, the efficiency was 95.5% when the power was 100 W. Subsequently, it exhibited a gradual rise, reaching a level of 96.4% when the power output reached 200 W. Afterward, it further rises to 96.6% when the power reaches 300 W. The efficiency thereafter rises to 96.8% when the power reaches 400 W. Following that, it increases to 97% when the power reaches 500 W. After that, the efficiency achieved its maximum value of 97.1% with a power output of 600 W. Later on, the efficiency began to decline to 96.5% when the power reached 700 W. The value further decreases to 96.6% when the power reaches 800 W. Subsequently, the efficiency soared to 96.5%

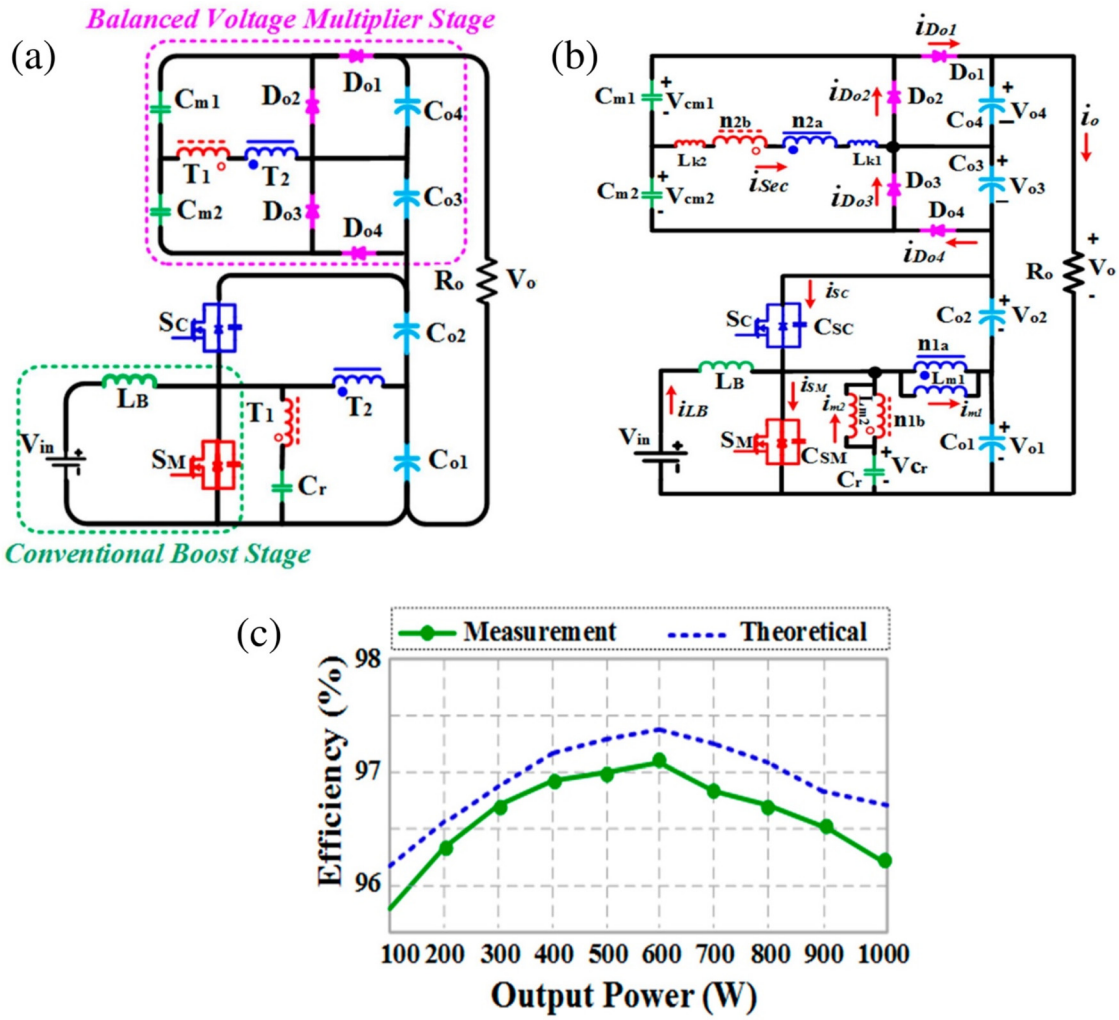

FIG. 18. The schematic of the proposed converter: (a) proposed converter and (b) the equivalent circuit. (c) Calculated and measured efficiency vs output power.[168] Reproduced with permission from Moradisizkoohi *et al.*, Inventions **3**, 63 (2018). Copyright 2018 MDPI.

21 October 2024 08:24:33

© Author(s) 2024

when the power output reached 900 W. Eventually, the efficiency declined and stabilized at 96.2% when the power reached 1000 W. It is worth mentioning that the highest efficiency achieved via theoretical calculations at an output power of 600 W is 97.3%. Similarly, Nagao *et al.*[169] introduced a three-level gate driver for GaN HEMTs in half-bridge converters. In comparison to the traditional two-level approach, the suggested gate driver achieved a 23% reduction in reverse conduction loss in a half-bridge evaluation circuit. The SR buck converter operates with a 48 V input, producing a 12 V output with a power of 48 W, and has a switching frequency of 500 kHz. The suggested gate driver enhances efficiency by 1.6% compared to the two-level technique, which achieves an efficiency of 95.5% at 500 kHz and 90.7% at 1 MHz. In a related study, Takahashi *et al.*[170] suggested a gate driver for GaN HEMT-based capacitors that operates with only one voltage supply. The suggested gate driver effectively reduces incorrect activation and minimizes the reverse conduction loss using a sole voltage source. The suggested and traditional gate drivers are utilized in a 48- to 12-V synchronous buck converter. The proposed and conventional gate drivers have efficiencies of 93.6% and 86.7%, respectively, operating at a frequency of 500 kHz with power output of 24 W. The peak of the ringing caused by turning on the high-side switch is 0.45 V when using the suggested gate driver at 48 W.

Although the aforementioned gate driver converters showed good parasitic inductance, switching efficiency is one of the main drawbacks of these kinds of converters. Monolithic integration with the gate driver of the chip can suppress this drawback. Hsia *et al.*[171] introduced an innovative monolithically integrated half-bridge driver design utilizing GaN-on-Si technology for high-speed and high-voltage DC–DC converters. Currently, there is a lack of cost-effective integrated high-side drivers for DC–DC converter applications in the GaN-on-Si technology. This study suggests using an E-stacked E/D-mode (EED) inverter-based high-side driver to directly drive GaN power transistors on the GaN-on-Si technology. The purpose is to effectively operate E-mode GaN transistors as output stages of power converters. The EED structure enhances the D/E-mode inverter to provide a high-efficiency and low-EMI high-side gate driver for E-mode power transistors, instead of depending just on a traditional level shifter and bootstrap circuit design. In this work, they have used synchronous buck architecture in the circuit. Figure 19(a) depicts the proposed integrated buck converter design utilizing high-voltage GaN technology. It primarily comprises three components: the power switch, gate driver, and buffer stage. The experimental findings demonstrate the circuit's ability to efficiently operate the half-bridge circuit and its suitability for use in a buck converter. The converter, operating at a voltage of 200 V, was able to provide an output power of 20 W with a peak efficiency of up to 90.7%. Figure 19(b) displays the efficiency of the buck converter technology. The graphic illustrates that the efficiency reaches 84% when the power output is 2.5 W. Subsequently, it rose to 88% at 5 W. The efficiency further improves to 90.1% when the power reaches 8 W. The efficiency thereafter achieved its maximum value of 90.7% with a power output of 10.8 W. Afterward, the efficiency saw a decline to 90.1% when the power output reached 16 W. Following that, the efficiency declined to 89% when the power output reached 21 W. The high-voltage switching signals, operating at a peak voltage of 200 V, have risen and fall periods of 54.4 and 57.6 ns, respectively. This implies that they achieve great speed in switching. Figure 19(c) displays a pie chart illustrating the estimated

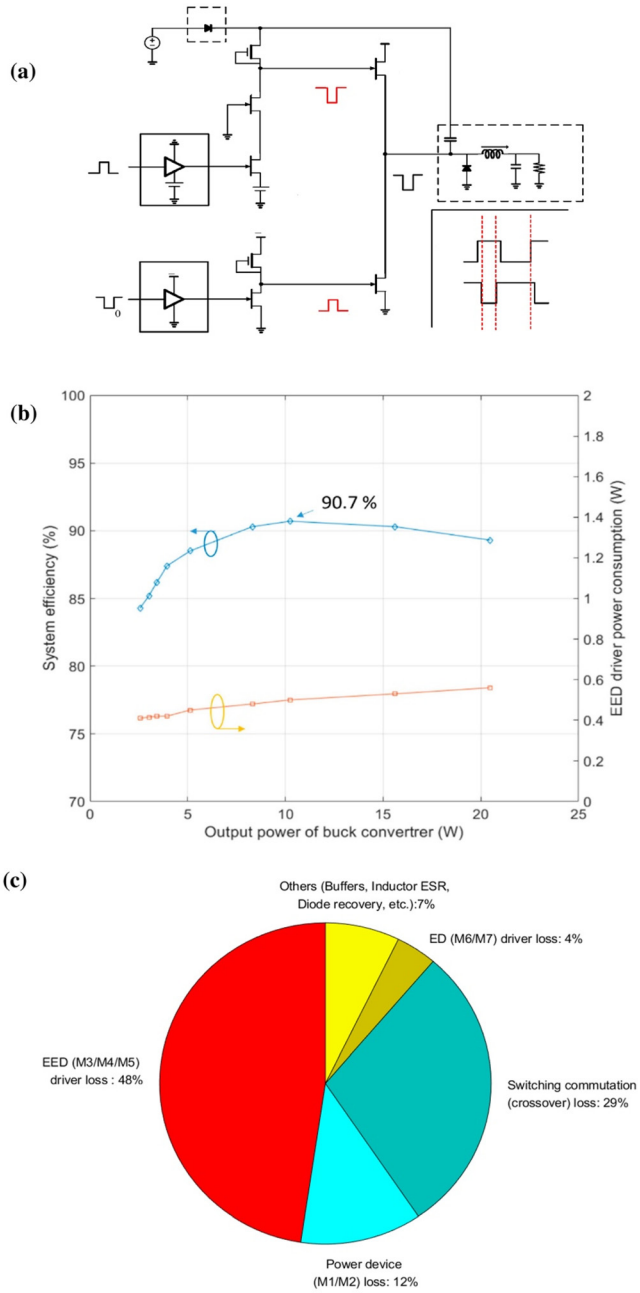

FIG. 19. (a) Proposed integrated buck converter. (b) The efficiency curve of the buck converter technology. (c) Overall power loss percentage comparison of an GaN-based buck converter.[171] Reproduced with permission from Hsia *et al.*, Appl. Sci. **12**, 5109 (2022). Copyright 2022 MDPI.

percentage of power loss for each device in the converter operating at 90.7% efficiency. The chart reveals that there was a 12% power loss in the device, 29% loss in switching commutation, 4% loss in ED driver, 48% loss in EED driver, and 7% loss in buffers, inductor ESR, diode recovery, and other factors. Table VIII shows previous findings of different GaN-based gate drivers.

21 October 2024 08:24:33

© Author(s) 2024

TABLE VIII. Different findings of GaN-based gate drivers based on recent literature.

Device type	Voltage (V)	Power (kW)	Frequency (kHz)	Efficiency (%)	Density (kW/l)	Ref.
GaN	400	1	100	97.1	···	168
GaN HEMT	48/12	0.0528	500	95.5	···	169
GaN HEMT	48/12	0.048	500	93.6	···	170
GaN on Si	200	0.0205	1000	90.7	···	171
GaN	100	3.1	1440	98.41	···	172
GaN HEMT	400	0.015	262	95.6	···	173
GaN HEMT	···	0.024	1000–2000	89.8	···	174
GaN SiC	28	0.030	10 000	95	···	175
GaN	400	···	300/700	93.1	1000	176
GaN	1000	6	3	98.6	150	177

While GaN converters with gate drivers have achieved good efficiency, converters that are monolithically integrated with gate drivers have achieved fast switching speed, reduced size, and good efficiency. This integrated solution is only feasible for use in heavy-duty vehicles to power their electronic systems.

C. Electric rail vehicle

The electrification of trains has been initiated as part of the ongoing shift toward more sustainable alternatives. In order to maintain competitiveness against alternative modes of transportation, such as personal vehicles and airplanes, railway traction systems must enhance their auxiliary power output while concurrently minimizing the weight and volume of their electronic components. This optimization is crucial to maximizing passenger capacity within the limited space available. The act of decreasing weight also leads to a decrease in the rate of wheel deterioration, as well as a reduction in overall energy usage. Furthermore, it is vital for these modes of transportation to function with enhanced efficiency, elevated speeds, and improved reliability in their railway traction systems.[178] In the forthcoming era, the production of exclusively electric heavy rail systems will be undertaken. The primary obstacle confronting this particular rail system pertains to its exorbitant financial implications. By incorporating WBG devices into auxiliary converters, it becomes possible to achieve a higher power density in the traction equipment, leading to cost and energy savings.[179,180] The use of GaN-based devices in onboard power converters, such as onboard chargers, in high-speed trains can increase efficiency. Modern trains and light-rail systems are not complete without on-board battery chargers, which guarantee the backup power needed for critical operational and safety systems. Figure 20(a)[181] shows the block diagram of on board chargers in an electric power train.

A 7.5-kW DAB converter has been implemented by Alemanno *et al.*,[182] which operates at a switching frequency of 200 kHz and utilizes 650 V commercial GaN HEMT transistors. This converter is specifically designed for charging applications. Figure 20(b) illustrates the architecture of the prototype converter. From Fig. 21, it is clear that there are three components that make up the system: the mother board, control board, and GaN module. The motherboard had a $265 \times 223\,\mathrm{mm}^2$ FR4 PCB with a thickness of 2 mm and was equipped with four layers of 2 ounce copper to effectively handle the high current levels in the power section. Furthermore, a generous exposed copper area was strategically placed on both the top and bottom layers of the transformer, with thermal vias connecting them. This design choice was made to enhance the thermal conductivity of the transformer. The low voltage part was equipped with sensors and conditioning circuits for analog signals, as well as PWM signal lines. The power and low-voltage sectors' reference grounds were isolated using a commercial DC/DC converter model AE40-EW-S12 by CUI. This converter served as an auxiliary power supply, capable of delivering a maximum output of 12 V and 3.3 A. The auxiliary supply for this application was far larger than necessary and was mostly chosen due to its easy accessibility. The dimensions of this functional block may be greatly decreased by a customized design. The layout design adhered to the IEC 61010-1 and IEC 60335-2-29 standards by implementing a clearance distance of 1.6 mm and a creepage distance of 4.5 mm. The control board was a four-layer FR4 board with dimensions of $46.2 \times 38.1\,\mathrm{mm}^2$, particularly engineered to execute the control law of the converter. The board detected signals from the motherboard and produced PWM signals. The controller is a specialized solution designed for power supplies that possess a digital environment, allowing it to efficiently handle a high-speed hardware state machine. This resulted in a smaller number of versatile microcontrollers compared to the standard C2000 family, with the benefit of reduced energy consumption. By implementing this approach, it becomes possible to effectively manage many feedback loops by dividing them into separate fast pathways, hence enabling a more efficient and responsive use of greater bandwidth. A notable capability is the ability to produce four pairs of PWM signals with a greater temporal resolution of 250 ps, which are synchronized using an inbuilt phase-shift mechanism. The GaN daughter module is comprised of two distinct boards, namely, a driver board and an IMS board. This technique was created to meet the requirement for improved thermal control while minimizing parasitic effects. The prototype achieved excellent efficiency, with a peak efficiency of over 98%. They have also studied the thermal management of the converter. Figures 21(a) and 21(b) show the thermal image of the prototype. Examining the magnification of the principal side FB in the lower portion of the diagram, one can observe an increased thermal stress in the first leg as compared to the second leg. Based on the small temperature imbalance, it was feasible to detect a problem in the

21 October 2024 08:24:33

© Author(s) 2024

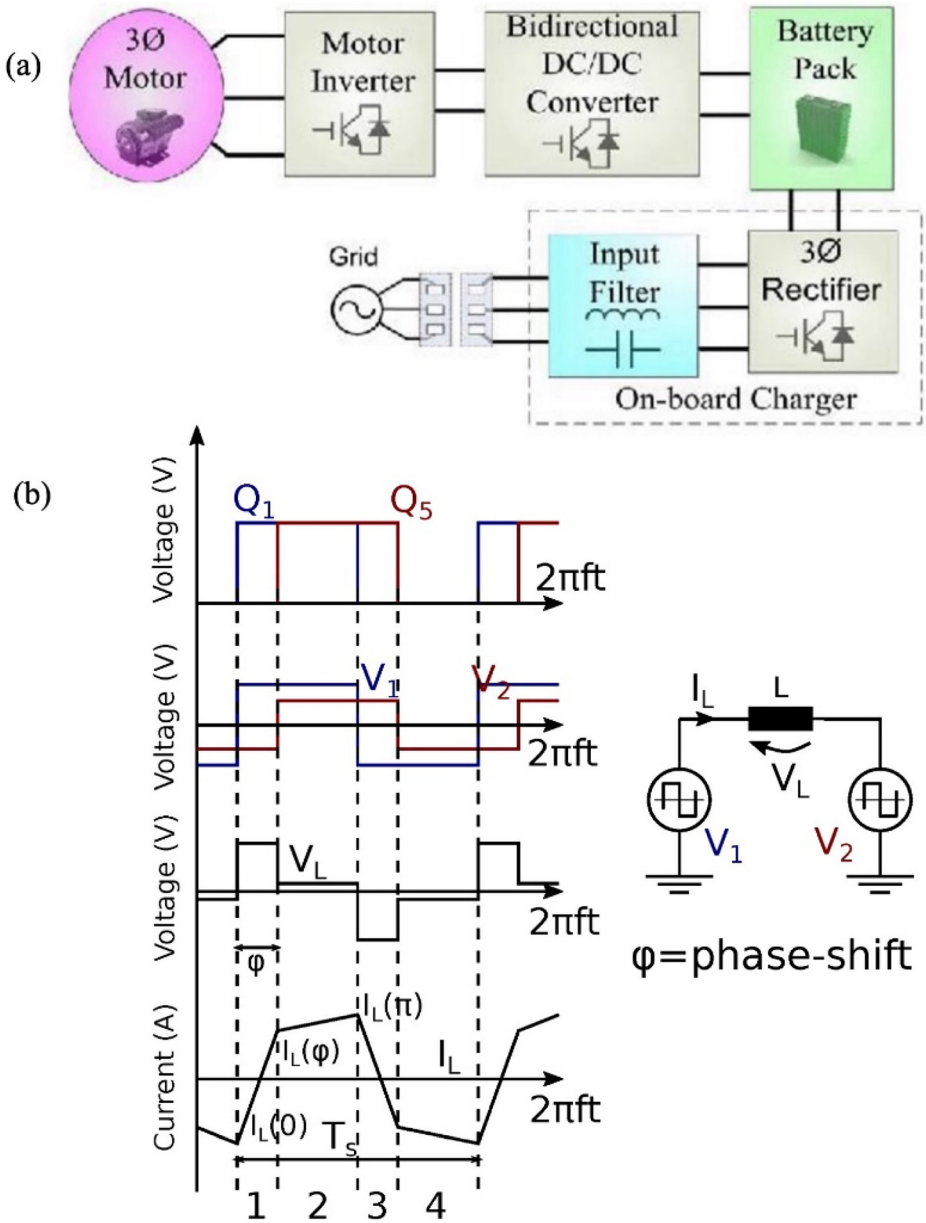

FIG. 20. (a) Block diagram of OBC in an electric train.[181] Reproduced with permission from Dusmez *et al.* APEC **2**, 2121–2127 (2012). Copyright 2012 IEEE. (b) Architecture of the bidirectional DAB prototype.[182] Reproduced with permission from Alemanno *et al.*, Electronics **12**, 1280 (2023). Copyright 2023 MDPI.

arrangement of the ground loop in this specific section of the motherboard, resulting in an increased stray inductance. Similarly, Karakaya *et al.*[183] proposed a bidirectional GaN HEMT-based converter. In this study, a 5.4-kW bi-directional DC/DC converter with QSW ZVS is shown. The converter utilizes GaN-based half-bridge prototypes and incorporates short circuit protection capability. The converter employs two half-bridges to eliminate the fluctuation in inductor current, thereby decreasing both the ripple in output voltage and the losses caused by the equivalent series resistance (ESR) of the capacitor. The suggested bidirectional converter operates at a capacity of 5.4 kW, achieving a volumetric power density of 5.24 kW/l or 85.9 W/in.^{3} when using air-forced cooling. It demonstrates exceptional efficiency in both buck and boost modes. Figure 21(c) displays the efficiency curves of the converter operating in buck mode and boost mode, using an input voltage of 400 V and a switching frequency of 450 kHz. The efficiency in buck mode was 93.8% at a power output of 1000 W, as shown in the figure. Subsequently, it steadily rose to 96% when the power reached 2000 W. The value steadily rises to 97% when the power reaches 3000 W. Afterward, the efficiency experienced a marginal rise to 97.2% when the power output reached 4000 W. It remained unchanged until it hit 5000 W. Following that, it experiences a minor decline to 97.0% when the power output reaches 5500 W. The efficiency of the boost mode was 94% when operating at a power of 1000 watts. Later on, it steadily rises to 96% when the power reaches

21 October 2024 08:24:33

© Author(s) 2024

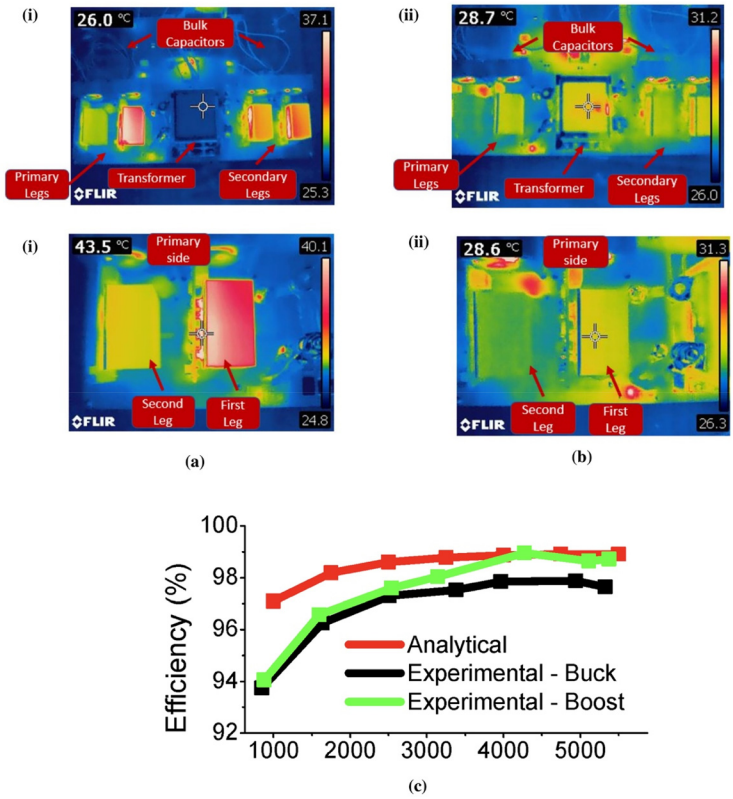

FIG. 21. Thermal image of the prototype at (a-i) phase shift at 35 °C for primary legs, (a-ii) phase shift at 35 °C for primary legs, (b-i) phase shift at 30 °C for primary legs, and (b-ii) phase shift at 30 °C for primary legs.[182] Reproduced with permission from Alemanno *et al.*, Electronics **12**, 1280 (2023). Copyright 2023 MDPI. (c) Efficiency curve of Buck and Boost mode.[183] Reproduced with permission from Karakaya *et al.*, Energies **14**, 2867 (2021). Copyright 2021 MDPI.

2000 W. Later on, it continues to rise steadily, reaching a peak of 97.3% when the power output reaches 3000 W. The value reached its maximum point at 98.5% when the power was 4000 W. At this point, it had a marginal decline to 98% when the power output reached 5000 W. Finally, it experienced a modest rise to 98.2% when the power reached 5500 W. The diagram also displayed the analytical efficiency curve of the converter. Analytical efficiency surpasses experimental findings somewhat, mostly due to unaccounted loss causes and measurement errors in the experimental data. The primary cause of loss in GaN HEMTs is conduction loss, which is attributed to the large current ripple. This underscores the need for device paralleling. Furthermore, the inductor's one-layer design, using Litz wires, effectively minimizes AC losses experienced by the inductor. Table IX presents recent findings on various converters for use in electrifying trains.

The bidirectional DAB converter yielded satisfactory outcomes; nonetheless, both investigations identified thermal management issues, including the presence of elevated stray or parasitic inductance in their PCB designs. Yang *et al.*[186] have addressed this issue by developing a lattice loop topology to mitigate parasitic inductance in a GaN

TABLE IX. Comparison of different GaN converter's data for electric rail system on the basis of recent studies.

Device type	Voltage (V)	Power (kW)	Power density (kW/l)	Frequency (kHz)	Efficiency (%)	Ref.
GaN HEMT	500	7.5	···	200	98.2	182
GaN HEMT	400	5.4	5.24	450	98.5	183
GaN HEMT	650	3.7	2.03	292	96.32	184
GaN E HEMT parallel gate driver	650	7.2	3.3	···	98	185
GaN HEMT	50	0.125	···	600	95.6	186
GaN	400	3.3	···	144–175	96.32	187
GaN	14	6.6	10.5	···	···	188
GaN	650	7.2	2.5	0.12	97	189
GaN CLCC	···	6.6	2.64	500	96	190

21 October 2024 08:24:33

© Author(s) 2024

HEMT-based converter. In order to mitigate the effects of parasitic inductance, the authors suggest implementing a vertical lattice loop structure with several loops. This approach is applicable to GaN HEMT packages of any form or shape. The single loop serves as the benchmark loop for designing the vertical lattice loop structure. Moreover, the suggested framework is constructed by arranging the reference loop in layers. The recommended vertical lattice loop construction effectively reduces both power loop inductance and gate loop inductance. In order to confirm the decrease in parasitic inductance, a 125-W buck converter design is implemented. The design includes an input voltage of 50 V, input current of 2.5 A, output voltage of 25 V, and output current of 5 A. The design is based on the PCB seen in Figs. 22(a) and 22(b). Figure 22(c) depicts the efficiency curve of the buck converter, both with and without a vertical lattice loop construction. When the vertical lattice loop is applied at a frequency of 1 MHz, the efficiency increases by roughly 1.2% compared to when it is not applied. The reduction in parasitic inductance leads to a decrease in switching loss. The experimental findings confirm the effectiveness of the suggested vertical lattice loop construction in enhancing efficiency and enabling high-frequency operation. Moreover, it has been confirmed that the suggested configuration exhibits superior efficiency when the GaN HEMTs are operated at high frequencies and under low loads.

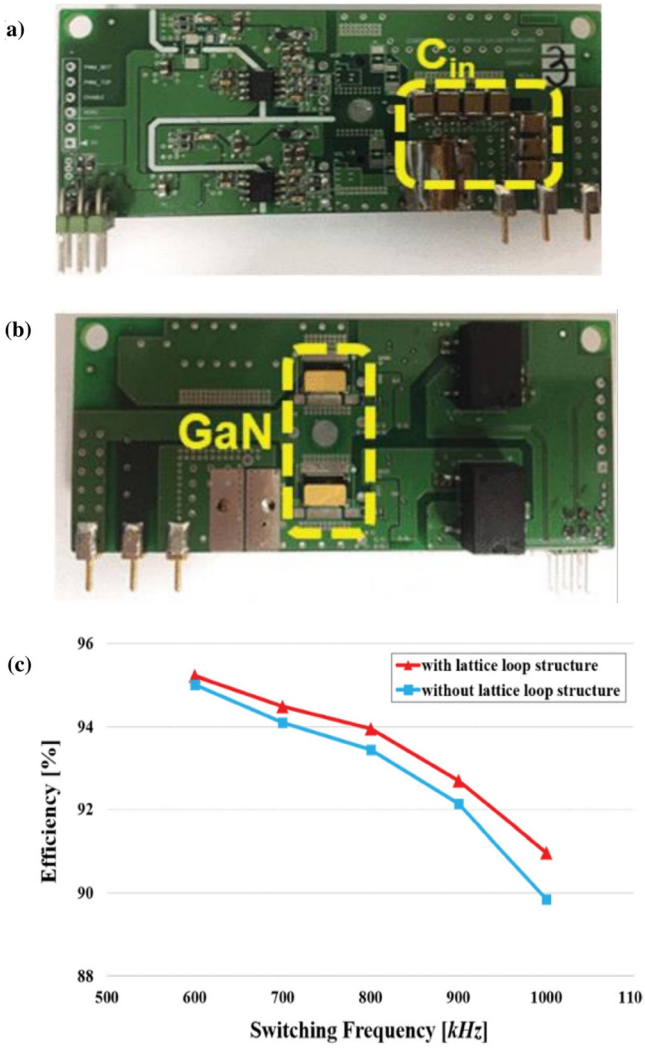

FIG. 22. A photograph of the PCB with the proposed vertical lattice loop design. (a) Top view, (b) bottom view. (c) Efficiency curve comparison between with lattice loop and without lattice loop.[186] Yang *et al.*, IEEE Access **10**, 117215 (2022), licensed under a Creative Commons Attribution (CC BY) License.

Ultimately, all of the aforementioned converters demonstrated superior efficiency for the OBC. The DAB converter exhibited significant parasitic inductance, which can be mitigated by implementing a vertical loop topology. However, due to its versatile and costly design, the DAB bidirectional converter remains the optimal choice for on-board charging (OBC) in electric trains.

D. Electric ships

Ship electrification improves mission capability, system efficiency, and operating costs.[191] It offers notable advantages, mostly due to the reduced space requirements for installing electrical propulsion machinery compared to conventional systems. Consequently, this results in increased available load space within a ship. The majority of modern ships, which are normally hybrid ships, are now equipped with mechanical combustion engines that are paired with electrical motors, much like the motors found in EVs. Figure 23(a)[192] is a schematic block diagram of hybrid ships. Different types of inverters have been used to run those electric motors on the ships. Additionally, radars are also equipped with inverters, which are included for the purpose of providing navigational assistance to ships. Before the use of radar on ships, navigation was accomplished by the use of visual means. This resulted in a number of downsides, such as the fact that it was extremely challenging to navigate in low visibility or for any other reason that prevented us from becoming aware of the goal. This led to a significant number of collisions at sea during the period of poor visibility. The radar in the maritime business is a blessing for mariners since it provides assistance to navigators in any circumstance, regardless of the weather, the traffic circumstances, or the visibility requirements. Contreras *et al.*[193] introduced a resonant topology for a half bridge using GaN material. This work presents a new and innovative hybrid flyback topology. The flyback topology has several advantages. The isolated topology is superior to non-isolated topologies in terms of safety and the removal of leakage ground currents,[194] primarily due to the presence of galvanic isolation.[195] Due to its lack of energy storage, this topology has a smaller transformer compared to flyback-based topologies.[196,197] Additionally, it offers a broader voltage range compared to LLC-based topologies, while attaining equivalent efficiency without the need for a large number of components.[198,199] Furthermore, employing resonant behavior through techniques such as ZVS and ZCS enables the use of higher frequencies, resulting in reduced volumes.[200] Additionally, this approach facilitates the incorporation of wideband gap semiconductors. Figure 23(b) displays the planned asymmetrical half bridge flyback converter. The 100-W prototype, which operates between an input voltage range of 320–380 V and an output range of 5–20 V, demonstrated a significant level of efficiency, with a maximum efficiency of 97%. The study also examines the thermal management of the converter. The thermal picture of the converter is depicted in Fig. 23(c). Based on the picture, it is evident

21 October 2024 08:24:33

© Author(s) 2024

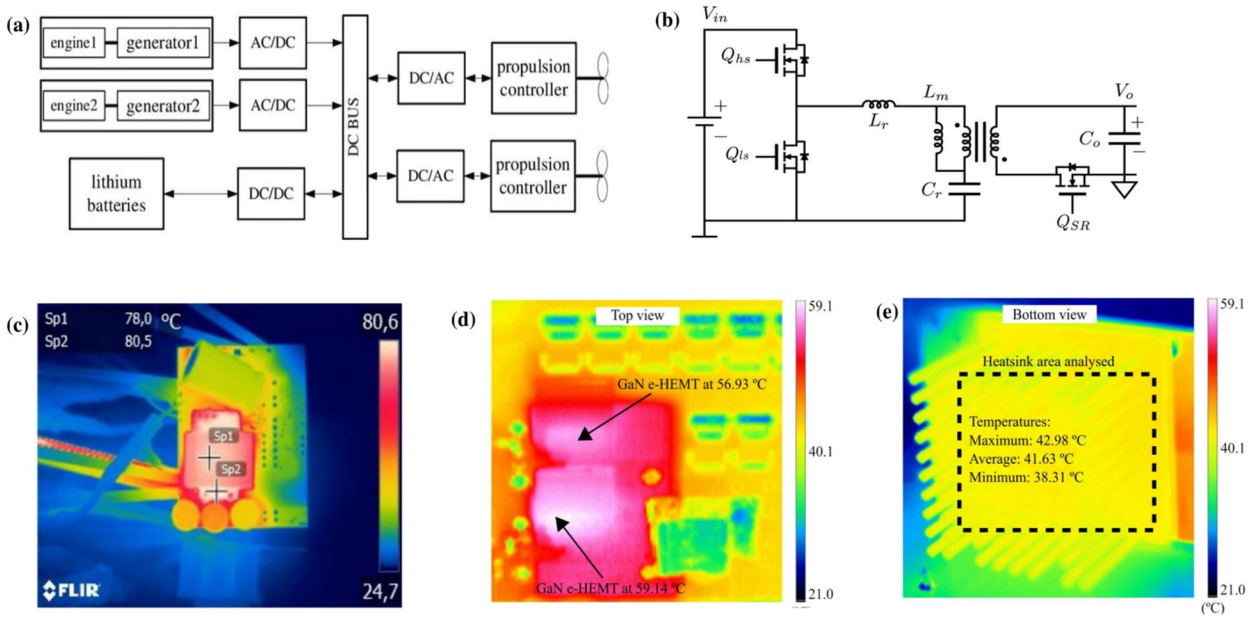

FIG. 23. (a) Schematic block diagram of hybrid ships.[192] Reproduced with permission from Gao *et al.*, Energies **11**, 1699 (2018). Copyright 2018 MDPI. (b) Proposed flyback converter. (c) Thermal image of the flyback converter.[193] Reproduced with permission from Contreras *et al.*, J. Electron. Commun. **174**, 155056 (2024). Copyright 2024 Elsevier. Thermal image of bottom side cooled inverter: (d) top view and (e) bottom view.[202] Reproduced with permission from Lumbreras *et al.*, Energies **14**, 6287 (2021). Copyright 2021 MDPI.

that the converter operating at full load has attained a temperature of 80.5 °C, which is considered to be excessive. The solution to this issue can be achieved by utilizing a heat-conductive electrical-insulation material. Oyane *et al.*[201] proposed a half bridge GaN HEMT resonant inverter. A novel passive L-S network has been suggested in this study for the circuit, which fulfills the design criteria of zero voltage switching (ZVS), minimal output harmonics, and high power with minimal loss, while keeping the drain-source voltage constant. The L-S network comprises an impedance converter known as the "L-network" as the initial stage, followed by a series resonator as the subsequent step. The half-bridge circuit guarantees the stability of the voltage between the drain and source terminals. The impedance converter provides both high output power and zero voltage switching (ZVS) operation concurrently. Additionally, the series resonator effectively suppresses harmonics. Each function is established by a specialized and autonomous design of each component. The suggested inverter possesses the capability to generate a substantial amount of power without being limited by the drain-source voltage and load. In the suggested configuration, a component known as an L-network impedance converter is placed between the half-bridge switch and the output series resonator. The authors designated this passive network as the "L-S network." The proposed L-S network allows for the separation of circuit design for noise suppression from circuit design for impedance conversion and high output power. The ability to construct circuits with flexibility allows for the generation of high-output power for high-frequency sinusoidal waves. The watts of the output power is governed by the architecture of the L-network, which converts impedance. It has the capability to provide a significant amount of power to loads with high resistance, hence broadening the scope of potential uses in comparison to traditional converters. In addition, the L-network is employed as an inductive reactance to provide zero voltage switching (ZVS) functionality for GaN-HEMT switches S1 and S2. The L-network and series resonator can be separately built in the suggested topology. ZVS may be readily accomplished due to the substantial current in the half-bridge and the efficient withdrawal of electric charges from the output capacitance of switch S1 or S2 during turn-on periods. While significant drain currents are present in S1 and S2, this is not a concern since it is expected that GaN-HEMTs with permissible currents in the range of tens of amperes are being utilized. The theoretical design and computer simulations confirmed that the output power of 3 kW was achieved at a frequency of 13.56 MHz, with a drain-source voltage of 280 V and a load impedance of 50 Ω. The suggested topology's usefulness was confirmed by experimental data. An impressive conversion efficiency of 99.4% was attained when the output power reached 471.4 W. In addition to that, the thermal condition of the prototype is investigated in this study. The study also showed that GaN HEMT on the high side exhibited a high temperature, which is one of the issues with the device. Table X shows the recent findings on different GaN LLC inverters of motor drives for electrifying ships.

Lumbreras *et al.*[202] conducted a study to investigate the impact of the heat dissipation system on GaN-based power converters. This work involves the modeling of several heat dissipation systems. The analysis focuses on two dissipation systems: bottom-side dissipation using thermal vias, and top-side dissipation employing various thermal interface materials. The figure displays the thermal model converter, illustrating dissipation on both the top and bottom sides. The heatsink of the 250 V, 400 kHz switching frequency, 574.5 W output power converter has shown significant effectiveness in reducing the temperature.

21 October 2024 08:24:33

© Author(s) 2024

TABLE X. Recent findings on different GaN LLC inverter of motor drive for electrifying ships.

Device type	Voltage (V)	Power (kW)	Power density (kW/l)	Frequency (kHz)	Efficiency (%)	Ref.
GaN LLC half bridge	380	0.1	···	···	97	182
GaN HEMT	280	0.471	···	1356	98.7	183
GaN HEMT	250	0.5745	···	400	···	184
GaN LLC	380	0.8	55.3	1000	97.6	203
GaN LLC	400	0.8	55.3	1000	97.7	204
GaN LLC	···	0.8	55.3	1000	97.4	205
GaN LLC	350	1.5 k	···	600	97.8	206
GaN LLC	12/48	···	14	300	95	207
GaN LLC	600	···	8.6	···	98.3	208
GaN LLC	400	3	8.6	350	98.4	209

Figure 23 displays thermal photos of the underside of the cooled converter. Figure 23(d) depicts a top view of the PCB. Here, the transistors were the most thermally active components of the converter. The temperature of the top GaN was 56.93 °C, whereas the temperature of the bottom GaN was 59.14 °C. The figure also illustrates the thermal conduction of heat from the transistors through the copper thermal plane. Figure 23(e) depicts a perspective from the underside of the converter. This thermogram displays the heatsink and its corresponding temperature. The heatsink maintained an average temperature of 41.63 °C during steady state. Figures 24(a) and 24(b) display the thermal images of the upper surface of the cooled converter, which includes a heatsink. The upper surface of the cooled inverters was fitted with two layers of thermal interface material (TIM). One option is the use of Graphite enhanced TIM, which resulted in an average temperature of 45.39 °C when measured from the top perspective and 43.68 °C when measured from the lateral view. Another option is Polymer TIM, with an average temperature of 40.5 °C in the top view and 39.20 °C in the lateral view. The converter equipped with the graphite-enhanced TIM exhibits superior heat conduction, resulting in the highest temperature in its heatsink. This TIM possesses a slender physical profile and exhibits an exceptionally elevated thermal conductivity inside the plane. These two features reduce the thermal resistance of the system, hence

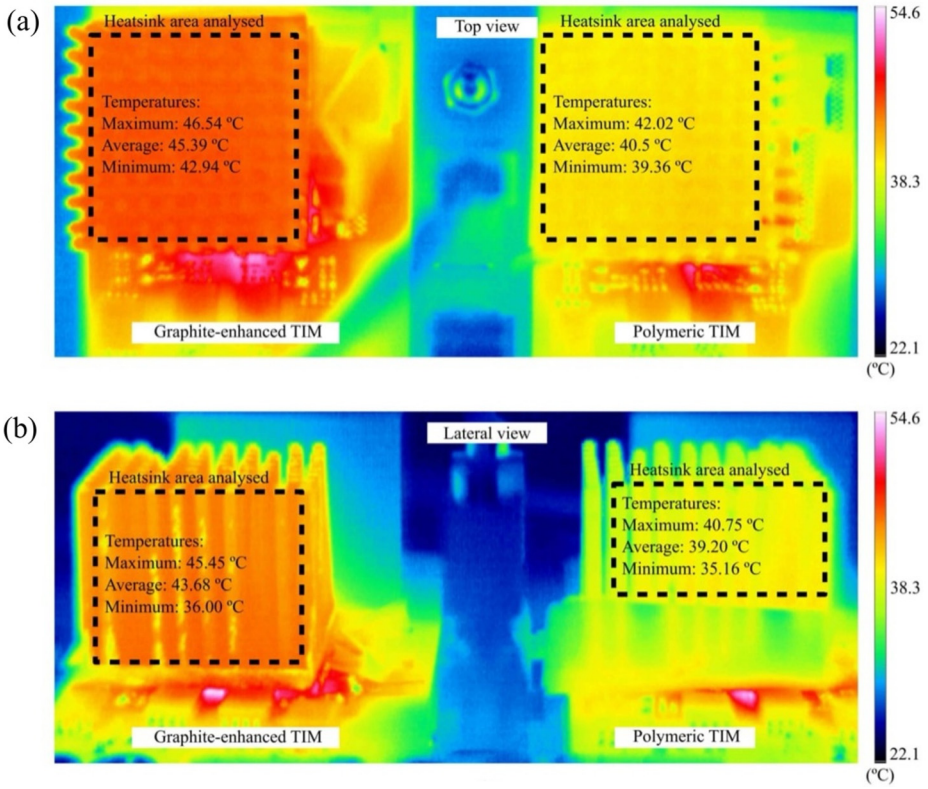

FIG. 24. Thermal image of top side cooled inverter (a) Top view (b) Lateral view.[202] Reproduced with permission from Lumbreras *et al.*, Energies **14**, 6287 (2021). Copyright 2021 MDPI.

21 October 2024 08:24:33

© Author(s) 2024

enhancing heat dissipation. The converter equipped with the polymeric TIM exhibits a greater level of thermal resistance. The polymer TIM has reduced heat conductivity and possesses a greater thickness. As a result, the dissipation of heat is less effective, and the temperature of the heatsink is somewhat lower. Upon analysis of both top and bottom cooled converters with heat sink, it is evident that bottom-cooled power converters display substantial parasitic inductance, resulting in elevated voltage ringing. The existence of thermal vias is responsible for this phenomenon. Top-cooled power converters offer a more efficient structure compared to bottom-cooled converters because they eliminate the need for thermal vias. Therefore, the level of parasitic inductance is expected to be negligible. In summary, one of the key components of the electric motor that powers a ship's engine system is an inverter or converter. GaN is a very favorable choice for converters and inverters due to its exceptional properties. However, its low thermal conductivity and compact size pose significant challenges for dissipating heat effectively. Insufficient thermal management can lead to a higher junction temperature, which in turn lowers efficiency and may even result in device failure. There is a conflict between performance and manufacturing costs when it comes to using different heat conductive insulating materials to enhance thermal behavior.

E. Electric submarines

Submarines and the ability to go below the surface of the ocean have been the holy grail for sailors since the beginning of time. There have been a number of advancements made in submarine technology. An integrated electrical propulsion system, also known as an IEPS, is being included into the design of most current Chinese submarines. The Chinese model is the first of its sort anywhere in the world since it is the first deployment of an IEPS that functions on a medium-voltage, direct-current infrastructure. Instead of translating the output of the ship's engine and reactor into mechanical action in order to rotate the propeller shaft, the IEPS is able to convert the whole output of the ship's engine into electricity.[210] This is in contrast to traditional propulsion systems, which convert electrical energy into mechanical energy. To convert electrical energy into mechanical energy, an electric motor is needed. To drive an electric motor, GaN is an excellent candidate. Electric motor inverters consist of loops of wire in a magnetic field. When current is passed through the loops, the magnetic field exerts torque on the loops, which rotates the shaft. Thus, electrical energy is converted to mechanical energy. Recently, three-phase leg inverters have been widely used in energy conversion systems. Alatawi *et al.*[211] developed GaN-based single-phase inverter. This study presents a thorough analysis of the losses in a newly updated topology based on the H5 inverter. The novel topology creates an alternative current path to minimize conduction losses by minimizing the number of conducting switches during the active state. Hence, the present suggested configuration in the active state passes via four switches. The suggested topology has obtained the lowest conduction losses when compared to both the H5 topology and the H6 topology. In addition, a comprehensive analysis of the utilization of GaN and Si devices for the suggested configuration is also incorporated. The loss comparison research uses datasheet information, conduction losses, switching losses, and heat sink requirements to provide a precise comparison of GaN and Si power devices. The study also conducted a thorough analysis of the operating modes, inverter structure, and switching techniques in the proposed topology. Sinusoidal pulse width modulation (SPWM) is utilized to maintain a consistent common mode (CM) voltage throughout all operational modes and minimize the amount of leakage current. Figure 25(a) shows the proposed inverter's circuit. The figure illustrates a novel transformer-less inverter design, in which high frequency switches S2, S4, S5, and S6 are employed, while low frequency freewheeling switches S1 and S3 are utilized. The introduction of the new topology results in the formation of fresh current pathways, leading to a reduction in conduction loss as compared to the H5 topology. Hence, the suggested topology in the active mode is characterized by the passage of current across four switches. Consequently, when compared to the H5 and H6 topologies, the suggested topology has successfully attained the lowest conduction losses. The 5-kW inverter demonstrated high efficiency across several switching frequencies. The input voltage of the inverter was 400 V, while the output voltage was 120 V. The switching frequency ranged from 50 to 200 kHz. Figure 25(b) displays the efficiency of Si MOSFET and GaN HEMT inverters at switching frequencies of 50 and 200 kHz. The graphic illustrates that the switching device power losses have a direct impact on the overall efficiency of the system. The figure also illustrates the enhanced efficiency achieved by employing GaN HEMTs, with an increase in over 2% at 50 kHz and over 3% at 200 kHz. These findings therefore confirm the GaN switching devices' better performance compared to their Si equivalents. Similarly, Zhang *et al.*[212] proposed a single-phase GaN HEMT inverter. The cascode GaN HEMT is a commonly used device for high voltage applications involving wide-bandgap devices. The device's unique shape increases the complexity of its operation compared to both regular Si MOSFETs and the improved GaN HEMTs. This study assesses a cascode GaN HEMT-based inverter with a voltage rating of 600 V. The dynamic process analysis of a single-phase inverter circuit based on cascode GaN HEMT is described, using the working process analysis of cascode GaN HEMT as the basis. Furthermore, the model takes into account the impact of parasitic factors, and derives the essential equations for each mode. Additionally, the impact of parasitic factors on the switching process of the switch is examined. Figure 26(a) shows the topology of the proposed cascode GaN HEMT-based inverter, and Fig. 26(b) shows the control strategy of the proposed cascode GaN HEMT-based inverter. The GaN cascode device with a power output of 500 W demonstrated excellent efficiency. Figure 26(c) shows the efficiency curve of different switching frequencies. The inverter has an input voltage of 380 V and an output voltage of 220 V. It operates at a switching frequency ranging from 20 to 100 kHz. From Fig. 26(c), the efficiency at 100 W is 92.6% when the switching frequency is 20 kHz. The efficiency then rose to 94.3% when the power output reached 200 W. It steadily increased and reached its maximum point at 95.6% when the power output was 300 W. The efficiency is constant up to 400 W. Subsequently, the efficiency began to decline and eventually reached 95.1% at 500 W. The efficiency at a switching frequency of 50 kHz was measured to be 95.1% when operating at a power of 100 W. Subsequently, the efficiency surges to 96.8% when the power output reaches 200 W. It steadily increases until it reaches its maximum value of 97.4% at 300 W. Subsequently, the efficiency exhibited a decline, reaching 97.2% when the power output was 400 W. Subsequently, it increased to 97.1% when the power output was set at 500 W. The efficiency at 100 W at a switching frequency of 100 kHz was 97%. Subsequently, it progressively rose to 98% when the power reached 200 W. Following that, the efficiency of the system achieved its maximum value of 98.3% when operating at 300 W. The efficiency

21 October 2024 08:24:33

© Author(s) 2024

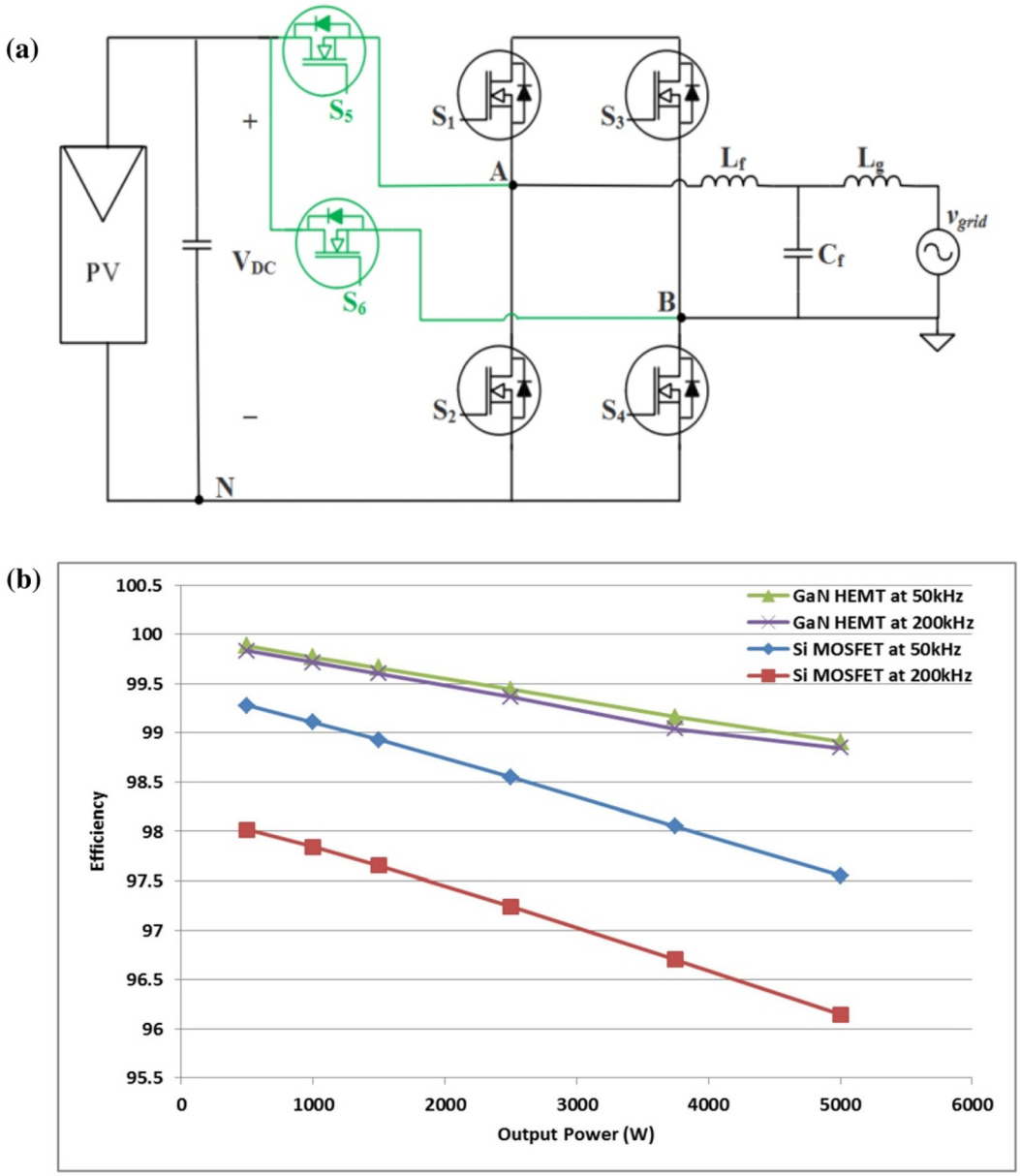

FIG. 25. (a) Proposed H5 topology. (b) Efficiency on different switching frequency.[211] Reproduced with permission from Alatawi *et al.*, Electronics **7**, 34 (2018). Copyright 2018 MDPI.

then declined to 98.2% when the power output reached 400 W. Finally, the efficiency peaked at 98.1% when the power output was 500 W. From the figure, it is also seen that as the switching frequency increases, the inverter experiences a rise in switching loss and a fall in overall efficiency. The figure also illustrates that the highest efficiency point is around 300 W, representing a trade-off between the switching loss and the filter loss. When the power level is low, the switching loss becomes the primary factor. As the power grows, the loss of the filter inductance also increases and becomes the main factor. Table XI shows the previous findings on different inverters for submarines.

The previously mentioned single-phase inverters exhibit high efficiency and straightforward construction. Nevertheless, this straightforwardness is accompanied by several drawbacks. Single-phase inverters exhibit less power output and less reliable voltage control, rendering them less appropriate for applications requiring large-scale or high-power capabilities. Three-phase inverters can solve this problem. Three-phase inverters offer additional benefits, including a higher power transmission capacity compared to single-phase ones. This feature makes them well-suited for spacious residences or business establishments with substantial energy requirements. In addition, they have

21 October 2024 08:24:33

© Author(s) 2024

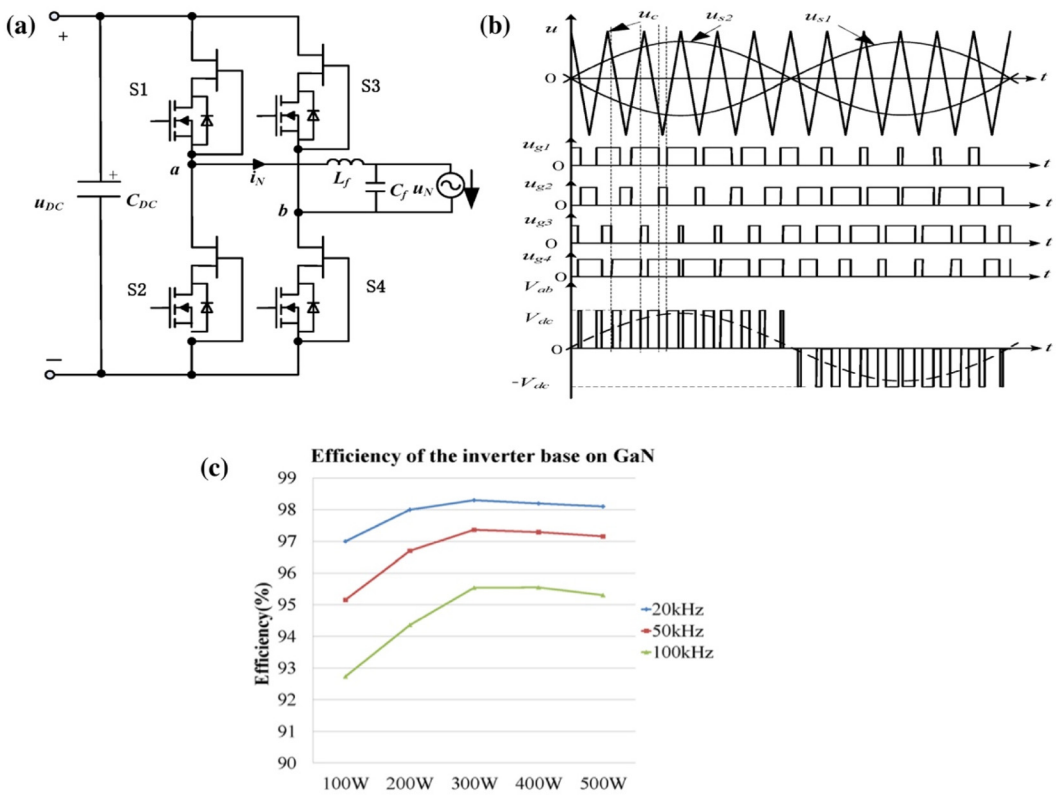

FIG. 26. (a) The topology of the proposed cascode GaN HEMT-based inverter. (b) The control strategy of the proposed cascode GaN HEMT-based inverter. (c)Efficiency curve of cascode GaN HEMT inverter.[212] Reproduced with permission from Zhang *et al.*, Energies **15**, 7791 (2022). Copyright 2022 MDPI.

TABLE XI. Recent findings of different inverters for electrifying different submarine modules.

Device type	Voltage (V)	Power (kW)	Power density (kW/l)	Frequency (kHz)	Efficiency (%)	Ref.
GaN single-phase inverter	400	5	···	200	99.7	211
GaN HEMT cascode	600	0.5	···	100	98.3	212
GaN active filter	···	2	···	80–100	97.2	213
IGBT	540	8	···	50	98	214
MOSFET	100	1.5	···	6	95	215
SiC inverter	···	8.8	···	50	97.2	216
GaN	···	2	5.58	···	96.5	217
GaN FET	450	2	3.43	···	98	218
MOSFET	450	2	14.77	0.06	98.1	219
GaN	450	2	13.29	0.12	97.6	220

the capability to decrease energy expenses and enhance the overall efficiency of the electrical system. Ma *et al.*[213] proposed a three-phase GaN-based inverter. This study outlines the fundamental design process and showcases, for the first time, the effectiveness of a 2-kVA GaN-based three-phase shunt APF active power filter (APF) system. The primary component of an APF system is a power converter that achieves the necessary power quality control functions by effectively controlling the switching of power electronic devices. Typically, it is linked to the point of common coupling (PCC) either in parallel or in series to carry out its intended activities. However, shunt APFs are more frequently utilized due to their ability to offer more versatile compensatory functions through current-injecting control and their reduced need for additional equipment. A unified power quality conditioner (UPQC) refers to the simultaneous connection of a series active power filter (APF) and a shunt APF over a shared direct current (DC) link. Figure 27(a) shows the proposed circuit. The figure illustrates the

21 October 2024 08:24:33

© Author(s) 2024

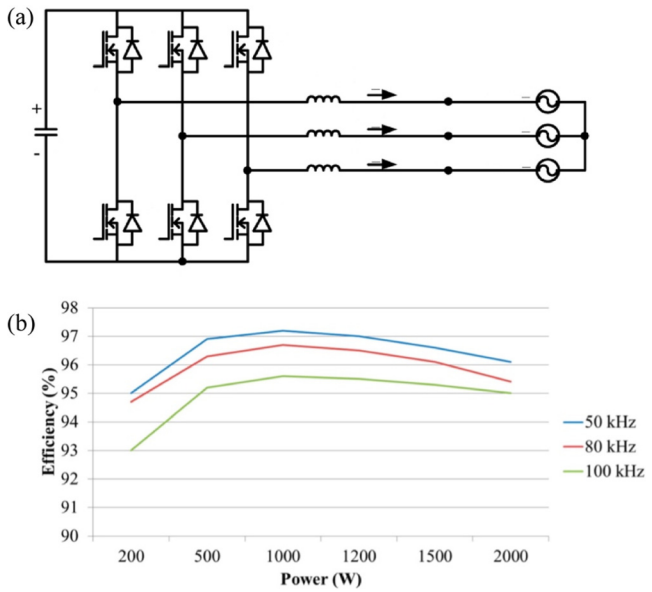

FIG. 27. (a) Proposed three-phase inverter. (b) Efficiency curve of different switching frequency.[213] Reproduced with permission from Zhang *et al.*, Micromachines **11**, 134 (2020). Copyright 2020 MDPI.

use of dual-loop control techniques for the regulation of the DC link voltage. The inner loop is responsible for managing the inductor currents, while the outer loop is responsible for regulating the DC link voltage. By manipulating the currents in the inductor, it is possible to achieve the objectives of regulating the voltage in the DC link and correcting for the harmonics, unbalanced, and reactive components of the load currents. The 2-kVA, 200-V inverter demonstrates exceptional efficiency across several frequencies (50, 80, and 100 kHz), with a maximum efficiency of 97.2%. Figure 27(b) illustrates the varying efficiency of the inverter at different switching frequencies. From Fig. 27(b), it can be seen that the highest efficiency is observed at around 50% of the rated load. Additionally, it is evident that increasing the switching frequency leads to a loss in efficiency. This is mostly attributed to the rise in switching losses. In short, the electric motor inverter plays a crucial role in operating the IEPS system of the submarine. Both the single-phase inverter and the three-phase inverter have demonstrated favorable outcomes. Nevertheless, the use of a three-phase shift inverter has successfully addressed the design challenges and significantly enhanced the efficiency of the device, making it a more viable choice.

V. CHALLENGES FOR GaN IN EV

A. Cross-talk

Cross-talk one of the main issues that arise while working with GaN power integrated circuits. It is one of the fundamental challenges. When it comes to half-bridge topology, this is truly one of the most widespread and significant issues. A high d U_{DS}/dt of one switch will interact with the parasitic capacitance of its complementary switch, which will result in the generation of crosstalk voltage. There is a possibility that one of the switches could be activated by accident due to the presence of positive crosstalk voltage, which would result in the risk of shoot through. On the other hand, the GaN device has a lower gate threshold voltage and a faster switching speed than the Si device, which is more likely to flip on unexpectedly.[221,222] There is a high probability that the negative crosstalk voltage may surpass the negative maximum gate–source voltage range, which subsequently leads to the device being damaged or experiencing accelerated performance deterioration.[223] Utilizing a negative turn-off voltage is a widely employed technique for mitigating crosstalk. The use of a negative driving voltage by Jia *et al.*[224] has a specific inhibitory impact on the positive crosstalk voltage, but it also immediately increases the peak value of the negative crosstalk voltage. Applying a negative driving voltage will intensify the impact of reverse conduction loss. The driving circuit developed by Gao *et al.*[225] utilizes a voltage divider circuit and a passive auxiliary power switch to successfully decrease the peak value of negative crosstalk voltage and provide negative driving voltage. However, it still incurs significant reverse conduction loss. Chen *et al.*[226] introduced a design approach for an attenuated negative driving voltage power supply. This method ensures that negative voltage is supplied during positive crosstalk to prevent any misleading effects. Additionally, the negative voltage gradually decreases to zero before negative crosstalk occurs, thereby preventing any negative overvoltage breakdown. Nevertheless, the forward-flyback converter results in elevated expenses and intricate circuitry. Kashyap *et al.*[227] examined the crosstalk voltage value and efficiency in a GaN-based buck prototype. They investigated the effects of various driving resistance, negative driving voltage, and dead time on these parameters. The researchers identified the combination of parameters that yielded the highest efficiency while maintaining reliability. However, this determination required extensive experimentation, and the results cannot be universally applied. Haihong *et al.*[228] introduced a negative voltage driving circuit for a cool GaN HEMT in a phase leg configuration. The study shows that the active negative voltage driving circuit has the ability to both mitigate the crosstalk impact and significantly decrease the reverse conduction loss resulting from negative driving voltage. This allows for a harmonious balance between the dependability and loss of the bridge-arm circuit. The impact of both positive driving voltage and acceleration capacitance on reliability and loss is not consistent. Therefore, it is necessary to design them in conjunction with each other in order to maximize the parameters. According to Fig. 28,[228] the CoolGaN HEMT exhibits rapid switching speed and minimal oscillation. The crosstalk voltage is capable of satisfying the crosstalk suppression criteria of the bridge arm. Hence, the suggested active negative voltage driving circuit achieves a shutdown mode that combines negative-voltage and zero-voltage, exhibiting excellent stability and speedy response.

B. Gate leakage current

One of the most important parameters for GaN is the gate leakage current, which has a direct connection to both the device's performance and its dependability. While the reversal of the forward gate leakage current may result in off-state power consumption and a lowering of V_{BR}, the forward gate leakage current restricts the gate voltage swing and causes driving losses.[229] This is because the forward gate leakage current restricts the gate voltage swing and causes drive losses. It is not acceptable to allow excessive gate leakage currents since they have the potential to result in unneeded power consumption. Therefore, in order to avoid the possibility of power loss, it is possible switch off the drain current by setting the Schottky gate to a reversed bias. As a result of this, research studies on gate leakage mechanisms

21 October 2024 08:24:33

© Author(s) 2024

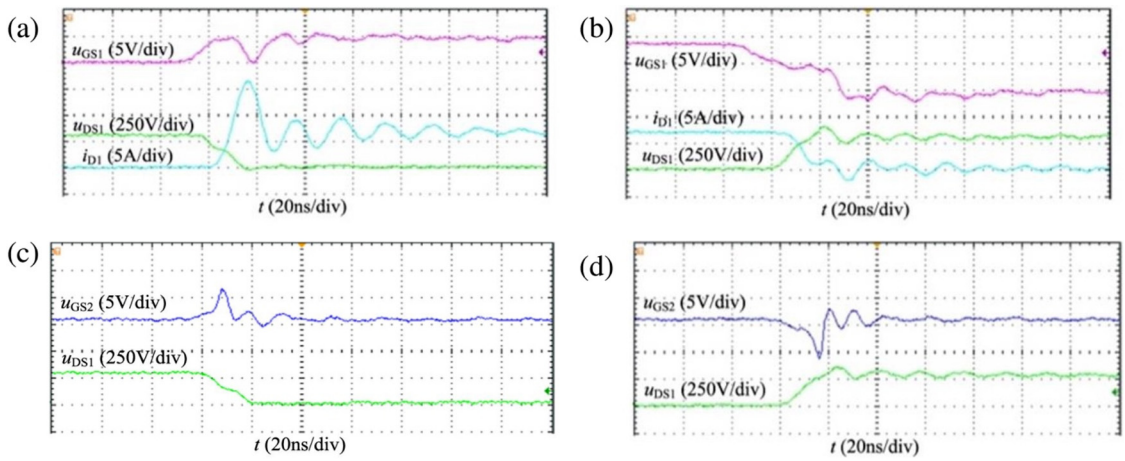

FIG. 28. The waveform of (a) turn on and (b) turn off switching process and the waveform of (c) positive crosstalk voltage and (d) negative crosstalk voltage interference.[217] Reproduced with permission from Qin *et al.*, Energy Rep. **8**, 780–788 (2022). Copyright 2022 Elsevier.

are frequently linked to problems regarding peak electric field distribution and current collapse.[229] The peak electric field causes a significant reduction in the supply of active electron traps that are located between the gate and the drain, which ultimately leads to a lower current collapse and knee exit.[230] Because of this, gate insulators need to have significant band offsets and large band gaps in order to reduce gate leakage current, even when the bias is in the forward direction.

To reduce gate leakage, including a gate insulator layer between the AlGaN barrier layer and the gate metal is one way.[231] There have been numerous dielectric materials studied for use in gate insulator applications. Some of these materials include hafnium dioxide (HfO_2), silicon dioxide (SiO_2), aluminum oxide (Al_2O_3), silicon nitride (SiNx), and zirconium dioxide (ZrO_2). High-k dielectrics, in particular, offer the possibility of channel controllability that is particularly advantageous for low off-state leakage currents, high on-to-off ratios, which suggests enhanced power efficiency in device applications. Table XII shows the dielectric properties of high-k materials that are frequently utilized.

C. Dynamic performance

Another significant obstacle faced by a GaN is the phenomenon of current collapse, which refers to the dynamic on-state resistance $R_{DS(ON)}$. The decrease in the dynamic on-state resistance $R_{DS(ON)}$ following the transition from a high voltage off state poses a hindrance to the practical implementation of these devices. Currently, there are two physical mechanisms that have been suggested to elucidate the degradation of $R_{DS(ON)}$. The trapped electrons[235,236] originate from the surface traps located between the gate and drain area, as well as the buffer traps beneath the two-dimensional electron gas (2DEG) channel. These traps are produced by a strong electric field across the drain-to-substrate in the off state. Figure 14[237] displays the dynamic $R_{DS(ON)}$ values of GaN-HEMT caused by trapping effects. Another type of electron, known as hot electrons[238,239] is produced within the channel. These electrons have the ability to be injected into and captured by either the surface or the buffer stack when high voltage switching transients occur. Despite the implementation of many sophisticated device technologies, such as field plate[240] and optimized buffer design,[241] the issue of dynamic $R_{DS(ON)}$ fluctuation remains a significant challenge for commercially available GaN devices. In the past, the majority of reports mostly concentrated on analyzing devices at the individual level or doing research to improve the quality of materials. To accurately forecast the performance of a GaN converter, it is crucial to thoroughly examine the impact of dynamic on-state resistance. It is advisable to avoid relying on static $R_{DS(ON)}$ values when assessing conduction loss. The double pulse test (DPT) is a commonly employed technique for determining the dynamic resistance on-state ($R_{DS(ON)}$) of power devices during switching under challenging

TABLE XII. Different high k materials properties. Data have been taken from Refs. 233 and 234.

Materials	ε (F m^{-1})	C (J K^{-1})	K (W m^{-1} k^{-1})	Energy gap (eV)	Ec (eV)	Ev (eV)
SiO_2	3.9	3.066	0.014	9	3.5	4.4
SiN	7.5	0.585	0.185	...	...	...
Al_2O_3	9.3	3.14	0.29	8.8	3	4.7
HfO_2	22	...	...	5.8	1.4	1.3
TaO_5	26	...	...	...	...	...
TiO_2	80	...	...	3.5	1.1	1.3

21 October 2024 08:24:33

© Author(s) 2024

situations.[242–245] The switching transients of the device under test (DUT) can be recorded during the second pulse when the desired voltage and current are applied. Therefore, the increase in junction temperature caused by switching loss can be disregarded. This method allows for the investigation of the impact on dynamic $R_{DS(ON)}$, which includes off-state time, off-state voltage, drain current, temperature, frequency, duty cycle, and gate voltage. Furthermore, the data obtained from dynamic power testing (DPT) can offer valuable insights for the design of converters. These insights include determining the appropriate switching frequency and dead time selections, optimizing thermal management, and estimating efficiency.[246,247] The previous discussion has previously covered the influence of gate characteristics,[248] off-state voltages,[246,249] and continuous operating mode.[250] The duration of the off-state period prior to the initial gate pulse is a crucial component that might impact the trapping phenomenon and thus introduce uncertainty in the $R_{DS(ON)}$ value. Nevertheless, there are not many reports that address this problem. Wei *et al.*[251] examined the dynamic on-resistance characteristics of a GaN HEMT device with a p-GaN gate under hard-switching conditions. The dynamic $R_{DS(ON)}$ exhibits a non-monotonic behavior, initially rising to 1.22 times the static value and subsequently declining as the off-state voltage increases. The multi-pulse test suggests minimal frequency correlation and dynamic resistance degradation when compared to the real-world application.

D. Thermal management

Improving the reliability of power converters requires a significant amount of work focused on maximizing the effectiveness of thermal control for GaN devices.[252] The issue of self-heating in HEMTs is of great importance since it can lead to the localized accumulation of high power density and uneven dissipation of heat. This problem is further substantiated by the temperature-dependent nature of several properties of these devices, such as electron mobility, saturation rate, and thermal conductivity. As semiconductor technology has advanced, designers have consistently raised the power density of power devices, resulting in higher channel temperatures and lower drain currents (I_{DS}). In GaN-based HEMTs, a high drain bias (V_D) is employed to achieve high-power and high-frequency functionalities, resulting in the generation of a robust lateral electric field originating from the drain electrode side at the gate edge. Consequently, the temperature of the nearby lattice increases, which is referred to as the self-heating phenomenon. Practically, excessive overheating ultimately diminishes the lifespan of GaN devices or leads to irreversible harm,[253] greatly affecting their long-term usage.[254] Currently, commercial GaN HEMTs are limited to an output power of 2–4 W mm^{-1}, although power amplifiers have demonstrated a power output of 40 W mm^{-1}. Reducing the structural temperature would consequently improve the power efficiency and reliability of devices in the long term.[255–257] Similarly,[258] it was shared that component self-heating was the main cause of operational temperatures over critical levels, which in turn led to HEMT technology failures. Self-heating can lead to several problems such as gate burying, damage to the link between the chip and the package, degradation of electron mobility, and a drop in current.[259] Therefore, it is crucial to prioritize thermal management during the design phase[260–263] in order to minimize performance deterioration and enhance dependability.[264,265] The thermal performance of HEMT devices is generally affected by the substrate materials they are used on. GaN-based HEMT often involves the growth of epitaxial layers on a substrate that is different from the GaN material itself. Commonly used substrates include sapphire, silicon (Si), silicon carbide (SiC), and diamond. Figure 29[266] provides a thermal analysis of various materials. These substrates with dissipative properties aid in reducing thermal mismatch while enhancing thermal stability.[267] Additionally, it has been found that using a substrate with high resistance can improve the capacity to withstand breakdown, but there is always a compromise between maintaining a stable threshold voltage and the cost of the material.[268]

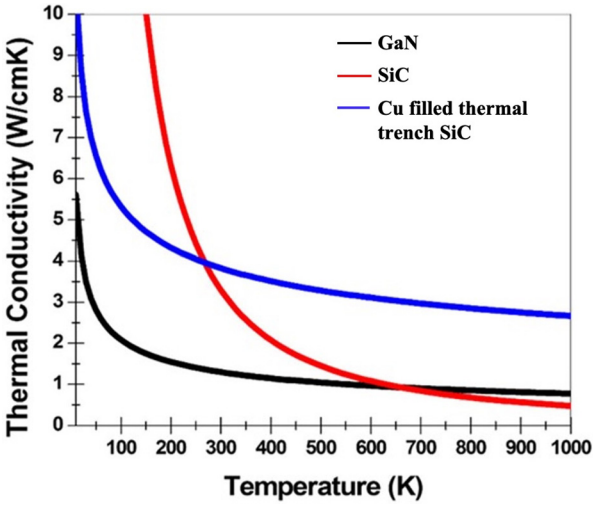

FIG. 29. Thermal Conductivity profiles for GaN, Sic, and Cu filled thermal trench SiC substrate.[266] Reproduced with permission from Jang *et al.*, Micromachines **11**, 53 (2020). Copyright 2020 MDPI.

VI. CONCLUSION AND FUTURE PROSPECTS

Due to the challenges in the transportation sector related to bulk and volume, there is an obvious demand for designs that are lighter without sacrificing efficiency. GaN has desirable characteristics such as a high switching frequency, high power density, and high breakdown voltage, which make it well-suited for use in this particular sector. In the past 5 years, a significant development of GaN devices has been seen in EV industry. The use of GaN in chargers yields significant benefits. Due to its elevated switching speed and enhanced heat resistance, it enables chargers to achieve higher efficiency, smaller size, and faster charging of devices. GaN converters and inverters in motor drives have significantly improved motor efficiency while simultaneously decreasing dimensions, weight, and expenses. This facilitates the development of motor systems that are compact, lightweight, quieter, possess higher torque, have an extended range, and improved accuracy. Turning now to potential GaN devices in non-automotive vehicles, it has been shown that GaN devices have greater advantages over other semiconductor devices. For instance, the efficiency of an aircraft's monitoring system has been improved with a GaN rectifier. GaN-based inverters and converters in electric ships and submarines may significantly enhance propulsion power with exceptional efficiency. The implementation of GaN-based converters in electric trains enables the attainment of a greater power density in the traction equipment, resulting in cost and energy efficiency. That being said, although

21 October 2024 08:24:33

© Author(s) 2024

tremendous improvements have been made in GaN device performance in these fields, it still has significant challenges that need to be addressed, such as high manufacturing costs, gate leakage current, and self-heating issues.

The future prospects for the rapidly expanding GaN-based EV are quite positive. Artificial intelligence (AI) technologies are revolutionizing the safety and efficiency of EVs by gathering sensor data and analyzing deviations from the standard. Rectifiers can be utilized to gather these data. These systems specifically evaluate the state of EVs and their batteries, allowing owners and fleet operators to take preemptive measures to avoid costly repairs. AI-based health monitoring is projected to become more widespread in the future with the use of GaN-based rectifiers. Advanced Driver Assistance Systems (ADAS) are a set of technology-driven features that use sensors and controls to improve driving safety and comfort. They do this by monitoring the surrounding environment for the presence of other cars and pedestrians. These data are used to provide immediate recommendations, such as emergency braking and parking assistance, which greatly contribute to the safety of EVs. Future ADAS are anticipated to employ GaN-based sensors, which should improve driving efficiency, safety, and comfort. GaN transistor equipped vehicle-to-everything (V2X) technology facilitates the exchange of information between software controllers and internal and external components. This includes remote diagnostics, location-based services, monitoring of current charge levels, and over-the-air software upgrades. This technology is now in the trial phase and is likely to be extensively used in the future. The scarcity of charging stations is a significant challenge for EVs since the current charging infrastructure is insufficient. To remedy the issue, it is recommended to install additional charging stations that are equipped with GaN power devices because GaN power devices are advantageous due to their high efficiency, compact size, fast charging capabilities, energy efficiency, enhanced safety features, and wide compatibility. Smart grids optimize the efficiency of EV charging and better the distribution of electrical loads, guaranteeing a seamless charging experience for consumers. GaN-based bi-directional charging with vehicle-to-grid (V2G) technologies enables EVs to serve as energy reservoirs, capable of feeding surplus energy back into the grid. This feature will enhance their sustainability and make them a more environmentally friendly choice in the near future.

ACKNOWLEDGMENTS

The authors would like to thank Ministry of Higher Education Malaysia for funding this project via Higher Education Center of Excellence (HICoE), Institute of Nano Optoelectronics Research and Technology (INOR), with Project No. A305-KR-AKH002-0000000434-K134.

AUTHOR DECLARATIONS

Conflict of Interest

The authors have no conflicts to disclose.

Author Contributions

Kazi Faridur Rahman: Data curation (equal); Formal analysis (equal); Investigation (equal); Methodology (equal); Visualization (equal); Writing – original draft (equal). **Shaili Falina:** Conceptualization (equal); Data curation (equal); Formal analysis (equal); Funding acquisition (equal); Investigation (equal); Methodology (equal); Project administration (equal); Resources (equal); Software (equal); Supervision (equal); Validation (equal); Visualization (equal); Writing – original draft (equal); Writing – review & editing (equal). **Mohamed Fauzi Packeer Mohamed**: Data curation (equal), Validation (supporting); Investigation (supporting); Methodology (supporting); Project administration (supporting); Software (equal). Visualization (supporting). **Hiroshi Kawarada:** Conceptualization (supporting); Validation (supporting); Writing – review & editing (supporting); Supervision (supporting). **Mohd Syamsul:** Conceptualization (equal); Data curation (equal); Formal analysis (equal); Funding acquisition (equal); Investigation (equal); Methodology (equal); Project administration (equal); Resources (equal); Software (equal); Supervision (equal); Validation (equal); Visualization (equal); Writing – original draft (equal); Writing – review & editing (equal).

DATA AVAILABILITY

The data that support the findings of this study are available from the corresponding authors upon reasonable request.

REFERENCES

[1] M. S. Hossain, L. Kumar, M. El Haj Assad, and R. Alayi, "Advancements and future prospects of electric vehicle technologies: A comprehensive review," Complexity **2022**, 1–21.
[2] "The history of the electric car," (Department of Energy, 2023), https://www.energy.gov/articles/history-electric-car, accessed 10 October 2023.
[3] A. Arancibia and K. Strunz, "Modeling of an electric vehicle charging station for fast DC charging," in *2012 IEEE International Electric Vehicle Conference, IEVC 2012* (IEEE, 2012).
[4] N. Karali, *Vehicle-Grid Integration. EV Fast Charging Infrastructure* (Lawrence Berkeley National Laboratory, 2017).
[5] X. Cheng *et al.*, "Electrified vehicles and the smart grid: The ITS perspective," IEEE Trans. Intell. Transp. Syst. **15**(4), 1388–1404 (2014).
[6] N. Lebedeva, F. Di Persio, and L. Boon-Brett, "Lithium ion battery value chain and related opportunities for Europe," Paper No. EUR 28534 EN (2017).
[7] S. Manzetti and F. Mariasiu, "Electric vehicle battery technologies: From present state to future systems," Renewable Sustain. Energy Rev. **51**, 1004–1012 (2015).
[8] M. Naumanen, T. Uusitalo, E. Huttunen-Saarivirta, and R. van der Have, "Development strategies for heavy duty electric battery vehicles: Comparison between China, EU, Japan and USA," Resour. Conserv. Recycl. **151**, 104413 (2019).
[9] J. Du and D. Ouyang, "Progress of Chinese electric vehicles industrialization in 2015: A review," Appl. Energy **188**, 529–546 (2017).
[10] "Global EV Outlook 2019—Analysis," (IEA, 2019), https://www.iea.org/reports/global-ev-outlook-2019, accessed 10 October 2023.
[11] C. F. Calvillo, A. Sánchez-Miralles, and J. Villar, "Energy management and planning in smart cities," Renewable Sustain. Energy Rev. **55**, 273–287 (2016).
[12] "Vehicle types," (US Department of Transportation, 2024), https://www.transportation.gov/rural/ev/toolkit/ev-basics/vehicle-types, accessed 1 February 2024.
[13] M. S. Hossain, L. Kumar, M. M. Islam, and J. Selvaraj, "A comprehensive review on the integration of electric vehicles for sustainable development," J. Adv. Transp. **2022**, 1.
[14] "What is EV, BEV, HEV, PHEV? Here's your guide to types of electric cars," (MarketWatch, 2024), https://www.marketwatch.com/story/what-is-ev-bev-hev-phev-heres-your-guide-to-types-of-electric-cars-11617986782, accessed 1 February 2024.
[15] E. A. M. Falcão, A. C. R. Teixeira, and J. R. Sodré, "Analysis of CO_2 emissions and techno-economic feasibility of an electric commercial vehicle," Appl. Energy **193**, 297–307 (2017).

21 October 2024 08:24:33

© Author(s) 2024

[16]E. D. Kostopoulos, G. C. Spyropoulos, and J. K. Kaldellis, "Real-world study for the optimal charging of electric vehicles," Energy Rep. **6**, 418–426 (2020).
[17]C. Armenta-Deu and T. Coulaud, "Control unit for battery charge management in electric vehicles (EVs)," Future Transp. **4**(2), 429–449 (2024).
[18]"The up! | Models," (Volkswagen UK, 2023), https://www.volkswagen.co.uk/en/new/up.html, accessed 10 October 2023.
[19]"Tesla nears debut of new 400-mile China-made Model 3," (Fortune, 2023), https://fortune.com/2020/04/07/tesla-debut-new-400-mile-china-model-3/, accessed 10 October 2023.
[20]See https://www.best-selling-cars.com/europe/2022-full-year-europe-best-selling-car-manufacturers-and-brands/ for "2022 (Full Year) Europe: Best-Selling Car Manufacturers and Brands," (2023)" (Last accessed 10 October 2023).
[21]"BMW all-electric vehicles," (BMW USA, 2023), https://www.bmwusa.com/all-electric.html/, accessed 10 October 2023.
[22]"Chevrolet Volt: Development story of the pioneering electrified vehicle—Lindsay Brooke," (Google Books, 2023), https://books.google.com.my/books?hl=en&lr=&id=GXd0EAAAQBAJ&oi=fnd&pg=PP1&ots=BFOCh5-ygB&sig=iACFrlkAcpS_Bec5SVsSIakfVKs&redir_esc=y#v=onepage&q&f=false/, accessed 10 October 2023.
[23]A. Heydari and A. Askarzadeh, "Techno-economic analysis of a PV/biomass/fuel cell energy system considering different fuel cell system initial capital costs," Sol. Energy **133**, 409–420 (2016).
[24]"Vehicle electrification—Benefits and technologies," (Honda, 2023), https://automobiles.honda.com/vehicle-electrification?source=https%3a%2f%2fautomobiles.honda.com%2fclarity%3fsource%3dhttps%253a%252f%252fautomobiles.honda.com%252fclarity-electric%26statusCode%3d301&statusCode=301/, accessed 10 October 2023.
[25]"Electric machines and energy storage technologies in EVs," (2023), https://automobiles.honda.com/images/2013/fit-ev/downloads/Automobile_Magazine.pdf/, accessed 10 October 2023.
[26]A. M. Bazzi, Y. Liu, and D. S. Fay, "Electric machines and energy storage: Over a century of technologies in electric and hybrid electric vehicles," IEEE Electrif. Mag. **6**(3), 49–53 (2018).
[27]"Electric car technology," (Kia UK, 2023), https://www.kia.com/uk/electric-hybrid-cars/technology//, accessed 10 October 2023.
[28]F. Nazari, A. Mohammadian, and T. Stephens, "Modeling electric vehicle adoption considering a latent travel pattern construct and charging infrastructure," Transp. Res. D Transp. Environ. **72**, 65–82 (2019).
[29]"All there is to know about Renault Twizy," (Renault Group, 2023), https://www.renaultgroup.com/en/news-on-air/news/all-there-is-to-know-about-renault-twizy//, accessed 10 October 2023.
[30]"New 2017 Renault ZOE ZE 40: 400 km range∗, 41 kWh battery," (2023), https://insideevs.com/news/331773/new-2017-renault-zoe-ze-40-400-km-range-41-kwh-battery//, accessed 10 October 2023.
[31]"Model 3," (Tesla, 2023), https://www.tesla.com/model3/, accessed 10 October 2023.
[32]"Model X," (Tesla, 2023), https://www.tesla.com/modelx/, accessed 10 October 2023.
[33]"2023 Toyota Prius Prime FAQ," (2023), https://www.toyota.com/priusprime/faq//, accessed 10 October 2023.
[34]S. Tanimoto and K. Matsui, "High junction temperature and low parasitic inductance power module technology for compact power conversion systems," IEEE Trans. Electron Devices **62**(2), 258–269 (2015).
[35]H. Wang, A. Hasanzadeh, and A. Khaligh, "Transportation electrification: Conductive charging of electrified vehicles," IEEE Electrif. Mag. **1**(2), 46–58 (2013).
[36]N. Keshmiri, D. Wang, B. Agrawal, R. Hou, and A. Emadi, "Current status and future trends of GaN HEMTs in electrified transportation," IEEE Access **8**, 70553–70571 (2020).
[37]S. Mishra *et al.*, "A comprehensive review on developments in electric vehicle charging station infrastructure and present scenario of India," Sustainability **13**(4), 2396 (2021).
[38]T. Zhang *et al.*, "Status and development of electric vehicle integrated thermal management from BTM to HVAC," Appl. Therm. Eng. **88**, 398–409 (2015).
[39]S. Hemavathi and A. Shinisha, "A study on trends and developments in electric vehicle charging technologies," J. Energy Storage **52**, 105013 (2022).
[40]A. Ahmad, Z. A. Khan, M. Saad Alam, and S. Khateeb, "A review of the electric vehicle charging techniques, standards, progression and evolution of EV technologies in Germany," Smart Sci. **6**(1), 36–53 (2018).
[41]F. Un-Noor, S. Padmanaban, L. Mihet-Popa, M. Mollah, and E. Hossain, "A comprehensive study of key electric vehicle (EV) components, technologies, challenges, impacts, and future direction of development," Energies (Basel) **10**(8), 1217 (2017).
[42]"Gallium nitride future of EV chips," (2023), https://www.sae.org/news/2021/04/gallium-nitride-future-of-ev-chips, accessed 10 October 2023.
[43]H. Qin *et al.*, "Influence of pressure on the mechanical and electronic properties of wurtzite and zinc-blende GaN crystals," Crystals (Basel) **8**(11), 428 (2018).
[44]M. Meneghini *et al.*, "GaN-based power devices: Physics, reliability, and perspectives," J. Appl. Phys. **130**(18), 181101 (2021).
[45]T. Yang *et al.*, "An integrated liquid metal thermal switch for active thermal management of electronics," IEEE Trans. Compon. Packaging Manuf. Technol. **9**(12), 2341–2351 (2019).
[46]S. Li *et al.*, "Reliability concern of 650-V normally-off GaN devices under reverse freewheeling stress," IEEE Trans. Electron Devices **67**(8), 3492–3495 (2020).
[47]C. Yu, E. Laboure, and C. Buttay, "Thermal management of lateral GaN power devices," in *IEEE International Workshop on Integrated Power Packaging, IWIPP 2015* (IEEE, 2015), pp. 40–43.
[48]M. F. Fatahilah, K. Strempel, F. Yu, S. Vodapally, A. Waag, and H. S. Wasisto, "3D GaN nanoarchitecture for field-effect transistors," Micro Nano Eng. **3**, 59–81 (2019).
[49]W. Saito, Y. Takada, M. Kuraguchi, K. Tsuda, and I. Omura, "Recessed-gate structure approach toward normally off high-voltage AlGaN/GaN HEMT for power electronics applications," IEEE Trans. Electron Devices **53**(2), 356–362 (2006).
[50]C. Langpoklakpam, A.-C. Liu, Y.-K. Hsiao, C.-H. Lin, and H.-C. Kuo, "Vertical GaN MOSFET power devices," Micromachines (Basel) **14**(10), 1937 (2023).
[51]N. Ikeda *et al.*, "GaN power transistors on Si substrates for switching applications," Proc. IEEE **98**(7), 1151–1161 (2010).
[52]H. Otake, K. Chikamatsu, A. Yamaguchi, T. Fujishima, and H. Ohta, "Vertical GaN-based trench gate metal oxide semiconductor field-effect transistors on GaN bulk substrates," Appl. Phys. Express **1**(1), 011105 (2008).
[53]Y. Gao, I. Ben-Yaacov, U. K. Mishra, and E. L. Hu, "Optimization of AlGaN/GaN current aperture vertical electron transistor (CAVET) fabricated by photoelectrochemical wet etching," J. Appl. Phys. **96**(11), 6925–6927 (2004).
[54]M. Kanechika *et al.*, "A vertical insulated gate AlGaN/GaN heterojunction field-effect transistor," Jpn. J. Appl. Phys. **46**(6L), L503 (2007).
[55]W. B. Lanford, T. Tanaka, Y. Otoki, and I. Adesida, "Recessed-gate enhancement-mode GaN HEMT with high threshold voltage," Electron Lett. **41**(7), 449 (2005).
[56]B. Lu, O. I. Saadat, and T. Palacios, "High-performance integrated dual-gate AlGaN/GaN enhancement-mode transistor," IEEE Electron Device Lett. **31**(9), 990–992 (2010).
[57]B. Lu, E. Matioli, and T. Palacios, "Tri-gate normally-off GaN power MISFET," IEEE Electron Device Lett. **33**(3), 360–362 (2012).
[58]K. Ota, K. Endo, Y. Okamoto, Y. Ando, H. Miyamoto, and H. Shimawaki, "A normally-off GaN FET with high threshold voltage uniformity using a novel piezo neutralization technique," in *2009 IEEE International Electron Devices Meeting (IEDM)* (IEEE, 2009), pp. 1–4.
[59]Y. Uemoto *et al.*, "Gate injection transistor (GIT)—A normally-off AlGaN/GaN power transistor using conductivity modulation," IEEE Trans. Electron Devices **54**(12), 3393–3399 (2007).
[60]T. Mizutani, M. Ito, S. Kishimoto, and F. Nakamura, "AlGaN/GaN HEMTs with thin InGaN cap layer for normally off operation," IEEE Electron Device Lett. **28**(7), 549–551 (2007).
[61]M. Okada *et al.*, "Novel vertical heterojunction field-effect transistors with regrown AlGaN/GaN two-dimensional electron gas channels on GaN substrates," Appl. Phys. Express **3**(5), 054201 (2010).
[62]G. Rajendran, C. A. Vaithilingam, N. Misron, K. Naidu, and M. R. Ahmed, "A comprehensive review on system architecture and international standards for electric vehicle charging stations," J. Energy Storage **42**, 103099 (2021).

21 October 2024 08:24:33

© Author(s) 2024

[63]Y. Yusuf *et al.*, "Two-step GaN layer growth for high-voltage lateral AlGaN/GaN HEMT," Crystals (Basel) **13**(1), 90 (2023).
[64]F. Medjdoub, J. F. Carlin, C. Gaquiere, N. Grandjean, and E. Kohn, "Status of the emerging InAlN/GaN power HEMT technology," Open Electr. Electron. Eng. J. **2**(1), 1–7 (2008).
[65]B. Hult, M. Thorsell, J.-T. Chen, and N. Rorsman, "High voltage and low leakage GaN-on-SiC MISHEMTs on a 'buffer-free' heterostructure," IEEE Electron Device Lett. **43**(5), 781–784 (2022).
[66]B. J. Baliga, "Gallium nitride devices for power electronic applications," Semicond. Sci. Technol. **28**(7), 074011 (2013).
[67]B. Hult, M. Thorsell, J.-T. Chen, and N. Rorsman, "AlGaN/GaN/AlN 'buffer-free' high voltage MISHEMTs with Si-rich and stoichiometric SiN_x first passivation," in *2022 Compound Semiconductor Week (CSW)* (IEEE, 2022).
[68]Y. Li, S. Huang, X. Wang, Q. Jiang, and X. Liu, "Investigation of ON-state breakdown mechanism in AlGaN/GaN HEMTs with AlGaN back barrier," Electron (Basel) **11**(9), 1331 (2022).
[69]W.-C. Ho *et al.*, "The Study of high breakdown voltage vertical GaN-on-GaN p-i-n diode with modified mesa structure," Crystals (Basel) **10**(8), 712 (2020).
[70]M. Okada, M. Uneno, M. Kiyama, and K. Sumiyoshi, "Low on-resistance high breakdown voltage GaN diodes on low dislocation density GaN substrates," SEI Technical Paper No. 77 (2013).
[71]A. Asgari and M. Kalafi, "The control of two-dimensional-electron-gas density and mobility in AlGaN/GaN heterostructures with Schottky gate," Mater. Sci. Eng. C **26**(5), 898–901 (2006).
[72]T. Fujishima, H. Otake, and H. Ohta, "Reduction in threshold voltages in GaN-based metal oxide semiconductor field effect transistors," Appl. Phys. Lett. **92**(24), 243505 (2008).
[73]Y. Zhong *et al.*, "A review on the GaN-on-Si power electronic devices," Fundam. Res. **2**(3), 462–475 (2022).
[74]M. Rodriguez, Y. Zhang, and D. Maksimovic, "High-frequency PWM buck converters using GaN-on-SiC HEMTs," IEEE Trans. Power Electron. **29**(5), 2462–2473 (2014).
[75]T. Ueda, M. Ishida, T. Tanaka, and D. Ueda, "GaN transistors on Si for switching and high-frequency applications," Jpn. J. Appl. Phys. **53**(10), 100214 (2014).
[76]S. Huang, W. Liao, P. Liu, W. Tang, and S. Huang, "Analysis and calculation on switching frequency and switching losses of modular multilevel converter with maximum sub-module capacitor voltage deviation," IET Power Electron. **9**(2), 188–197 (2016).
[77]H. Lu *et al.*, "A review of GaN RF devices and power amplifiers for 5G communication applications," Fundam. Res. (published online) (2023).
[78]C. Caruana, "Power converters for renewable energy: Solar," in *Encyclopedia of Electrical and Electronic Power Engineering* (Elsevier, 2023), pp. 168–183.
[79]O. F. Goksu, E. B. Bulut, M. O. Gulbahce, and S. Dusmez, "Thermal design and performance evaluation of GaN power stage in a 4-level totem-pole PFC," AEU – Int. J. Electron. Commun. **173**, 154981 (2024).
[80]D. Han, A. Ogale, S. Li, Y. Li, and B. Sarlioglu, "Efficiency characterization and thermal study of GaN based 1 kW inverter," in *2014 IEEE Applied Power Electronics Conference and Exposition—APEC 2014* (IEEE, 2014), pp. 2344–2350.
[81]A. Ahmed, M. A. Khan, M. Badawy, Y. Sozer, and I. Husain, "Performance analysis of bi-directional DC-DC converters for electric vehicles and charging infrastructure," in *2013 IEEE Energy Conversion Congress and Exposition, ECCE 2013* (IEEE, 2013), pp. 1401–1408.
[82]M. A. Khan, A. Ahmed, I. Husain, Y. Sozer, and M. Badawy, "Performance analysis of bidirectional DC-DC converters for electric vehicles," IEEE Trans. Ind. Appl. **51**(4), 3442–3452 (2015).
[83]C. Jiang, R. Torquato, D. Salles, and W. Xu, "Method to assess the power-quality impact of plug-in electric vehicles," IEEE Trans. Power Delivery **29**(2), 958–965 (2014).
[84]G. Roh, H. Kim, H. Jeon, and K. Yoon, "Fuel consumption and CO_2 emission reductions of ships powered by a fuel-cell-based hybrid power source," J. Mar. Sci. Eng. **7**(7), 230 (2019).
[85]R. Ahmed, M. E. Sayed, I. Arasaratnam, J. Tjong, and S. Habibi, "Reduced-order electrochemical model parameters identification and SOC estimation for healthy and aged Li-ion batteries. Part II: Aged battery model and state of charge estimation," IEEE J. Emerg. Sel. Top. Power Electron. **2**(3), 678–690 (2014).
[86]K. Shenai, M. Dudley, R. F. Davis, M. Su, C. Chen, and S. Rajan, "Prospects for the application of GaN power devices in hybrid electric vehicle drive systems," Semicond. Sci. Technol. **28**(7), 074012 (2013).
[87]M. Kazanbas, M. Wendt, T. Kleeb, P. Zacharia, and S. Araujo, "Prospects of GaN devices in automotive electrification," in *PCIM Europe 2014: International Exhibition and Conference for Power Electronics, Intelligent Motion, Renewable Energy and Energy Management* (VDE, Nuremberg, 2014), pp. 1–8.
[88]A. Avila, M. Lucu, A. Garcia-Bediaga, U. Ibarguren, I. Gandiaga, and A. Rujas, "Hybrid energy storage system based on Li-ion and Li-S battery modules and GaN-based DC-DC converter," IEEE Access **9**, 132342–132353 (2021).
[89]A. Eial Awwad, "Analysis, design, and experimental results for a high-frequency ZVZCS galvanically isolated PSFB DC-DC converter over a wide operating range using GaN-HEMT," World Electric Veh. J. **13**(11), 206 (2022).
[90]J.-G. Yoo, D.-M. Joo, H.-B. Kim, and J.-S. Kim, "Implementation of a phase shift full-bridge converter for LDC using GaN HEMT," in *2017 20th International Conference on Electrical Machines and Systems (ICEMS)* (IEEE, 2017), pp. 1–5.
[91]K. Shi *et al.*, "Design and optimization of a current-driven phase-shift full-bridge converter with GaN devices and large conversion ratio," in *2020 IEEE 3rd International Conference on Electronics Technology, ICET 2020* (Institute of Electrical and Electronics Engineers Inc., 2020), pp. 324–329.
[92]F. Xue, R. Yu, and A. Q. Huang, "A 98.3% efficient GaN isolated bidirectional DC-DC converter for DC microgrid energy storage system applications," IEEE Trans. Ind. Electron. **64**(11), 9094–9103 (2017).
[93]A. F. Bakan, N. Altintaş, and I. Aksoy, "An improved PSFB PWM DC-DC converter for high-power and frequency applications," IEEE Trans. Power Electron. **28**(1), 64–74 (2013).
[94]M. Escudero *et al.*, "A practical approach to the design of a highly efficient PSFB DC-DC converter for server applications," Energies **12**(19), 3723 (2019).
[95]H. Nene and T. Zaitsu, "Bi-directional PSFB DC-DC converter with unique PWM control schemes and seamless mode transitions using enhanced digital control," in *IEEE Applied Power Electronics Conference and Exposition—APEC* (IEEE, 2017), pp. 3229–3233.
[96]M. Escudero, M. A. Kutschak, D. Meneses, D. P. Morales, and N. Rodriguez, "Synchronous rectifiers drain voltage overshoot reduction in PSFB converters," IEEE Trans. Power Electron. **35**(7), 7419–7433 (2020).
[97]G. Di Capua, S. A. Shirsavar, M. A. Hallworth, and N. Femia, "An enhanced model for small-signal analysis of the phase-shifted full-bridge converter," IEEE Trans. Power Electron. **30**(3), 1567–1576 (2015).
[98]S. Inoue and H. Akagi, "A bidirectional DC-DC converter for an energy storage system with galvanic isolation," IEEE Trans. Power Electron. **22**(6), 2299–2306 (2007).
[99]C. Mi, H. Bai, C. Wang, and S. Gargies, "Operation, design and control of dual H-bridge-based isolated bidirectional DC-DC converter," IET Power Electron. **1**(4), 507–5017 (2008).
[100]D. Costinett, D. Maksimovic, and R. Zane, "Design and control for high efficiency in high step-down dual active bridge converters operating at high switching frequency," IEEE Trans. Power Electron. **28**(8), 3931–3940 (2013).
[101]F. Krismer and J. W. Kolar, "Closed form solution for minimum conduction loss modulation of DAB converters," IEEE Trans. Power Electron. **27**(1), 174–188 (2012).
[102]F. Krismer and J. W. Kolar, "Efficiency-optimized high-current dual active bridge converter for automotive applications," IEEE Trans. Ind. Electron. **59**(7), 2745–2760 (2012).
[103]H. Zhou and A. M. Khambadkone, "Hybrid modulation for dual active bridge bi-directional converter with extended power range for ultracapacitor application," in *Conference Record—IAS Annual Meeting* (IEEE Industry Applications Society, 2008).
[104]G. Ortiz, J. Biela, D. Bortis, and J. W. Kolar, "1 Megawatt, 20 kHz, isolated, bidirectional 12 kV to 1.2 kV DC-DC converter for renewable energy applications," in *2010 International Power Electronics Conference—ECCE Asia, IPEC 2010* (IEEE, 2010), pp. 3212–3219.

21 October 2024 08:24:33

© Author(s) 2024

[105]U. Mustafa, R. Ahmed, A. Watson, P. Wheeler, N. Ahmed, and P. Dahele, "A comprehensive review of machine-integrated electric vehicle chargers," Energies **16**(1), 129 (2022).
[106]Y. C. Liu, C. Chen, K. De Chen, Y. L. Syu, and M. C. Tsai, "High-frequency LLC resonant converter with GaN devices and integrated magnetics," Energies (Basel) **12**(9), 1781 (2019).
[107]M. Faizan, X. Wang, and M. Z. Yousaf, "Design and comparative analysis of an ultra-highly efficient, compact half-bridge LLC resonant GaN converter for low-power applications," Electron (Switzerland) **12**(13), 2850 (2023).
[108]B. Sun, R. Burgos, D. Boroyevich, S. Bala, and J. Xu, "10 kW high efficiency compact GaN-based DC/DC converter design," in *2018 IEEE Energy Conversion Congress and Exposition (ECCE)* (IEEE, 2018), pp. 6307–6313.
[109]M. D. Seeman, S. R. Bahl, D. I. Anderson, and G. A. Shah, "Advantages of GaN in a high-voltage resonant LLC converter," in *2014 IEEE Applied Power Electronics Conference and Exposition—APEC 2014* (IEEE, 2014), pp. 476–483.
[110]A. M. Ammar, K. Ali, and D. J. Rogers, "A bidirectional GaN-based CLLC converter for plug-in electric vehicles on-board chargers," in *IECON 2020: The 46th Annual Conference of the IEEE Industrial Electronics Society* (IEEE, 2020), pp. 1129–1135.
[111]H. N. Vu, M. Abdel-Monem, M. El Baghdadi, J. Van Mierlo, and O. Hegazy, "Multi-objective optimization of on-board chargers based on state-of-the-art 650V GaN power transistors for the application of electric vehicles," in *2019 IEEE Vehicle Power and Propulsion Conference, VPPC 2019* (IEEE, 2019).
[112]H. Watanabe, J. I. Itoh, N. Koike, and S. Nagai, "PV micro-inverter topology using LLC resonant converter," Energies **12**(16), 3106 (2019).
[113]E. Çalışkan and O. Ustun, "Smart efficiency tracking for novel switch—LLC converter for battery charging applications," Energies **15**(5), 1861 (2022).
[114]S. Zhao, A. Kempitiya, W. T. Chou, V. Palija, and C. Bonfiglio, "Variable DC-link voltage LLC resonant DC/DC converter with wide bandgap power devices," IEEE Trans. Ind. Appl. **58**(3), 2965–2977 (2022).
[115]S. A. Mortazavizadeh *et al.*, "High frequency, high efficiency, and high power density GaN-based LLC resonant converter: State-of-the-art and perspectives," Appl. Sci. **11**(23), 11350 (2021).
[116]Z. U. Zahid, Z. M. Dalala, R. Chen, B. Chen, and J. S. Lai, "Design of bidirectional DC-DC resonant converter for Vehicle-to-Grid (V2G) applications," IEEE Trans. Transp. Electrif. **1**(3), 232–244 (2015).
[117]J. H. Jung, H. S. Kim, M. H. Ryu, and J. W. Baek, "Design methodology of bidirectional CLLC resonant converter for high-frequency isolation of DC distribution systems," IEEE Trans. Power Electron. **28**(4), 1741–1755 (2013).
[118]M. Hoshi, "Electric vehicles and expectations for wide bandgap power devices," in *Proceedings of the International Symposium on Power Semiconductor Devices and Ics* (IEEE, 2016), pp. 5–8.
[119]Y. Zhang and M. A. De Rooij, "How eGaN® FETs are enabling large area wireless power transfer," in *2017 IEEE 5th Workshop on Wide Bandgap Power Devices and Applications, WiPDA 2017* (IEEE, 2017), pp. 366–372.
[120]Y. Yang, Y. Liu, Y. Zhao, J. Liu, and B. Zhu, "High frequency and high power density bipolar DC–DC converter with GaN HEMT," Energy Rep. **9**, 617–624 (2023).
[121]T. M. Rezk, G. A. Fahmy, S. A. Ibrahim, and H. F. Ragai, "Design of a differential power oscillator for 433 MHz WPT using e-GaN HEMTs," Ain Shams Eng. J. **13**(3), 101581 (2022).
[122]B. A. Obaid, A. L. Saleh, and A. K. Kadhim, "Resolving of optimal fractional PID controller for DC motor drive based on anti-windup by invasive weed optimization technique," Indo. J. Electr. Eng. Comput. Sci. **15**(1), 95–103 (2019).
[123]S. Z. Mohammad Noor, A. M. Omar, N. N. Mahzan, and I. R. Ibrahim, "A review of single-phase single stage inverter topologies for photovoltaic system," in *2013 IEEE 4th Control and System Graduate Research Colloquium* (IEEE, 2013), pp. 69–74.
[124]M. D. Bellar *et al.*, *A Review of Soft-Switched DC-AC Converters* (IEEE, 1998).
[125]Y. Xia, J. Roy, and R. Ayyanar, "GaN-based split phase transformer-less PV inverter with auxiliary ZVT circuit," IET Power Electron. **13**(3), 525–534 (2020).
[126]M. Valente, F. Iannuzzo, Y. Yang, and E. Gurpinar, "Performance analysis of a single-phase GaN-based 3L-ANPC inverter for photovoltaic applications," in *2018 IEEE 4th Southern Power Electronics Conference, SPEC 2018* (Institute of Electrical and Electronics Engineers Inc., 2018).
[127]E. Gurpinar and A. Castellazzi, "Tradeoff study of heat sink and output filter volume in a GaN HEMT based single-phase inverter," IEEE Trans. Power Electron. **33**(6), 5226–5239 (2018).
[128]T. Liu, C. Chen, K. Xu, Y. Zhang, and Y. Kang, "GaN-based megahertz single-phase inverter with a hybrid TCM control method for high efficiency and high-power density," IEEE Trans. Power Electron. **36**(6), 6797–6813 (2021).
[129]M. T. Elrais and I. Batarseh, "Design and experimental study of a GaN-based three-port multilevel inverter," in *IECON 2021—47th Annual Conference of the IEEE Industrial Electronics Society* (IEEE, 2021), pp. 1–6.
[130]T. Morita *et al.*, "99.3% Efficiency of three-phase inverter for motor drive using GaN-based gate injection transistors," in *IEEE Applied Power Electronics Conference and Exposition—APEC* (IEEE, 2011), pp. 481–484.
[131]J. Colmenares, D. Peftitsis, G. Tolstoy, D. Sadik, H. P. Nee, and J. Rabkowski, "High-efficiency three-phase inverter with SiC MOSFET power modules for motor-drive applications," in *2014 IEEE Energy Conversion Congress and Exposition, ECCE 2014* (IEEE, 2014), pp. 468–474.
[132]I. Takahashi, G. Su, T. Koganezawa, and K. Ohyama, "A super high speed PM motor drive system by a quasi current source inverter," IEEE Trans. Ind. Appl. **30**(3), 683–690 (1994).
[133]K. Shirabe *et al.*, "Advantages of high frequency PWM in AC motor drive applications," in *2012 IEEE Energy Conversion Congress and Exposition, ECCE 2012* (IEEE, 2012), pp. 2977–2984.
[134]H. Liu, Z. Gao, W. Wu, L. Chow, and T. Wu, "Design of a high-efficiency permanent magnet synchronous motor and inverter system," in *IECON 2015—41st Annual Conference of the IEEE Industrial Electronics Society* (IEEE, 2015), pp. 4996–5001.
[135]"GaN motor drives for consumer electronics & personal robotics," (EPC, 2024), https://epc-co.com/epc/markets/consumer-electronics/motor-drive, accessed 13 June 2024.
[136]"Industrial motor drive," (Navitas, 2024), https://navitassemi.com/industrial-motor-drive/, accessed 13 June 2024.
[137]"Automotive—Electric vehicle main DC-DC converter," (Skyworks, 2023), https://www.skyworksinc.com/en/Application-Pages/Automotive-EV-Main-DC-DC-Converter, accessed 6 December 2023.
[138]N. Keshmiri, M. I. Hassan, R. Rodriguez, and A. Emadi, "Comparison of isolated bidirectional DC/DC converters using WBG devices for more electric aircraft," IEEE Open J. Ind. Electron. Soc. **2**, 184–198 (2021).
[139]"12V 24V 48V 72V DC converters to use in 144 volt, 196 volt, 240 volt, 288 volt, 320 volt electric cars, including waterproof," (2023), https://www.powerstream.com/electric-car-12V-DCDC-converters.htm, accessed 6 December 2023.
[140]Z. Waradzyn, R. Stala, A. Mondzik, A. Skała, and A. Penczek, "GaN-based DC-DC resonant boost converter with very high efficiency and voltage gain control," Energies (Basel) **13**(23), 6403 (2020).
[141]R. P. Narasipuram and S. Mopidevi, "A novel hybrid control strategy and dynamic performance enhancement of a 3.3 kW GaN–HEMT-based iL2C resonant full-bridge DC–DC power converter methodology for electric vehicle charging systems," Energies (Basel) **16**(15), 5811 (2023).
[142]N. Kondrath, "Design and evaluation of a novel hybrid SiC-GaN based bidirectional full-bridge DC-DC converter," Paper No. 2017-01-2032 (2017).
[143]A. Jafari, M. Samizadeh Nikoo, F. Karakaya, and E. Matioli, "Enhanced-DAB converter: Comprehensive design evaluation," in *2020 IEEE 9th International Power Electronics and Motion Control Conference (IPEMC2020-ECCE Asia)* (IEEE, 2020), pp. 1844–1851.
[144]M. Vasic, D. Serrano, V. Toral, P. Alou, J. A. Oliver, and J. A. Cobos, "Ultraefficient voltage doubler based on a GaN resonant switched-capacitor converter," IEEE J. Emerg. Sel. Top. Power Electron. **7**(2), 622–635 (2019).
[145]D. Reusch and J. Strydom, "Evaluation of gallium nitride transistors in high frequency resonant and soft-switching DC–DC converters," IEEE Trans. Power Electron. **30**(9), 5151–5158 (2015).
[146]S. Li, Y. Zheng, B. Wu, and K. M. Smedley, "A family of resonant two-switch boosting switched-capacitor converter with ZVS operation and a wide line regulation range," IEEE Trans. Power Electron. **33**(1), 448–459 (2018).
[147]A. Kawa and R. Stala, "SiC-based bidirectional multilevel high-voltage gain switched-capacitor resonant converter with improved efficiency," Energies (Basel) **13**(10), 2445 (2020).

21 October 2024 08:24:33

© Author(s) 2024

[148]H. Setiadi and H. Fujita, "Reduction of switching power losses for ZVS operation in switched-capacitor-based resonant converters," IEEE Trans. Power Electron. **36**(1), 1104–1115 (2021).
[149]W. Xie, B. Y. Brown, and K. M. Smedley, "Multilevel step-down resonant switched-capacitor converters with full-range regulation," IEEE Trans. Ind. Electron. **68**(10), 9481–9492 (2021).
[150]A. Panday and H. O. Bansal, "Energy management strategy for hybrid electric vehicles using genetic algorithm," J. Renewable Sustain. Energy **8**(1), 015701 (2016).
[151]A. Geetha and C. Subramani, "A comprehensive review on energy management strategies of hybrid energy storage system for electric vehicles," Int. J. Energy Res. **41**(13), 1817–1834 (2017).
[152]J. Hoelzen *et al.*, "Conceptual design of operation strategies for hybrid electric aircraft," Energies (Basel) **11**(1), 217 (2018).
[153]J. D. Widmer, R. Martin, and M. Kimiabeigi, "Electric vehicle traction motors without rare earth magnets," Sustain. Mater. Technol. **3**, 7–13 (2015).
[154]A. Krings, A. Boglietti, A. Cavagnino, and S. Sprague, "Soft magnetic material status and trends in electric machines," IEEE Trans. Ind. Electron. **64**(3), 2405–2414 (2017).
[155]R. D. Falck, J. C. Chin, S. L. Schnulo, J. M. Burt, and J. S. Gray, "Trajectory optimization of electric aircraft subject to subsystem thermal constraints," in *18th AIAA/ISSMO Multidisciplinary Analysis and Optimization Conference* (AIAA, 2017).
[156]N. K. Borer *et al.*, "Design and performance of the NASA SCEPTOR distributed electric propulsion flight demonstrator," Paper No. AIAA 2016-3920 (2016).
[157]K. A. Deere, J. K. Viken, S. A. Viken, M. B. Carter, M. R. Wiese, and N. Farr, "Computational analysis of a wing designed for the X-57 distributed electric propulsion aircraft," Paper No. AIAA 2016-3923 (2017).
[158]K. C. Reinhardt and M. A. Marciniak, "Wide-bandgap power electronics for the more electric aircraft," in "*Proceedings of the Intersociety Energy Conversion Engineering Conference* (IEEE, 1996), Vol. 1, pp. 127–132.
[159]"Gallium nitride applications," (2023), https://www.theiet.org/publishing/inspec/researching-hot-topics/gallium-nitride-applications/?utm_source=redirect&utm_medium=legacyredirects&utm_campaign=2019relaunch, accessed 8 November 2023.
[160]J. Na *et al.*, "2.4 GHz GaN HEMT class-F synchronous rectifier using an independent second harmonic tuning circuit," Sensors **21**(5), 1–9 (2021).
[161]M. A. Hoque, S. N. Ali, M. A. Mokri, S. Gopal, M. Chahardori, and D. Heo, "A highly efficient dual-band harmonic-tuned GaN RF synchronous rectifier with integrated coupler and phase shifter," in *2019 IEEE MTT-S International Microwave Symposium (IMS)* (IEEE, 2019), pp. 1320–1323.
[162]Y. Liu, X. Huang, Y. Dou, Z. Ouyang, and M. Andersen, "GaN-based ZVS bridgeless dual-SEPIC PFC rectifier with integrated inductors," IEEE Trans. Power Electron. **36**(10), 11483–11498 (2021).
[163]S. Abbasian and T. Johnson, "High efficiency GaN HEMT class-F synchronous rectifier for wireless applications," IEICE Electron. Express **12**(1), 20140952 (2015).
[164]S. Abbasian and T. Johnson, "High efficiency GaN HEMT synchronous rectifier with an octave bandwidth for wireless power applications," in *2016 IEEE MTT-S International Microwave Symposium (IMS)* (IEEE, 2016), pp. 1–4.
[165]S. N. Ali, T. Johnson, and D. Heo, "DC polarity control in radio frequency synchronous rectifier circuits," IEEE Microwave Wireless Compon. Lett. **27**(12), 1107–1109 (2017).
[166]S. Aldhaher, D. C. Yates, and P. D. Mitcheson, "Load-independent class E/EF inverters and rectifiers for MHz-switching applications," IEEE Trans. Power Electron. **33**(10), 8270–8287 (2018).
[167]Y. Guan, Y. Wang, W. Wang, and D. Xu, "Analysis and design of a high-frequency DC/DC converter based on a resonant rectifier," IEEE Trans. Ind. Electron. **64**(11), 8492–8503 (2017).
[168]H. Moradisizkoohi, N. Elsayad, and O. Mohammed, "A soft-switched DC/DC converter using integrated dual half-bridge with high voltage gain and low voltage stress for DC microgrid applications," Inventions **3**(3), 63 (2018).
[169]J. Nagao, J. Furuta, and K. Kobayashi, "Capacitor-based three-level gate driver for GaN HEMT only with a single voltage supply," in *2020 IEEE 21st Workshop on Control and Modeling for Power Electronics, COMPEL 2020* (Institute of Electrical and Electronics Engineers Inc., 2020).
[170]T. Takahashi, J. Nagao, J. Furuta, and K. Kobayashi, "A capacitor-based multilevel gate driver for GaN HEMT only with a single voltage supply," in *2021 IEEE 8th Workshop on Wide Bandgap Power Devices and Applications, WiPDA 2021* (IEEE, 2021), pp. 158–163.
[171]C. Hsia and D.-F. Lu, "GaN-on-Si: Monolithically integrated all-GaN drivers for high-voltage DC-DC power conversion," Appl. Sci. **12**(10), 5109 (2022).
[172]C. B. Barth *et al.*, "Design and control of a GaN-based, 13-level, flying capacitor multilevel inverter," IEEE J. Emerg. Sel. Top. Power Electron. **8**(3), 2179–2191 (2020).
[173]M. Kaufmann, M. Lueders, C. Kaya, and B. Wicht, "18.2 A monolithic E-mode GaN 15W 400V offline self-supplied hysteretic buck converter with 95.6% efficiency," in *2020 IEEE International Solid- State Circuits Conference (ISSCC)* (IEEE, 2020), pp. 288–290.
[174]S. Noike, J. Nagao, J. Furuta, and K. Kobayashi, "An asynchronous buck converter by using a monolithic GaN IC integrated by an enhancement-mode GaN-on-SOI process," in *2021 IEEE 8th Workshop on Wide Bandgap Power Devices and Applications (WiPDA)* (IEEE, 2021), pp. 215–219.
[175]I. Telliez *et al.*, *95% Efficiency, 10MHz Switching Rate and 30W, Fully Integrated Buck Converters Using E/D-Mode GaN HEMTs* (Defense Technical Information Center, Fort Belvoir, VA, 2019), pp. 501–505.
[176]S. Biswas, D. Reusch, and M. de Rooij, "Design of GaN-based multilevel switched capacitor converters—Benefits and challenges," IEEE Trans. Ind. Appl. **56**(2), 979–988 (2020).
[177]T. Modeer, N. Pallo, T. Foulkes, C. B. Barth, and R. C. N. Pilawa-Podgurski, "Design of a GaN-based interleaved nine-level flying capacitor multilevel inverter for electric aircraft applications," IEEE Trans. Power Electron. **35**(11), 12153–12165 (2020).
[178]J. Feng, W. Q. Chu, Z. Zhang, and Z. Q. Zhu, "Power electronic transformer-based railway traction systems: Challenges and opportunities," IEEE J. Emerg. Sel. Top. Power Electron. **5**(3), 1237–1253 (2017).
[179]D. Ronanki, S. A. Singh, and S. S. Williamson, "Comprehensive topological overview of rolling stock architectures and recent trends in electric railway traction systems," IEEE Trans. Transp. Electrif. **3**(3), 724–738 (2017).
[180]B. Fesmire, "The future of transport is electric, and it's already here," Policy Magazine (2014).
[181]S. Dusmez and A. Khaligh, "Cost effective solutions to level 3 on-board battery chargers," in *IEEE Applied Power Electronics Conference and Exposition—APEC* (IEEE, 2012), pp. 2121–2127.
[182]A. Alemanno, R. Morici, M. Pretelli, and C. Florian, "Design of a 7.5 kW dual active bridge converter in 650 V GaN technology for charging applications," Electron (Basel) **12**(6), 1280 (2023).
[183]F. Karakaya, Ö. Gülsuna, and O. Keysan, "Feasibility of quasi-square-wave zero-voltage-switching bi-directional DC/DC converters with GaN HEMTs," Energies (Basel) **14**(10), 2867 (2021).
[184]H.-N. Vu, M. Abdel-Monem, M. El Baghdadi, J. Van Mierlo, and O. Hegazy, "Multi-objective optimization of on-board chargers based on state-of-the-art 650V GaN power transistors for the application of electric vehicles," in *2019 IEEE Vehicle Power and Propulsion Conference (VPPC)* (IEEE, 2019), pp. 1–6.
[185]H. Bai, M. McAmmond, J. Lu, Q. Tian, H. Teng, and A. Brown, "Design and optimization of a 98%-efficiency on-board level-2 battery charger using E-mode GaN HEMTs for electric vehicles," SAE Int. J. Altern. Powertrains **5**(1), 205–213 (2016).
[186]S.-S. Yang, S.-S. Min, C.-H. Eom, R.-Y. Kim, and G.-Y. Lee, "Design method of vertical lattice loop structure for parasitic inductance reduction in a GaN HEMTs-based converter," IEEE Access **10**, 117215–117224 (2022).
[187]Y. Jang, M. M. Jovanovic, J. M. Ruiz, M. Kumar, and G. Liu, "Implementation of 3.3-kW GaN-based DC-DC converter for EV on-board charger with series-resonant converter that employs combination of variable-frequency and delay-time control," in *2016 IEEE Applied Power Electronics Conference and Exposition (APEC)* (IEEE, 2016), pp. 1292–1299.
[188]G.-J. Su, C. White, and Z. Liang, "Design and evaluation of a 6.6 kW GaN converter for onboard charger applications," in *2017 IEEE 18th Workshop on Control and Modeling for Power Electronics (COMPEL)* (IEEE, 2017), pp. 1–6.
[189]J. Lu, Q. Tian, K. Bai, A. Brown, and M. McAmmond, "An indirect matrix converter based 97%-efficiency on-board level 2 battery charger using E-mode GaN HEMTs," in *2015 IEEE 3rd Workshop on Wide Bandgap Power Devices and Applications (WiPDA)* (IEEE, 2015), pp. 351–358.

21 October 2024 08:24:33

© Author(s) 2024

[190]B. Li, F. C. Lee, Q. Li, and Z. Liu, "Bi-directional on-board charger architecture and control for achieving ultra-high efficiency with wide battery voltage range," in *2017 IEEE Applied Power Electronics Conference and Exposition (APEC)* (IEEE, 2017), pp. 3688–3694.
[191]P. B. Backlund, C. C. Seepersad, and T. M. Kiehne, "All-electric ship energy system design using classifier-guided sampling," IEEE Trans. Transp. Electrif. **1**(1), 77–85 (2015).
[192]D. Gao, X. Wang, T. Wang, Y. Wang, and X. Xu, "An energy optimization strategy for hybrid power ships under load uncertainty based on load power prediction and improved NSGA-II Algorithm," Energies (Basel) **11**(7), 1699 (2018).
[193]C. Martos-Contreras, J. Cruz-Cozar, A. Medina-Garcia, N. Rodriguez, and D. P. Morales, "Experimental comparison of planar transformer architectures for half-bridge resonant topology," AEU – Int. J. Electron. Commun. **174**, 155056 (2024).
[194]K. Alluhaybi, I. Batarseh, and H. Hu, "Comprehensive review and comparison of single-phase grid-tied photovoltaic microinverters," IEEE J. Emerg. Sel. Top. Power Electron. **8**(2), 1310–1329 (2020).
[195]B. Dwiza and J. Kalaiselvi, "Analytical approach for common mode EMI noise analysis in dual active bridge converter," in *IECON 2020: The 46th Annual Conference of the IEEE Industrial Electronics Society* (IEEE, 2020), pp. 1279–1284.
[196]P. Alou, O. Garcia, J. A. Cobos, J. Uceda, and M. Rascon, "Flyback with active clamp: Suitable topology for low power and very wide input voltage range applications," in *APEC Seventeenth Annual IEEE Applied Power Electronics Conference and Exposition (Cat. No. 02CH37335)* (IEEE, 2002), pp. 242–248.
[197]A. A. Mohammed and S. M. Nafie, "Flyback converter design for low power application," in *2015 International Conference on Computing, Control, Networking, Electronics and Embedded Systems Engineering (ICCNEEE)* (IEEE, 2015), pp. 447–450.
[198]Q. Cao, Z. Li, and H. Wang, "Wide voltage gain range LLC DC/DC topologies: State-of-the-art," in *2018 International Power Electronics Conference (IPEC-Niigata 2018 -ECCE Asia)* (IEEE, 2018), pp. 100–107.
[199]J. Zeng, G. Zhang, S. S. Yu, B. Zhang, and Y. Zhang, "LLC resonant converter topologies and industrial applications—A review," Chin. J. Electr. Eng. **6**(3), 73–84 (2020).
[200]Y.-C. Liu, B.-S. Huang, C.-H. Lin, K. A. Kim, and H.-J. Chiu, "Design and Implementation of a high power density active-clamped flyback converter," in *2018 International Power Electronics Conference (IPEC-Niigata 2018—ECCE Asia)* (IEEE, 2018), pp. 2092–2096.
[201]A. Oyane, T. Senanayake, M. Masuda, J. Imaoka, and M. Yamamoto, "13.56 MHz half-bridge GaN-HEMT resonant inverter achieving high power, low distortion, and high efficiency by 'L-S network'," IEICE Trans. Electron. **E105. C**(9), 2021ECP5048 (2022).
[202]D. Lumbreras, M. Vilella, J. Zaragoza, N. Berbel, J. Jordà, and A. Collado, "Effect of the heat dissipation system on hard-switching GaN-based power converters for energy conversion," Energies (Basel) **14**(19), 6287 (2021).
[203]C. Fei, F. C. Lee, and Q. Li, "High-efficiency high-power-density LLC converter with an integrated planar matrix transformer for high-output current applications," IEEE Trans. Ind. Electron. **64**(11), 9072–9082 (2017).
[204]C. Fei, Y. Yang, Q. Li, and F. C. Lee, "Shielding technique for planar matrix transformers to suppress common-mode EMI noise and improve efficiency," IEEE Trans. Ind. Electron. **65**(2), 1263–1272 (2018).
[205]C. Fei, F. C. Lee, and Q. Li, "A new design paradigm for GaN based LLC converter," in *2017 IEEE Southern Power Electronics Conference (SPEC)* (IEEE, 2017), pp. 1–6.
[206]R. Ren, B. Liu, E. A. Jones, F. F. Wang, Z. Zhang, and D. Costinett, "Capacitor-clamped, three-level GaN-based DC–DC converter with dual voltage outputs for battery charger applications," IEEE J. Emerg. Sel. Top. Power Electron. **4**(3), 841–853 (2016).
[207]D. Song *et al.*, "Highly dynamic multiphase wide-bandgap DC-DC converter for automotive active suspension systems," in *2017 IEEE 3rd International Future Energy Electronics Conference and ECCE Asia (IFEEC 2017—ECCE Asia)* (IEEE, 2017), pp. 528–533..
[208]M. Domb, "High power density, high efficiency 380v to 52v LLC converter utilizing E-mode GaN switches," in *PCIM Europe 2016: International Exhibition and Conference for Power Electronics, Intelligent Motion, Renewable Energy and Energy Management* (VDE, Nuremberg, 2016), pp. 1–7.
[209]A. Amirahmadi, M. Domb, and E. Persson, "High power density high efficiency wide input voltage range LLC resonant converter utilizing E-mode GaN switches," in *2017 IEEE Applied Power Electronics Conference and Exposition (APEC)* (IEEE, 2017), pp. 350–354.
[210]"Emerging technologies for submarines of the future," (2023), https://www.spsnavalforces.com/story/?id=584&h=Emerging-Technologies-for-Submarines-of-the-Future, accessed 8 November 2023.
[211]K. Alatawi, F. Almasoudi, M. Manandhar, and M. Matin, "Comparative analysis of Si- and GaN-based single-phase transformer-less PV grid-tied inverter," Electron (Basel) **7**(3), 34 (2018).
[212]Y. Zhang, J. Li, J. Wang, T. Q. Zheng, and P. Jia, "Dynamic-state analysis of inverter based on cascode GaN HEMTs for PV application," Energies (Basel) **15**(20), 7791 (2022).
[213]C.-T. Ma and Z.-H. Gu, "Design and implementation of a GaN-based three-phase active power filter," Micromachines (Basel) **11**(2), 134 (2020).
[214]M. Ugur, H. Sarac, and O. Keysan, "Comparison of inverter topologies suited for integrated modular motor drive applications," in *2018 IEEE 18th International Power Electronics and Motion Control Conference (PEMC)* (IEEE, 2018), pp. 524–530.
[215]M. Mahmoudian, M. Gitizadeh, A. H. Rajaei, and V. M. Tehrani, "Common mode voltage suppression in three-phase voltage source inverters with dynamic load," IET Power Electron. **12**(12), 3141–3148 (2019).
[216]Y. Fu *et al.*, "Design methodology of a three-phase four-wire EV charger operated at the autonomous mode," IEEE Trans. Transp. Electrif. **5**(4), 1169–1181 (2019).
[217]K. A. Kim, "Opening the box: Survey of high power density inverter techniques from the little box challenge," CPSS Trans. Power Electron. Appl. **2**(2), 131–139 (2017).
[218]A. S. Morsy and P. N. Enjeti, "Comparison of active power decoupling methods for high-power-density single-phase inverters using wide-bandgap FETs for Google Little Box Challenge," IEEE J. Emerg. Sel. Top. Power Electron. **4**(3), 790–798 (2016).
[219]D. Bortis, D. Neumayr, and J. W. Kolar, "$\eta\rho$-Pareto optimization and comparative evaluation of inverter concepts considered for the GOOGLE Little Box Challenge," in *2016 IEEE 17th Workshop on Control and Modeling for Power Electronics (COMPEL)* (IEEE, 2016), pp. 1–5.
[220]Y. Lei *et al.*, "A 2-kW single-phase seven-level flying capacitor multilevel inverter with an active energy buffer," IEEE Trans. Power Electron. **32**(11), 8570–8581 (2017).
[221]G. Xu *et al.*, "The mitigating effects of the threshold voltage shifting on the false turn-on of GaN E-HEMTs," in *2018 IEEE Applied Power Electronics Conference and Exposition (APEC)* (IEEE, 2018), pp. 909–912.
[222]R. Xie, H. Wang, G. Tang, X. Yang, and K. J. Chen, "An analytical model for false turn-on evaluation of high-voltage enhancement-mode GaN transistor in bridge-leg configuration," IEEE Trans. Power Electron. **32**(8), 6416–6433 (2017).
[223]M. Hua, J. Wei, Q. Bao, Z. Zhang, Z. Zheng, and K. J. Chen, "Dependence of VTH stability on gate-bias under reverse-bias stress in E-mode GaN MIS-FET," IEEE Electron Device Lett. **39**(3), 413–416 (2018).
[224]Y. Jia *et al.*, "Characterization and optimal control of totem-pole PFC converter with high frequency GaN HEMTs and low frequency Si diodes," IEEE Trans. Ind. Electron. **68**(11), 10740–10749 (2021).
[225]F. Gao, Q. Zhou, P. Wang, and C. Zhang, "A gate driver of SiC MOSFET for suppressing the negative voltage spikes in a bridge circuit," IEEE Trans. Power Electron. **33**(3), 2339–2353 (2018).
[226]Y. Chen, R. Wang, X. Liu, and Y. Kang, "Gate-drive power supply with decayed negative voltage to solve crosstalk problem of GaN synchronous buck converter," IEEE Trans. Power Electron. **36**(1), 6–11 (2021).
[227]N. Kashyap and J. Bauman, "Optimizing PWM control for efficiency and reduction of false turn-on events in synchronous Buck GaN converters," IEEE Access **9**, 146000–146009 (2021).
[228]H. Qin, W. Wang, S. Xie, X. Han, Z. Xu, and L. Wang, "Characterization and optimization of active negative voltage driving circuit for CoolGaN HEMTs in a phase-leg configuration," Energy Rep. **8**, 780–788 (2022).

21 October 2024 08:24:33

© Author(s) 2024

[229]A. Wang, L. Zeng, and W. Wang, "Simulation of gate leakage current of AlGaN/GaN HEMTs: Effects of the gate edges and self-heating," ECS J. Solid State Sci. Technol. **6**(11), S3025–S3029 (2017).
[230]S. Zhang *et al.*, "Suppression of gate leakage current in Ka-band AlGaN/GaN HEMT with 5-nm SiN gate dielectric grown by plasma-enhanced ALD," IEEE Trans. Electron Devices **68**(1), 49–52 (2021).
[231]A. D. S. Rawal *et al.*, "Design and fabrication of multi-finger field plate for enhancement of AlGaN/GaN HEMT breakdown voltage," Def. Sci. J. **68**(3), 290–294 (2018).
[232]Z. Sun *et al.*, "Effects of SiON/III-nitride interface properties on device performances of GaN-based power field-effect transistors," J. Phys. D: Appl. Phys. **54**(2), 025109 (2020).
[233]Y.-C. Yeo, T.-J. King, and C. Hu, "Metal-dielectric band alignment and its implications for metal gate complementary metal-oxide-semiconductor technology," J. Appl. Phys. **92**(12), 7266–7271 (2002).
[234]A. Babaya, A. Saadi, and S. Bri, "New investigation of an E-mode metal-insulator-semiconductor AlInN/AlN/GaN HEMT with an Au-T-gate," Telecommun. Comput. Electron. Control **19**(2), 531 (2021).
[235]M. Meneghini, E. Zanoni, and G. Meneghesso, "Gallium nitride based HEMTs for power applications: High field trapping issues," in *2014 12th IEEE International Conference on Solid-State and Integrated Circuit Technology (ICSICT)* (IEEE, 2014), pp. 1–4.
[236]R. Vetury, N. Q. Zhang, S. Keller, and U. K. Mishra, *The Impact of Surface States on the DC and RF Characteristics of AlGaN/GaN HFETs* (IEEE, 2001).
[237]K. Li, P. Evans, and M. Johnson, "GaN-HEMT dynamic ON-state resistance characterisation and modelling," in *2016 IEEE 17th Workshop on Control and Modeling for Power Electronics (COMPEL)* (IEEE, 2016), pp. 1–7.
[238]I. Rossetto *et al.*, "Evidence of hot-electron effects during hard switching of AlGaN/GaN HEMTs," IEEE Trans. Electron Devices **64**(9), 3734–3739 (2017).
[239]I. Hwang *et al.*, "Impact of channel hot electrons on current collapse in AlGaN/GaN HEMTs," IEEE Electron Device Lett. **34**(12), 1494–1496 (2013).
[240]E. A. Jones, F. F. Wang, and D. Costinett, "Review of commercial GaN power devices and GaN-based converter design challenges," IEEE J. Emerg. Sel. Top. Power Electron. **4**(3), 707–719 (2016).
[241]O. Hilt, E. Bahat-Treidel, E. Cho, S. Singwald, and J. Wurfl, "Impact of buffer composition on the dynamic on-state resistance of high-voltage AlGaN/GaN HFETs," in *2012 24th International Symposium on Power Semiconductor Devices and Ics* (IEEE, 2012), pp. 345–348.
[242]E. A. Jones and A. Pozo, "Hard-switching dynamic $R_{ds,on}$ characterization of a GaN FET with an active GaN-based clamping circuit," in *2019 IEEE Applied Power Electronics Conference and Exposition (APEC)* (IEEE, 2019), pp. 2757–2763.
[243]Y. Cai, A. J. Forsyth, and R. Todd, "Impact of GaN HEMT dynamic on-state resistance on converter performance," in *2017 IEEE Applied Power Electronics Conference and Exposition (APEC)* (IEEE, 2017), pp. 1689–1694.
[244]N. Badawi, O. Hilt, E. Bahat-Treidel, J. Bocker, J. Wurfl, and S. Dieckerhoff, "Investigation of the dynamic on-state resistance of 600 v normally-off and normally-on GaN HEMTs," IEEE Trans. Ind. Appl. **52**(6), 4955–4964 (2016).
[245]W. Zhang, Z. Xu, Z. Zhang, F. Wang, L. M. Tolbert, and B. J. Blalock, "Evaluation of 600 V cascode GaN HEMT in device characterization and all-GaN-based LLC resonant converter," in *2013 IEEE Energy Conversion Congress and Exposition* (IEEE, 2013), pp. 3571–3578.
[246]T. Yao and R. Ayyanar, "A multifunctional double pulse tester for cascode GaN devices," IEEE Trans. Ind. Electron. **64**(11), 9023–9031 (2017).
[247]R. Burgos, Z. Chen, D. Boroyevich, and F. Wang, "Design considerations of a fast 0-Ω gate-drive circuit for 1.2 kV SiC JFET devices in phase-leg configuration," in *2009 IEEE Energy Conversion Congress and Exposition* (IEEE, 2009), pp. 2293–2300.
[248]H. Wang, J. Wei, R. Xie, C. Liu, G. Tang, and K. J. Chen, "Maximizing the performance of 650-V p-GaN gate HEMTs: Dynamic RON characterization and circuit design considerations," IEEE Trans. Power Electron. **32**(7), 5539–5549 (2017).
[249]B. Lu, T. Palacios, D. Risbud, S. Bahl, and D. I. Anderson, "Extraction of dynamic on-resistance in GaN transistors: Under soft- and hard-switching conditions," in *2011 IEEE Compound Semiconductor Integrated Circuit Symposium (CSICS)* (IEEE, 2011), pp. 1–4.
[250]R. Li, X. Wu, S. Yang, and K. Sheng, "Dynamic on-state resistance test and evaluation of GaN power devices under hard- and soft-switching conditions by double and multiple pulses," IEEE Trans. Power Electron. **34**(2), 1044–1053 (2019).
[251]W. Wang, Y. Liang, M. Zhang, F. Lin, F. Wen, and H. Wang, "Mechanism analysis of dynamic on-state resistance degradation for a commercial GaN HEMT using double pulse test," Electron (Switzerland) **10**(10), 1202 (2021).
[252]A. F. Al-Neama, N. Kapur, J. Summers, and H. M. Thompson, "Thermal management of GaN HEMT devices using serpentine minichannel heat sinks," Appl. Therm. Eng. **140**, 622–636 (2018).
[253]A. Wang, L. Zeng, and W. Wang, "Three-dimensional steady and transient fully coupled electro-thermal simulation of AlGaN/GaN high electron mobility transistors: Effects of lateral heat dissipation and thermal crosstalk between gate fingers," AIP Adv. **7**(9), 095304 (2017).
[254]F. Xia *et al.*, "Investigation of high threshold voltage E-mode AlGaN/GaN MIS-HEMT with triple barrier layer," Results Phys. **25**, 104189 (2021).
[255]L. M. Weituschat, W. Dickmann, J. Guimbao, D. Ramos, S. Kroker, and P. A. Postigo, "Photonic and thermal modelling of microrings in silicon, diamond and GaN for temperature sensing," Nanomaterials **10**(5), 934 (2020).
[256]J. Li, J. Wang, J. d Cai, Y. f Xu, B. f Fan, and G. Wang, "Numerical simulation and analysis of process parameters of GaN-MOCVD reactor," Int. Commun. Heat Mass Transfer **91**, 64–76 (2018).
[257]M. Hosseinzadeh Sani and S. Khosroabadi, "Improving thermal effects and reduction of self-heating phenomenon in AlGaN/GaN/Si based HEMT," J. Electron. Mater. **50**(4), 2295–2304 (2021).
[258]A. Amar, B. Radi, and A. El Hami, "Electrothermal reliability of the high electron mobility transistor (HEMT)," Appl. Sci. (Switzerland) **11**(22), 10720 (2021).
[259]M. A. Alim, M. M. Ali, A. A. Rezazadeh, and C. Gaquiere, "Thermal response for intermodulation distortion components of GaN HEMT for low and high frequency applications," Microelectron. Eng. **209**, 53–59 (2019).
[260]A. K. Vallabhaneni, L. Chen, M. P. Gupta, and S. Kumar, "Solving nongray Boltzmann transport equation in gallium nitride," J. Heat Transfer **139**(10), 102701 (2017).
[261]V. Sodan *et al.*, "Fast and distributed thermal model for thermal modeling of GaN power devices," IEEE Trans. Compon. Packaging Manuf. Technol. **8**(10), 1747–1755 (2018).
[262]A. S. Yalamarthy *et al.*, "Tuning electrical and thermal transport in AlGaN/GaN heterostructures via buffer layer engineering," Adv. Funct. Mater. **28**(22), 1705823 (2018).
[263]Q. Hao, H. Zhao, Y. Xiao, and M. B. Kronenfeld, "Electrothermal studies of GaN-based high electron mobility transistors with improved thermal designs," Int. J. Heat Mass Transfer **116**, 496–506 (2018).
[264]Z. Liao *et al.*, "Thermal evaluation of GaN-based HEMTs with various layer sizes and structural parameters using finite-element thermal simulation," Microelectron. Rel. **74**, 52–57 (2017).
[265]S. Russo, V. D'Alessandro, M. Costagliola, G. Sasso, and N. Rinaldi, "Analysis of the thermal behavior of AlGaN/GaN HEMTs," Mater. Sci. Eng.: B **177**(15), 1343–1351 (2012).
[266]K. W. Jang, I. T. Hwang, H. J. Kim, S. H. Lee, J. W. Lim, and H. S. Kim, "Thermal analysis and operational characteristics of an AlGaN/GaN high electron mobility transistor with copper-filled structures: A simulation study," Micromachines (Basel) **11**(1), 53 (2020).
[267]Y. Dong, Z. Xie, D. Chen, H. Lu, R. Zhang, and Y. Zheng, "Effects of dissipative substrate on the performances of enhancement mode AlInN/GaN HEMTs," Int. J. Numer. Modell.: Electron. Netw. Devices Fields **32**(1), e2482 (2019).
[268]M. Borga *et al.*, "Impact of substrate resistivity on the vertical leakage, breakdown, and trapping in GaN-on-Si E-mode HEMTs," IEEE Trans. Electron Devices **65**(7), 2765–2770 (2018).

21 October 2024 08:24:33

© Author(s) 2024